Oil in ice: Transport, Fate and Potential Exposure

A Final Report Submitted to

The Coastal Response Research Center

Submitted by

Dr. Liv-Guri Faksness, Dr. Odd Gunnar Brakstad, Dr. Mark Reed, Frode Leirvik, and Dr. Per Johan Brandvik
SINTEF Materials and Chemistry
Marine Environmental Technology
NO-7465 Trondheim, Norway

Dr. Chris Petrich
University of Alaska Fairbanks

Project Period, 2008-2010

February 1, 2011
Revised May 2, 2011

This project was funded by a grant from NOAA/UNH Coastal Response Research Center. NOAA Grant Number(s): NA07NOS4630143. Project Number: 09-039, and SINTEF Materials and Chemistry.

SINTEF

SINTEF Materialer og kjemi
SINTEF Materials and Chemistry

Address:
Postboks 4760 Sluppen
NO-7465 Trondheim
NORWAY

Telephone:+47 73593000
Telefax:+47 73595910

info.mk@sintef.no
www.sintef.no/mk
Enterprise /VAT No.

KEYWORDS:
Arctic,
oil spills
water soluble oil components,
first-year sea ice,
biodegradation

Report

Oil in ice: Transport, Fate and Potential Exposure

Final report

VERSION
Final

DATE
2011-04-30

AUTHOR(S)
Liv-Guri Faksness, Odd Gunnar Brakstad, Mark Reed, Frode Lervik, Per Johan Brandvik, and Chris Petrich

CLIENT(S)
The Coastal Response Research Center

CLIENT'S REF.
Nancy Kinner

PROJECT NO.
800801

NUMBER OF PAGES/APPENDICES:
126/3 Appendices

ABSTRACT

A laboratory study has been performed to determine how ice growth conditions affect the transport and fate of entrapped oil in ice. Quantitative data on the partitioning of water soluble oil components into brine inclusions and channels has been collected. Since biodegradation of petroleum hydrocarbons at subzero temperatures in marine ice has not yet been shown, it has been essential to determine *if* crude oil biodegradation takes place in marine sea ice within a defined span of time and to what extent. Biodegradation as one of the hydrocarbon depletion processes in marine ice have been assessed. In addition, a 1-D model appropriate for implementation as a sub-model or module in regional ice models has been developed, such that numerical forecasting experiments can be carried out to determine the extent to which oil frozen into the ice may eventually represent a risk to biota during the melting phase.

PREPARED BY
Liv-Guri Faksness

SIGNATURE
Liv-Guri Faksness

CHECKED BY
Alf G. Melbye

SIGNATURE

APPROVED BY
Tore Aunaas

SIGNATURE

REPORT NO.
SINTEF A19275

ISBN
978-82-14-05136-0

CLASSIFICATION
Unrestricted

CLASSIFICATION THIS PAGE
Unrestricted

Abstract

Oil spilled in the arctic marine environment can be rapidly frozen into the ice sheet. The oil will in this way be preserved, in the sense that evaporation, dissolution, and degradation are expected to be reduced. This implies that the oil will retain much of its potential toxicity upon release from the ice, either via transport in brine channels and/or eventual breakup and melting of the ice sheet. Being able to estimate the pathways, release rates, and chemical characteristics of the remaining oil will provide the basis for eventual environmental risk and impact assessments. The purpose of this project has been to provide a basis and methodology for estimating routes and magnitudes of potential environmental exposures and concentrations of oil components migrating through the ice regime as the oil is subjected to a freezing-thawing cycle. This information can be used to support decision-making for oil spill response actions in ice-covered waters.

A laboratory study has been performed to determine how ice growth conditions affect the transport and fate of entrapped oil in ice. Quantitative data on the partitioning of water soluble oil components (WSC) into brine inclusions and channels has been collected. The experiments have shown that there is a downwards migration of WSC from oil encapsulated in the ice, and that the migration starts after spring thawing has increased the porosity of the ice. As long as the temperature in the ice is relatively low, the migration seems to be negligible. These observations are in accordance with the findings in field experiments in first-year sea ice on Svalbard (Faksness and Brandvik, 2008a,b). The content of bio-available WSC and their estimated acute toxicity expressed as hazard index (HI) in the brine channels have been calculated. The HI values for the ice core samples (5 cm sections) are below one for all reported samples (ranging from 0.001 to 0.96), which indicates that the concentrations in the ice samples were not high enough to represent an acute toxicity to local marine biota. Nevertheless, the ice organisms may be exposed to WSC over several months, which might cause potentially toxic oil components to enter the Arctic marine food web. The ice growth conditions in the laboratory experiments seem to be similar to natural conditions, but the spring thawing might be more difficult to simulate, as the experiments are performed in a closed system where natural processes such as tide movements, currents and sunlight (albedo effect) were not included. Faksness and Brandvik (2008b) observed an upward migration of oil during their field experiments on Svalbard, but no upward transport was observed during the spring thawing in these laboratory experiments, indicating that the tide movement, sunlight, and albedo effect are important factors that should be taken into account in future experiments.

In order to investigate the potentials for oil biodegradation in marine ice, depletion of oil in artificial seawater-based brines was examined in biotic and sterile systems at subzero temperatures. The selected biodegradation conditions were relevant for salinities in brine channels of marine ice at -5 and -10°C, and the experiments were conducted at these temperatures. A paraffinic oil was used during the experiments, and the oil fractions included water-soluble fractions (WSFs) generated by careful stirring of the oil in seawater, and *n*-alkanes immobilized to hydrophobic Fluortex adsorbents. Two separate

biodegradation studies were performed over periods of 6 months. One experiment examined the effects of different temperatures (+5 to -10°C), the other focused on the effects of added inorganic nutrients. The experiments indicated that slow biodegradation appeared in brines at subzero temperatures in the water-soluble fraction, but not in the oil phase. However, due to possible biodegradation in the sterile controls, it was not possible to determine the contribution of biodegradation to the depletion of soluble hydrocarbon in the experiments. The potential biodegradation in the brines at sub-zero temperatures was supported by microbiological analyses like epifluorescence microscopy counts and bacterial PCR-DGGE. The results indicated that no stimulation of biodegradation resulted from the use of inorganic nutrients. If bioremediation is to be used in ice it is therefore important to investigate novel systems specially designed for improving biodegradation in sea ice brine.

Further investigations of oil-in-ice biodegradation should be conducted to determine the fate of hydrocarbons in the ice and to include these data as part of the risk assessment of oil in ice. It may also be of interest to investigate the possibilities of treating oil spills in the Arctic with respect to stimulation of oil biodegradation during the arctic winter

This work joins a thermal model of snow and sea ice growth and melt with internal fluxes, including natural convection during ice growth, forced convection during desalination, and exchange between fluid in a porous medium and brine channels. At the same time, high numerical efficiency has been sought, such that the approach can be implemented as a module in regional ice models. The ice growth model was implemented based on a fixed number of grid cells that are adjusted in size during growth and melt. A description of surface ablation of ice was included; although this could not be thoroughly validated in this project and should be revisited in future work. An approach was developed to derive snow depth from precipitation measurements, and to quantify snow ablation based on air temperature reports. Compared with field measurements, simulated snow depth appears to be realistic. In conjunction with the ice growth model, derived ice temperature profiles reproduce field measurements well. Based on the simulated development of a bulk salinity profile, the flow field inside sea ice appears to behave as expected. However, the parameter space is large, in spite of simplifying assumptions such as those of constant brine density and infinite vertical permeability of brine channels.

The 1-D model developed here is appropriate for implementation as a sub-model or module in regional ice models, such that numerical forecasting experiments can be carried out to determine the extent to which oil frozen into the ice may eventually represent a risk to biota during the melting phase. The model therefore represents a contribution to decision support tools for oil spill response in the Arctic.

Keywords: Arctic, oil spills, water soluble oil components, first-year sea ice, biodegradation

Acknowledgements

This project was funded by a grant from NOAA/UNH Coastal Response Research Center and SINTEF Materials and Chemistry.
NOAA Grant Number(s): NA07NOS4630143. Project Number: 09-039.
SINTEF project number: 800801.

We gratefully acknowledge Hajo Eicken, UAF, for valued input and discussions, and Kjersti Almås, Kristin Bonaunet, Ragnhild L. Daae, Bror Johansen, Inger B. Steinsvik, Marianne U. Rønsberg, and Siv-Hege Vang at SINTEF for their valued assistance in the laboratory.

Table of Contents

List of Figures and Tables

1 Introduction

The project has been split into three main activities:

1. Transport and physical fate of oil hydrocarbons in ice;
2. Biodegradation of crude oil hydrocarbons in ice, with focus on the brine channels/inclusions; and
3. Modeling of behavior and biodegradation of crude oil hydrocarbons in ice (prototype model)

Each activity is described in separate chapters, which includes introduction, objectives, methods, results, and summary and conclusions.

2 Transport and physical fate of oil hydrocarbons in ice

2.1 Introduction

The behavior of oils in freezing environments includes spreading in ice, snow, under ice, and in water with ice present. Important parameters for oil spreading in ice are specific gravity and viscosity (Chen *et al.*, 1974), but also oil-ice interfacial tension is important (Kawamura *et al.*, 1986). Hydrocarbons released from the ice-encapsulated oil may be transported downward through the brine channels (Faksness and Brandvik, 2005, 2008a, 2008b), thereby coming in contract with organisms in a fluid medium. The remaining oil escapes the ice in the spring as the ice deteriorates by two general processes: a) vertical rise of the oil through the brine channels in the ice (Martin, 1979), and b) ablation of the ice surface down to the oil lens in the ice (Fingas and Hollebone, 2003).

This research aims to complement and complete the knowledge needed to understand the transport and fate of oil components resulting from oil spills in ice and cold climates. Until recently, most of the research conducted on migration of oil through ice has focused on bulk oil (NORCOR, 1975; Martin, 1979; Reed *et al*., 1999; Fingas and Hollebone, 2003; Payne *et al*., 1991; and Brandvik *et al.*, 2004), and most of the conceptual models for oil-in-ice discuss upward migration of oil through brine channels during melting, due to density differences, solar radiation and heat capacity of the oil. Very few studies have actually attempted to determine the transport and fate of individual compounds, such as PAHs or changes in oil composition in ice scenarios. Recent work has shown that the more soluble components are transported downwards through brine channels (Faksness and Brandvik, 2005, 2008a, 2008b).

Species sensitivity to oil may be less or more than for temperate species, but one would expect to be able to predict mortality within a range of PAH concentrations regardless of species type using hazard index (e.g. Neff et al., 2006) or toxic units (e.g. DiToro et al., 2007) . What cannot successfully be predicted with the current state of knowledge on ice-oil interactions, are the routes of exposures, the concentrations or durations of oil components (dissolved and particulate) migrating through the ice regime as the oil is subjected to a freezing-thawing cycle. Evidence suggests that the presence and dynamics of brine channels transports the bioavailable oil components downward from an "encapsulated slick" in a non-trivial manner through diffusion and advection (Faksness and Brandvik, 2005, 2008a, 2008b), as depicted in Figure 2.1.

Three field seasons with oil encapsulated in first-year Arctic sea ice have shown that not only the ice thickness and the temperature profile in the ice, but also the air temperature prior to an oil spill are significant for the distribution of water soluble oil components (Faksness and Brandvik, 2008b). A relatively high air temperature (e.g. mean temperature -9.7 ºC (±8) in 2005, 7 ºC higher than normally) resulted in a more porous ice and the major part of the water soluble oil components (WSC) will leak out quickly, meaning the remaining amounts of toxic WSC in the ice will be low. However, if a spill occurs during extremely cold conditions (e.g. mean air temperature -22.8 ºC (±4) in 2004, -4 ºC lower than normally), the ice becomes less porous and WSC leak out more slowly. This results in a longer exposure period to low concentrations of toxic WSC for the ice organisms.

The results from the three field seasons strongly indicate that the transport of WSC occurs mainly in the brine channels. Thus, the amounts of bio-available WSC and their estimated acute toxicity in the brine channels have been calculated (Faksness and Brandvik, 2008b). The estimated results indicate that the concentration of WSC in the brine channels are acutely toxic to the ice organisms and will most likely cause toxic oil components to enter the Arctic marine food web. This study, coupled with an understanding of the micro-scale dynamics of sea-ice (reviewed by Eicken, 2003), led to the experiments outlined in this project.

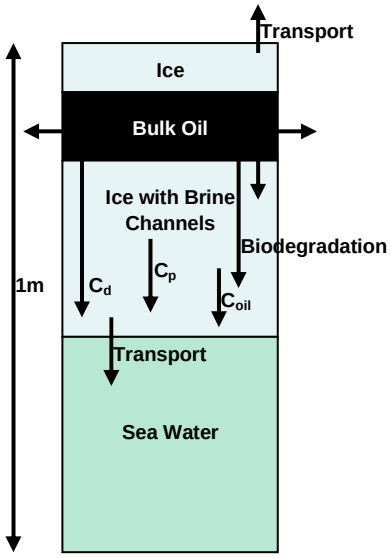

Figure 2.1 Schematic of transport processes of bulk oil components through a column of sea ice, where C_d represents the dissolved phase; C_p represents the particulate phase (sorbed to particulate or oil droplets); and C_{oil} represents oil droplets. Transport represents both advection and diffusion processes.

2.2 Objective

Transport/exposure laboratory studies to determine how ice growth conditions affect the transport and fate of entrapped oil in ice and to collect quantitative data on the partitioning of oil components (bioavailable fractions) into brine inclusions and channels and rates of vertical transport;

2.3 Methods

2.3.1 Experimental system

A key component of this study was to expand upon the work of Faksness and Brandvik (2005, 2008a, b) through laboratory experiments at SINTEF Sealab.

A setup with a series of 8 columns for ice core freezing was established. The columns were constructed to simulate the freezing of first year sea-ice to quantify changes in dissolved oil component concentrations over time through freezing and thawing cycles. The columns are filled with natural seawater.

The columns were made of 80 cm polycarbonate cylinders with an inner diameter of 144 mm. Each column was placed in a Styrofoam box (Figure 2.2) and the void between the box and the column is filled with insulating padding. The system is placed in a temperature controlled room at -22°C. The ice growth is monitored closely in one of the columns by thermistor strings positioned at every 5th cm in the ice for temperature readings during the experiments.

Figure 2.2 The setup of columns for ice core freezing.

As shown in Figure 2.3 the temperature in the box is controlled, both in the seawater and the air surrounding the column. The water surface is exposed to the room temperature of -22°C during freezing of ice, but during thawing a Styrofoam hat with a heating element is introduced on top of the system. The temperature just above the ice is controlled during thawing.

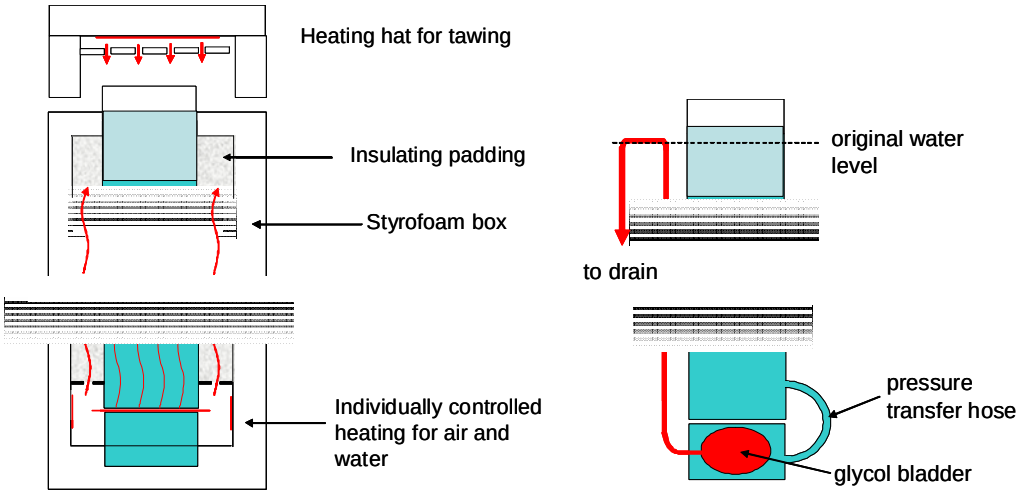

Figure 2.3 Column design and freezing and melting procedure

The heater at the base provides for a small heat flux into the column that prevents formation of frazil ice or freezing onto the side walls of the column. A pressure release mechanism prevents the brine from being pushed upward through the ice as the ice cover gradually thickens. Pressure is transferred to the underlying tank, a glycol bladder is compressed, and glycol is expelled on the outside of the system as illustrated in Figure 2.3 (right sketch).

When the ice thickness reached approx 40-50 cm, Statfjord crude oil (3 mm oil film thickness) was applied as shown in Figure 2.4 A hole (10 cm in diameter at 10 cm depth) was drilled into the ice. The oil and the hole was covered with slush ice and allowed to re-freeze before first sampling.

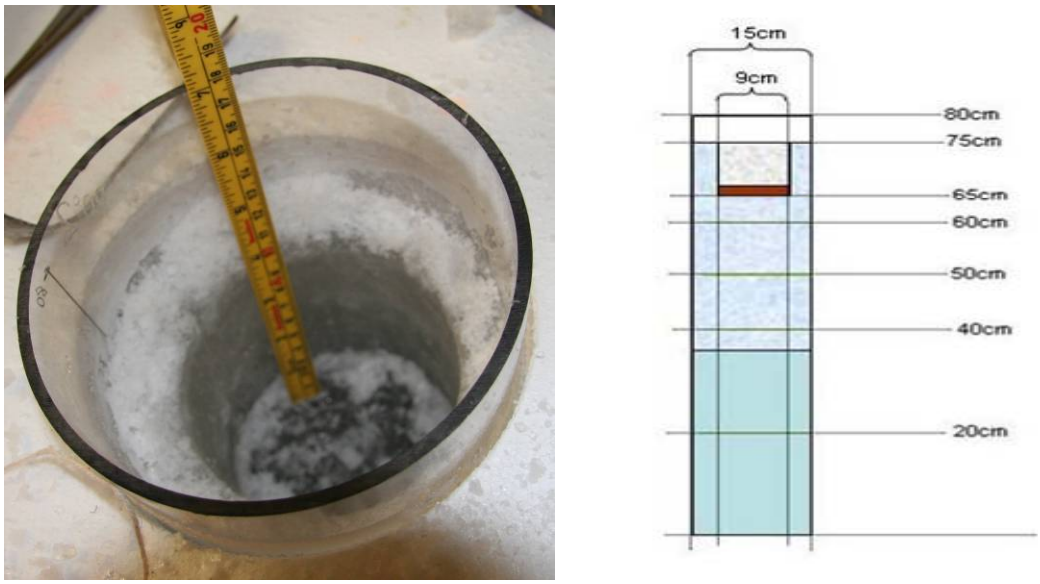

Figure 2.4 Application of oil into the ice columns (day 0), and an illustration of the column design

Sampling with passive samplers (solid phase micro extraction fibers (SPME)) in the ice columns was tested. SPMEs are optical fibers with a poly(dimethylsiloxane) coating thickness of 50 µm and a total diameter of 160 µm acquired from Dr. Lohman at University of Rhode Island URI). Four SPMEs positioned at four levels in the ice and one in the water under the ice for on site sampling was used (as illustrated in Figure 2.5). One SPME from all levels were sampled at each sampling time. The assumed advantage was that one does not has to "sacrifice" the column at sampling (cutting the ice core in sections and thawing the ice for extraction of WSC), but can follow the behavior of oil in the same column through the whole experimental period.

Both the established sampling technique with cutting the ice core into sections before melting followed by liquid-liquid extraction and in situ SPME passive sampling have been used. Preparation of SPMEs prior to use was performed by URI (Lohmann, 2010), and the SPMEs were shipped in deionized water to SINTEF.

Figure 2.5 Column with SPMEs, one level shown.

The experiments have been performed in three phases:

- Phase I: Testing and establishment of freezing and thawing cycles (times and different temperature profiles), and documentation of the ice properties.
- Phase II (Table 2.1): Different sampling techniques have been compared; in addition, one column was used as reference ice core (column 1) with temperature logging and for characterization of ice properties. The established sampling technique with cutting the ice core into sections before melting followed by liquid-liquid extraction and SPME passive sampling have been compared. Three replicate experiments (columns) with SPMEs were performed.

- Phase III (Table 2.2): Replicate experiments using different sampling techniques were planned, however, it was decided that no SPMEs should be used (phone conference with CRRC, UAF and SINTEF June 16, 2010), so only the sampling technique with cutting the ice core into sections before melting followed by liquid-liquid extraction were applied.

Table 2.1 Experimental setup and sampling for columns in phase II.

		Sampling (days after oil application)				
		6	11	25	65	Description sampling
Col 1	REF				X	Reference, no oil added. Temp logging and ice properties
Col 3		X				Whole column, cut in sections and melted
Col 6			X			Whole column, cut in sections and melted
Col 4				X		Whole column, cut in sections and melted
Col 2					X	Whole column, cut in sections and melted
Col 5	SPME	2 d	X	X	X	Colum with passive samplers
Col 7	SPME	X	X	X		Colum with passive samplers
Col 8	SPME	X	X	X	X	Colum with passive samplers

Table 2.2 Experimental setup for columns in phase III (no SPME).

		Sampling (days after oil application)			
		9	21	35	Comments
Col 2	REF			X	Temperature readings (no oil)
Col 7	REF			X	Reference column (no oil)
Col 6		X			
Col 8		X			
Col 3			X		
Col 4			X		
Col 1				X	
Col 5				X	

2.3.2 Sample preparation

The ice columns were split into 5 cm sections from 20 cm and below, and the ice sections were melted in closed containers. A 20 mL aliquot from each sample were used for salinity measurement. Salinity was measured using a Mettler Toledo SevenGo^{TM} Conductivitymeter SG3 or an Atago Salinity Refractometer S/Mill.

A Leitz 1400 Microtome was used for ice texture examination (thin section analysis). The sample processing and analysis are described in Eicken and Karlsson (2009).

Temperature and salinity measurements were used to calculate the ice properties. The brine volume fractions (V_b/V) as a function of ice temperature and salinity were calculated based on a set of equations described in Cox and Weeks (1983). Temperature and salinity of the ice are the prime controlling variables governing not only the phase fraction, but a whole host of other physical properties. The thermodynamic coupling between these different variables is a key aspect of sea ice as a geophysical material and a habitat, since any temperature change directly affects the porosity and pore microstructure of the ice as well as the salinity and chemical composition of the brine (Eicken, 2003). Direct measurements of these properties in the field are difficult. Commonly, the in situ brine volume fraction and other properties are hence derived from the bulk salinity of an ice sample and its in situ temperature, as in this project.

The volume of the melted ice was measured and the water was added hydrochloric acid to a pH below 2 to enhance the extraction efficiency of phenols. The water samples were spiked with surrogate internal standards (SIS; *o*-terphenyl, naphthalene-d_8, phenanthrene-d_{10}, chrysene-d_{12}, phenol-d_6, 4-methylphenol-d_8) and serially extracted with dichloromethane (Modified EPA Method 3510). The combined extracts were dried with sodium sulfate and concentrated to approximately 1 mL using a Zymark Turbovap® 500 Concentrator. The final extracts were spiked with the appropriate recovery internal standards (RIS; 5α-androstane, fluorene-d_{10}, and acenaphthene-d_{10}) and was analyzed by gas chromatography/flame ionization detection (GC/FID) and gas chromatography/mass spectrometry (GC/MS). The SIS and RIS were added to the samples to monitor procedural efficiencies on a sample-by-sample basis and to allow for accurate determination by internal standards. The results are reported as μg component/L melted ice (ppb).

The SPMEs were cut into small pieces and transferred to a GC-vial with hexane and internal standards (SIS) immediately after sampling. RIS was added to the samples prior to analysis on GC/FID and GC/MS. Quantifications were performed as described in Lohmann (2010) and are corrected with respect to porosity and salinity.

2.3.3 Analyses of ice core

- Characterization of ice properties: Temperature measurements in the ice through the experimental period, ice micro-structural characterization (on selected samples) and salinity measurements of melted ice sections.
- Liquid-liquid extraction of the melted ice cores: Screening analysis by GC/FID were performed according to a modification of EPA Method 8100, and single component analysis by GC/MS of decalines, phenols, naphthalenes and PAH compounds by a modified EPA Method 8270. A list of the target analytes is given in Table A 1 (Appendix A).
- Analysis of SPMEs: Same chemical analyses as the melted ice cores.

The experiments have provided detailed quantitative data of water soluble oil components that have been migrating through the ice.

2.3.4 Estimated toxicity in the brine volume of the ice

Exposure of oil may cause different harmful effects on marine organisms. It is expected that components with low molecular weight, e.g. BTEX and 2-3 rings PAH, which are fairly water-soluble and appear in relatively high concentrations, give a higher contribution to toxicity than less soluble components. A compound's specific acute toxicity (unspecific narcosis) is correlated to its partition coefficient for octanol-water, K_{ow}. The most hydrophobic components have the highest specific toxicity, but have also a low solubility in water, and the contribution to acute toxic effects may thus be limited or insignificant. French McCay (2002) has regarded components with log $K_{ow} > 5.6$ as insignificantly water-soluble, and not bio-available, however, other use log $K_{ow} > 6$ as a limit for bioavailability (McCarty, 1992, and Neff *et al.*, 2002).

The content of bio-available WSC in the brine volume of the ice has been determined for the ice cores. In order to predict toxicity, the hazard index (HI) approach (Neff et al. (2005 and 2006) for organic compounds whose primary acute effects is narcosis was applied: LC_{50} values for individual components are predicted from empirical correlations between log K_{ow}, and the HI is calculated from the measured concentrations of the WSC in the brine channels and the predicted LC_{50} values. The acute toxic effects of narcotic chemicals are assumed to be additive, excluding potential antagonistic or synergistic effects. The calculation of HI is described in Appendix C.
A value of HI >1 implies toxicity, i.e. the concentration in the ice is expected to cause 50% mortality in the organisms. An HI < 1 does not indicate that the oil is non-toxic to the environment, but only implies that the oil is not acutely toxic according to the predictions.

2.4 Results

The columns have been constructed to simulate the freezing of first-year sea ice to quantify the migration of dissolved oil components over time through freezing and thawing cycles. To simulate spring thawing, the temperature was increased to enhance the size of the brine channels and increase the transport and migration of oil components in the ice.

2.4.1 Phase I

In initial experiments, 20 cm of ice were frozen in approximately 56 hours. The ice formed in the initial experiments was microtomed and photographed. As shown in Figure 2.6, large crystals are growing vertically from the surface down. This is a crystal structure that favors the latter formation of brine channels.

Figure 2.6 Vertical slice if ice column (height 3-12 cm)

To simulate spring thawing, the temperature above the ice is controlled at a higher temperature to enhance the size of the brine channels. The time needed to warm up the entire column of frozen ice is strongly dependent on the temperature above the ice. The initial experiments indicate that several weeks may be needed to heat the entire ice core without overheating the upper layers. More details are given in Eicken and Karlsson (2009).

Eicken and Karlsson (2009) concluded that the stratigraphic and thin section analysis revealed that ice grown in the SINTEF ice-column experiments is representative of ice grown under natural conditions in coastal and offshore locations. Artifacts due to wall effects or uneven ice growth are minimal and the overall design should result in a homogenous ice sheet.

2.4.2 Phase II

Two different sampling techniques (SPMEs and ice columns cut into sections and melted) were compared in phase II.

The experiments were initiated September 22, 2009. Oil was applied to the columns at day 0 (ice thickness approx 40-50 cm). First sampling was performed at day 2 (col 5) or 6, and thereafter the melting process was started. Sampling with comments is given in Table 2.3. There was visible oil spreading in all columns with SPMEs (as illustrated in Figure 2.7), and in one of four columns without SPMEs. As mainly the water soluble oil components are of interest, visible oil is referred to as “oil contamination”.

Examples of columns with the oil nicely entrapped in the ice are shown in Figure 2.8. The column experiment lasted for 65 days (after oil application). There were a few problems with the temperature control during the experiment, so it is expected that the next experiment (phase III) will be shorter.

There were several problems with the experimental setup during the experiments in phase II. Especially a few episodes of uncontrolled increased temperature might have influenced the results and the ice properties, and for approximately a day the ice below 20-25 cm was melted. As the temperature recording was performed in the reference column, and all columns were individually controlled, there is a possibility that the monitored ice temperature is not representative for all columns during the experimental period.

The chosen column design with SPMEs resulted in oil migration along the walls in all columns and a bulk oil contamination in a large number of SPME samples. In addition, there were problems with removing the SPMEs from the column and/or SPME breakage during the first samplings (see overview in Table A 2). Pressure changes in the columns during sampling of the SPMEs were probably the cause of oil migration. The thin section analysis of the ice cores showed columnar (congelation) ice in all columns.

Table 2.3 Overview sampling with comments (Days after oil application).

Col		days	days	days	days	Comments at sampling time
1	ref				65	Reference, no oil added
3		6				Oil encapsulated in the ice (no visible contamination)
6			11			Oil encapsulated in the ice (no visible contamination)
4				23		Oil contamination
2					65	Oil encapsulated in the ice (no visible contamination)
5	spme	2	11	25	65	Oil contamination down to approx 30 cm
7	spme	6	11	25		Contamin, but exp finished after one month (temp probl)
8	spme	6	11	25	65	Oil contamination down to approx 15 cm

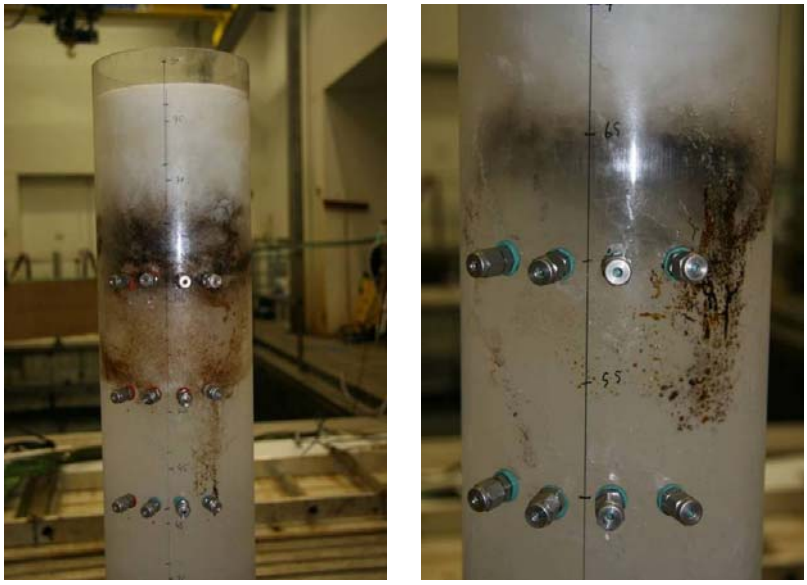

Figure 2.7 Column 5 (left) and column 8 (right) at sampling after 65 days, showing oil migration, probably due to pressure changes during SPME sampling.

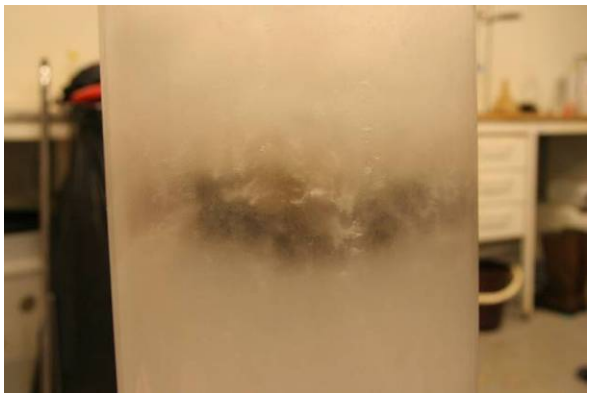

Figure 2.8 Column 6 sampled after 11 days. The oil is nicely encapsulated in the ice.

2.4.2.1 Ice properties, phase II

The temperature was recorded in the reference column (every 5th cm). Salinity was measured in the same samples as the chemistry samples. Ice characterization (thin section analysis) has been performed every 5th cm in the reference core (no oil), and in one section in column 2, 3 and 6. No salinity measurements or ice texture examination (thin section analysis) were performed in the SPME-columns.

The ice texture was examined in the ice columns (photos given in Appendix A). From the reference column both vertical and horizontal thin sections were made (Figure A 1), and from the remaining columns horizontal thin sections (25-26 cm depth) were made (Figure A 2). These figures have been evaluated by Hajo Eicken (Eicken, 2010): The thin section photos show columnar (congelation) ice in all samples. The vertical sections in column 1 (Figure A 1) indicates that there is some nucleation of new crystals of more random orientation at ca 20 cm depth. While this is explained in part by the melt event mentioned below, the crystal fabric below this depth is still more fine-grained with less preferential alignment than at the top. This is also evident in the horizontal sections from the other columns, in particular col 1, 3, 4 and 5 (Figure A 2), where crystals are less oriented than expected for columnar ice typically of the uppermost 20 cm in column 1 (Figure A 1).

The salinity profile in the ice shows a doubling to quadrupling of salinity with depth (Figure 2.10), as to be expected in closed columns that collects brine with increasing salt concentrations at the base (Eicken, 2010). At the same time, there is a significant decrease in salinity between day 6 and 65 in the lowermost 15-20 cm, which might be caused by brine drainage during sampling.

The temperature profiles have been recorded from the reference column (Figure 2.9), and show some consistent bias at 25 cm. This might be caused by the melt event, as there is no evidence on a miscalibration of the thermistor. Temperatures increase during the course of the experiment.

Figure 2.11 shows the permeability of the ice, which is calculated from the salinity measurements and temperature recordings (as described in Cox and Weeks (1983), and

Eicken (2003)). The calculations indicate that the permeability of the ice increased during the experiment. Permeability can also be denoted as brine volume or pore volume.

A few episodes of uncontrolled increased temperature might have influenced the results: The same day as the oil was applied in all columns (except column 6, where the oil was applied later) were the temperature in water increased dramatically, and it is assumed that the ice from approximately 20 cm and below melted and refroze again, probably in all columns. However, a horizontal hole in the ice was observed in the reference column, and the "messy" orientation of the crystals in the 18-27 cm vertical slice may arise from the accidental heating. This might have influenced the results. In addition, there was a power failure in the entire building October 13 for two hours. Room temperature increased to 1.5 ºC.

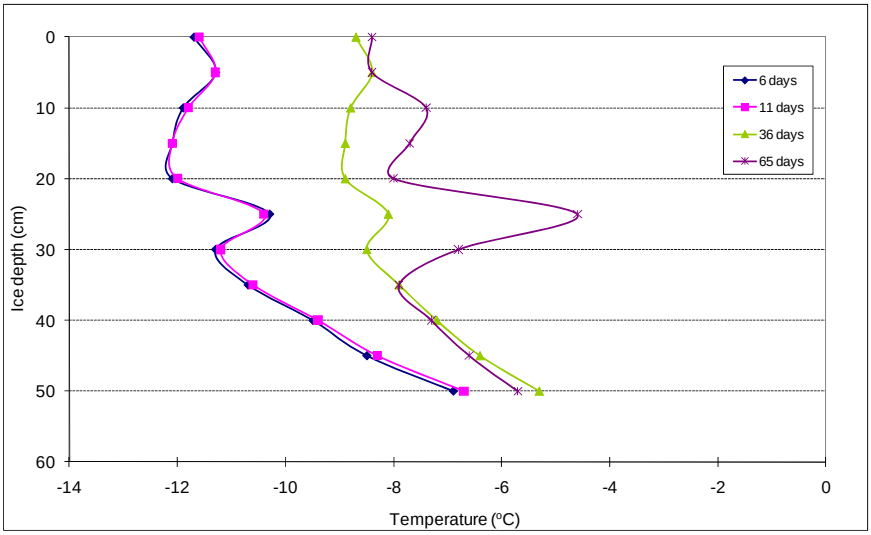

Figure 2.9 Temperature readings in the ice (from reference column).

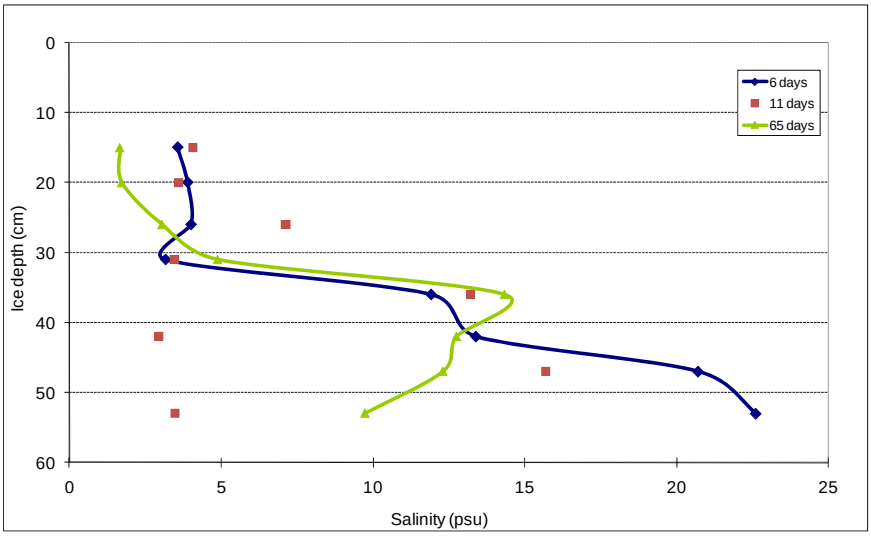

Figure 2.10 Salinity measurements from day 6, day 11, and day 6.

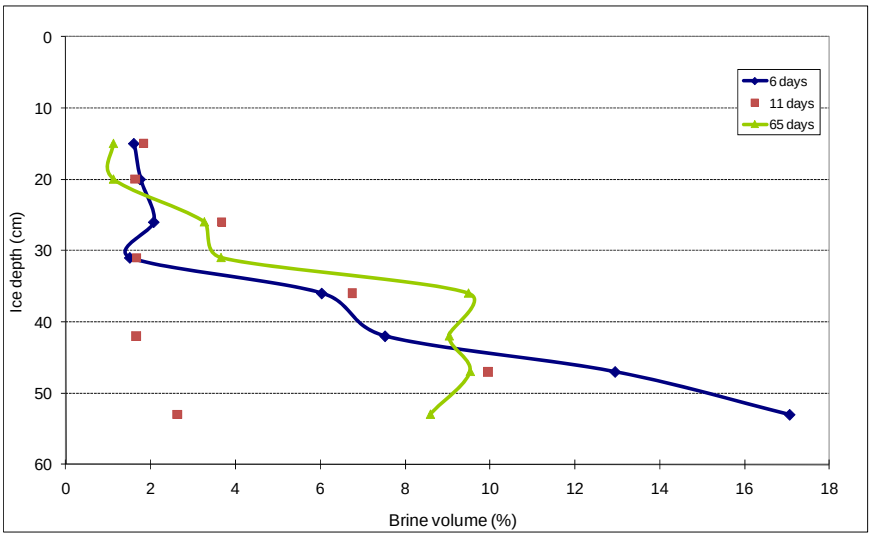

Figure 2.11 Brine volume calculated from temperature readings and salinity measurements

2.4.2.2 Chemical analyses, phase II

The results from the chemical analyses are given in Appendix A, Table A 3 to Table A 6 for SPME, and Table A 7 and Table A 8 for the melted ice cores. The results are correlated to mg SPME or total melted ice volume, and are corrected with respect to the calculated brine volume (porosity) in the ice.

2.4.2.2.1 Columns without SPMEs

The oil was entrapped in the upper part of the columns, so the section from 0 to 15 cm of the ice columns was not processed. The remaining ice core was split into sections of 5 cm. Column 4 (sampled at day 23) was not processed, due to that the oil had spread out too much. According to the GC/FID screening (results not shown) section 15-20 cm in column 2 (day 65) and 15-25 cm in column 3 (day 6) contained traces of oil droplets, while all other sections seem to contain only dissolved hydrocarbons. Data from these sections are not presented in the figures below.

The results presented in Figure 2.12 and Figure 2.13 have been corrected with respect to porosity. The figures illustrate that there is a concentration gradient, both in ice depth and as a function of time. The highest concentrations were observed in the section 26-31cm in the column sampled 6 days after oil application (181 µg/L brine fraction). However, the content of WSC are lower in the column sampled at day 11 (from 1.1 to 40 µg/L brine fraction) than the one sampled at day 65 (from 3.7 to 86 µg/L brine fraction). The naphthalenes, especially naphthalene and C1-naphthalenes, have a relatively high solubility in water, and will therefore give the highest contribution to the total SVOC content. This is in accordance with laboratory WAF experiments (Faksness et al., 2008) and data from field experiments on Svalbard (e.g. Faksness and Brandvik, 2008b).

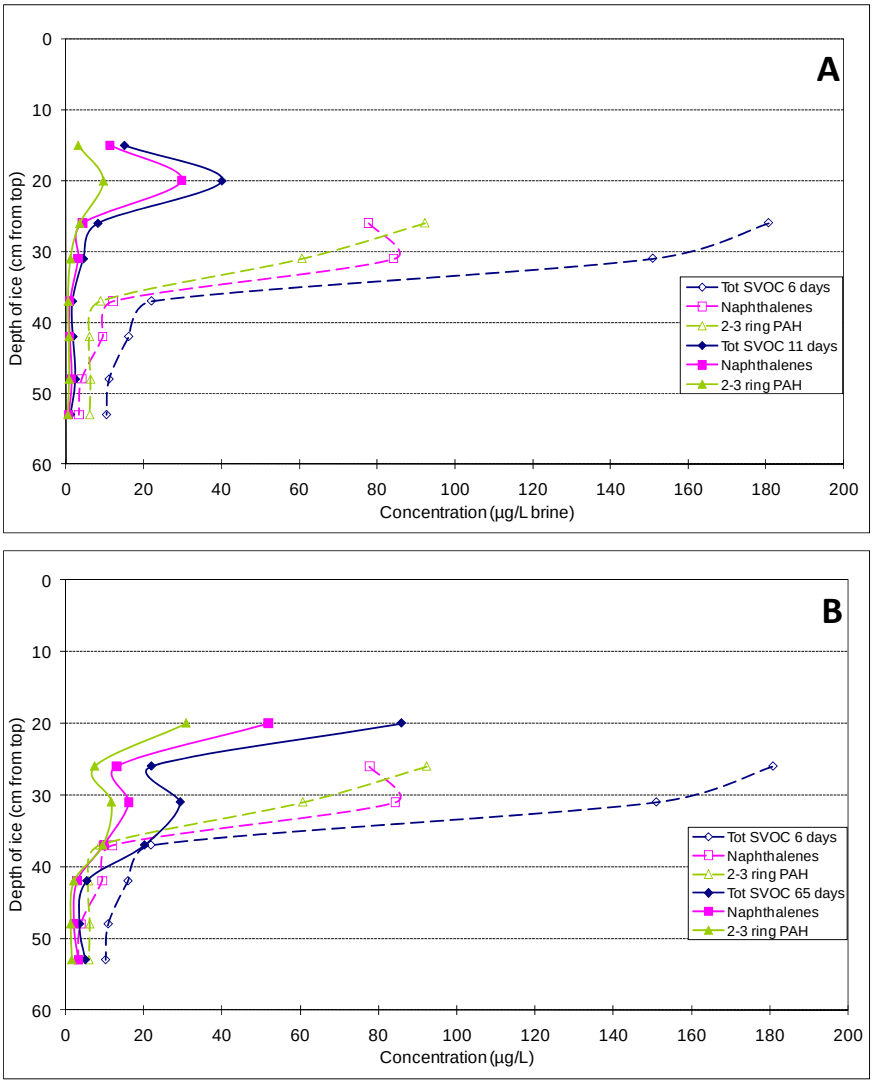

Figure 2.12 SVOC in ice cores vs depth given in µg analyte/L brine volume in ice (corrected for porosity). SVOC concentrations on day 6 compared to SVOC concentrations on day 11 (A) and day 6 compared to day 65 (B).

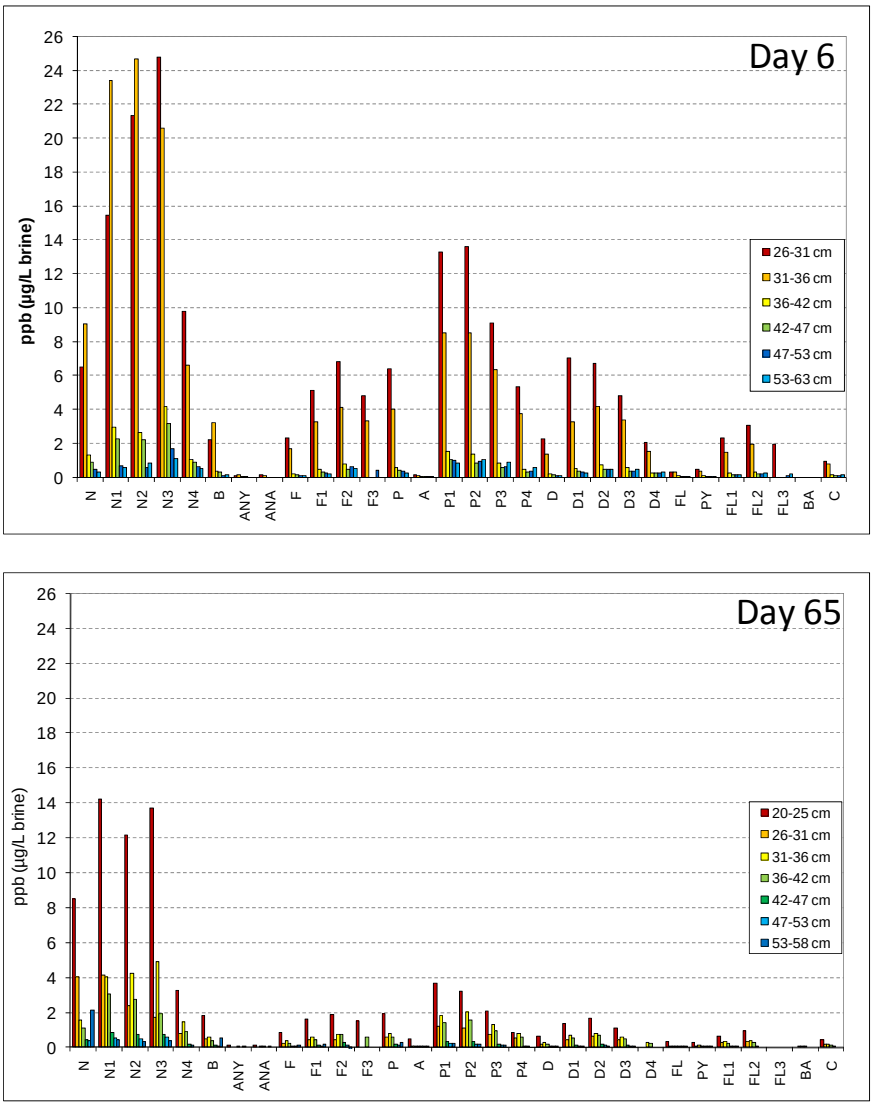

Figure 2.13 Distribution of SVOC in ice cores given in µg/L brine volume (corrected for porosity) as a function of depth for day 6 (upper figure) and day 65 (lower figure)

2.4.2.2.2 Columns with SPME

There was visible oil migration along the walls in all columns with SPMEs (as illustrated in Figure 2.7), which resulted in bulk oil contamination of a large number of SPME samples. As mainly the water soluble oil components are of interest, visible oil is referred to as "oil contamination". All samples are analyzed on GC/FID (screening) and GC/MS.

The results (Table A 3 to Table A 6) are presented as ng analyte/mg SPME and as µg analyte/L brine, which was calculated as described in Lohmann (2010) and expressed as concentration in pore water or brine water. However, no salinity measurements were performed in these ice cores, so the measurements from the ice cores with no SPME sampled the same day were used. There were mainly naphthalens detected in the SPMEs.

All samples were analyzed on GC/FID (screening) and GC/MS. Figure A 3 to Figure A 6 show the GC chromatograms from SPME sampling from column 7 after 25 days. The concentrations of SVOC in these columns were 0.53 ng/mg SPME at 55 cm, 0.43 ng/mg at 35 cm, 1.32 ng/mg at 25 cm and 594 ng/mg at 15 cm. Average concentrations in three reference SPMEs (i.e. SPMEs that not have been inserted in the ice or exposed to oil) was 0.50 ng/mg (±0.03). The results from the columns with SPME indicate that samples with no oil contamination (according to the GC chromatograms and visible observations) seem to be on background level when compared to analysis of reference SPME samples. In samples contaminated with oil (C10-C22), as illustrated in Figure A 3, the SVOC concentrations (naphthalenes, 2-3 ring PAHs and decalins) were from 90 to 2300 ng/mg SPME.

The results show that use of SPMEs not seems to be working as good as expected, but this might be due to the column design.

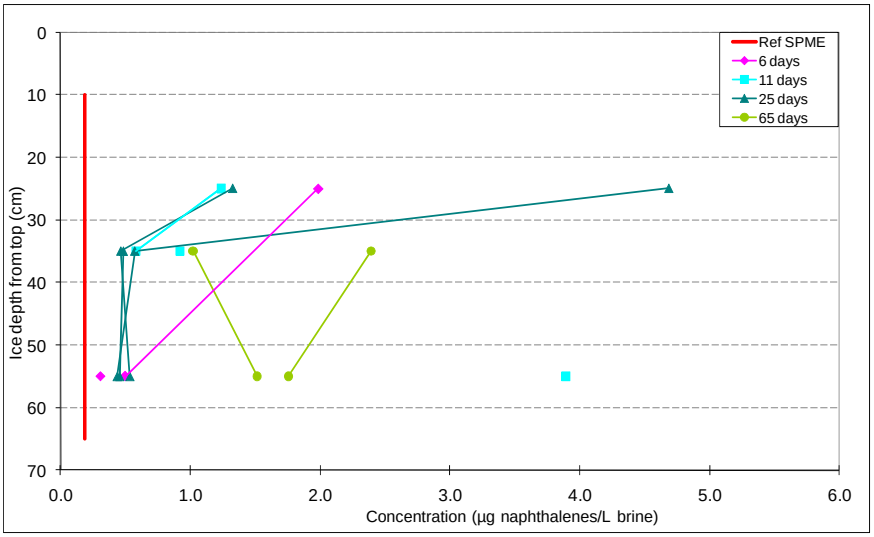

Figure 2.14 Naphthalenes quantified from SPMEs in ice cores, given as µg analyte/L brine volume. Red line indicates concentration in reference SPMEs (not exposed to ice and oil).

2.4.2.2.3 Comparing the sampling techniques

The chosen column design with SPMEs resulted in oil migration along the walls in all columns, probably due to a pressure change in the columns during sampling, which resulted in a bulk oil contamination in a large number of SPME samples. In addition, there were problems with removing the SPMEs from the column and/or SPME breakage during the first samplings (see overview in Table A 2).

The results have shown that naphthalenes, 2-3 ring PAHs and phenols were detected in the ice core samples, but mainly naphthalene and C1-naphthalenes in the SPMEs. The

concentration of naphthalenes in the SPMEs was more than 10-fold lower than in the ice cores (Figure 2.15), ranging from 0.3 to 4.2 µg/L in SPMEs and 3.9 to 84 µg/L in ice cores (corrected for porosity). The thin section analysis of the ice cores showed columnar (congelation) ice in all columns. However, it was not possible to remove an intact ice core from the SPME columns to perform ice texture examination.

As sampling of whole ice cores have given more applicable results then the SPME, it was decided that no SPMEs should be used in the experiments in phase III (phone conference with CRRC, UAF and SINTEF at June 16, 2010).

The estimated toxicity was not calculated for this experiment, as there were so many uncertain factors related to temperature and oil droplet migration due to column design.

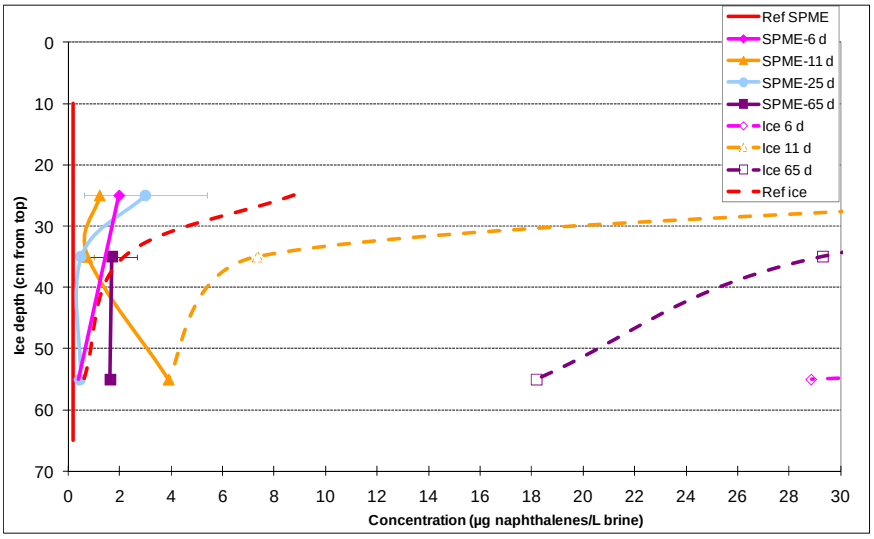

Figure 2.15 Comparing the concentration of naphthalenes sampled in SPMEs and melted ice cores, given in µg naphthalenes/L brine (related to porosity).

2.4.3 Phase III

As the results from the first ice column experiment have shown that the sampling with ice cores seems to give more applicable results than the SPMEs, it was decided to exclude SPMEs in phase III. In addition, the experiments were performed in a cold laboratory with adjustable temperature. Initial room temperature was set to -18 ºC, and increased carefully during the experimental period (see Figure 2.17)

The experiments in phase III were initiated August 10, 2010, and are described in Table 2.2. The melting process was started after first sampling (9 days after oil application). Second sampling was performed at day 21 and the last sampling at day 35 (September 27, 2010. Two columns were sampled each time.

The oil was nicely entrapped in the ice, and there was no visible oil migration in the ice as illustrated in Figure 2.16.

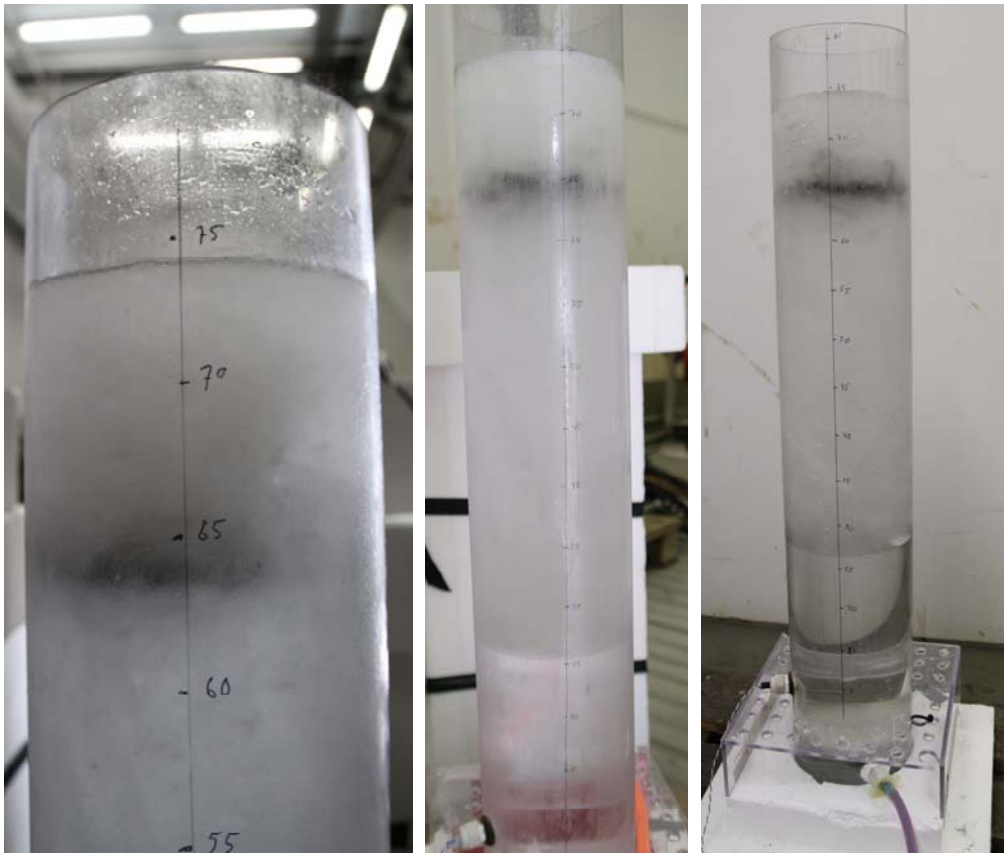

Figure 2.16 Sampling of ice cores. From left: Column 6 on day 9, column 3 on day 21, and column 5 on day 35.

2.4.3.1 Ice properties, phase III

The temperatures were logged every 5th cm in one of the columns. Salinity was measured in the same samples as the chemistry samples. No ice texture (thin section) was examined. The thin section analyses were usually performed at the cold laboratory at the Norwegian University of Science, but their cold laboratory has been out of order for a long time.

The temperature profiles in the ice from oil application to last sampling are shown in Figure 2.17. The "heater hat" was installed two days after oil application, and the temperatures were gradually increased both in the hat and in the room.

Figure 2.17 shows that there is a decrease in ice temperature during the experimental period, and that heating from the top gives an enhanced reduction in ice temperature in the upper part of the column. These data illustrates that there has been no problems with the temperature regulation in the cold room during this experiment.

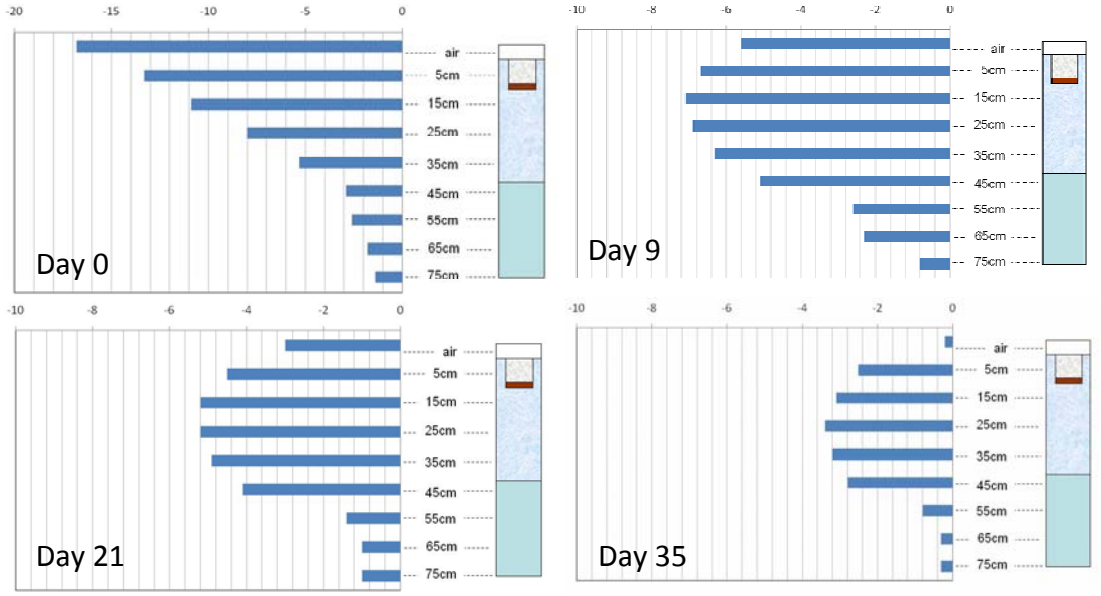

Figure 2.17 Temperature recordings (x-axis) vs ice depth (y-axis) at oil application (day 0) and the three sampling times.

Due to that the samples from the middle section of all columns by mistake were added acid prior to measurements, was the salinity measured using both a refractometer and a conductivity meter. The refractometer is not giving as accurate readings as the conductivity meter, but it was important to get a complete data set of salinity measurements. Reported results are from the measurements with refractometer are given in Figure 2.18.

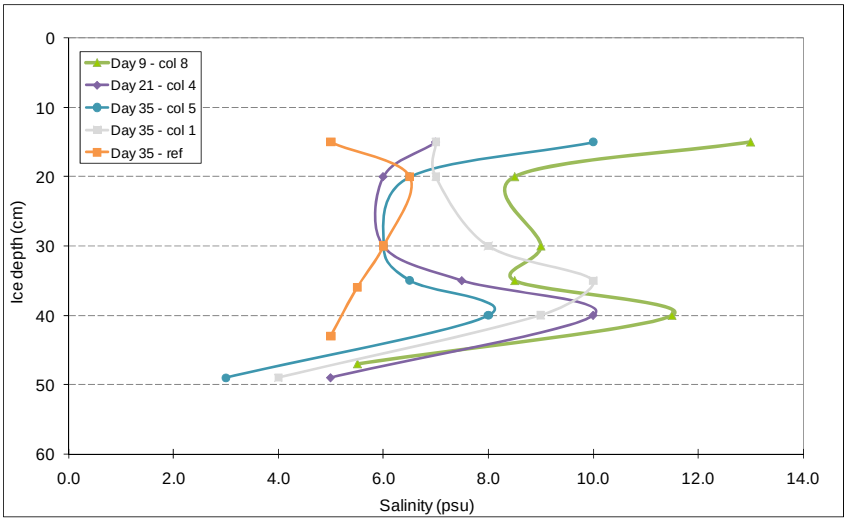

Figure 2.18 Salinity measurements with a refractometer.

The results show that the salinity is decreasing during the experimental period from day 9 to day 35. The salinity profiles with depth are C-shaped down to 40 cm, with a significant decrease in salinity in the lowest part of the columns, most likely caused by brine drainage during sampling. The measurements indicate that ice conditions in the reference column (not added oil) and col 1 were not the same as e.g. in column 5 that was sampled the same day. Figure 2.19 shows the calculated permeability (brine volume) of the ice cores. The calculations indicate that the permeability of the ice increased throughout the experiment.

The freezing and melting conditions in the ice seem to be more controlled during the experiments in phase III, both due to that the experiments were performed in a cold room with adjustable temperature, and that no unexpected power failures occurred. Examination of ice texture by thin section analysis in phase I and II have shown that columnar ice has been produced, and it is assumed that the ice in phase III has the same properties. The salinity measurements suggest that the ice conditions have changed during the experimental period, and that the ice property might not be the same in all columns.

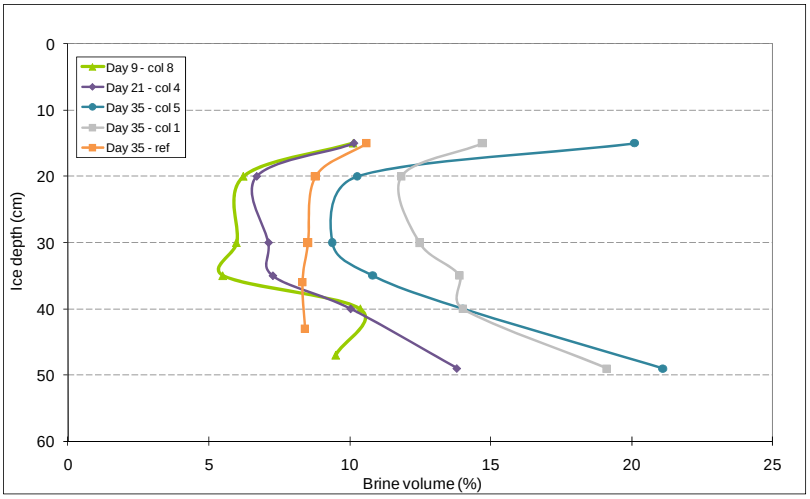

Figure 2.19 Brine volume calculated from temperature readings and salinity measurements.

2.4.3.2 Chemical analyses, phase III

The results from the chemical analyses are given in Appendix B. Table B 1 gives the content of semi volatiles in melted ice cores, Table B 2 in reference samples, and Table B 3 gives the concentrations based on calculated porosity (brine volume).

The oil was entrapped in the upper 10-15 cm of the ice core, and no visible oil droplet transport has been observed during the sample processing. However, traces of n-alkanes were detected in some of the GC/FID chromatograms. Therefore, no results from column 3 (day 21) and column 6 (day 9) are presented. The results (Figure 2.20) indicate that the concentration of WSC increased during the experiment, and was highest at last sampling point (35 d, 15-20 cm). The total SVOC concentrations in the melted ice cores were 0.05 ppb after 9 days, 0.13 ppb after 21 days, and 5.5 and 7 ppb after 35 days. The corresponding values based on porosity were 0.6, 3, and 29 and 55 µg/L brine volume.

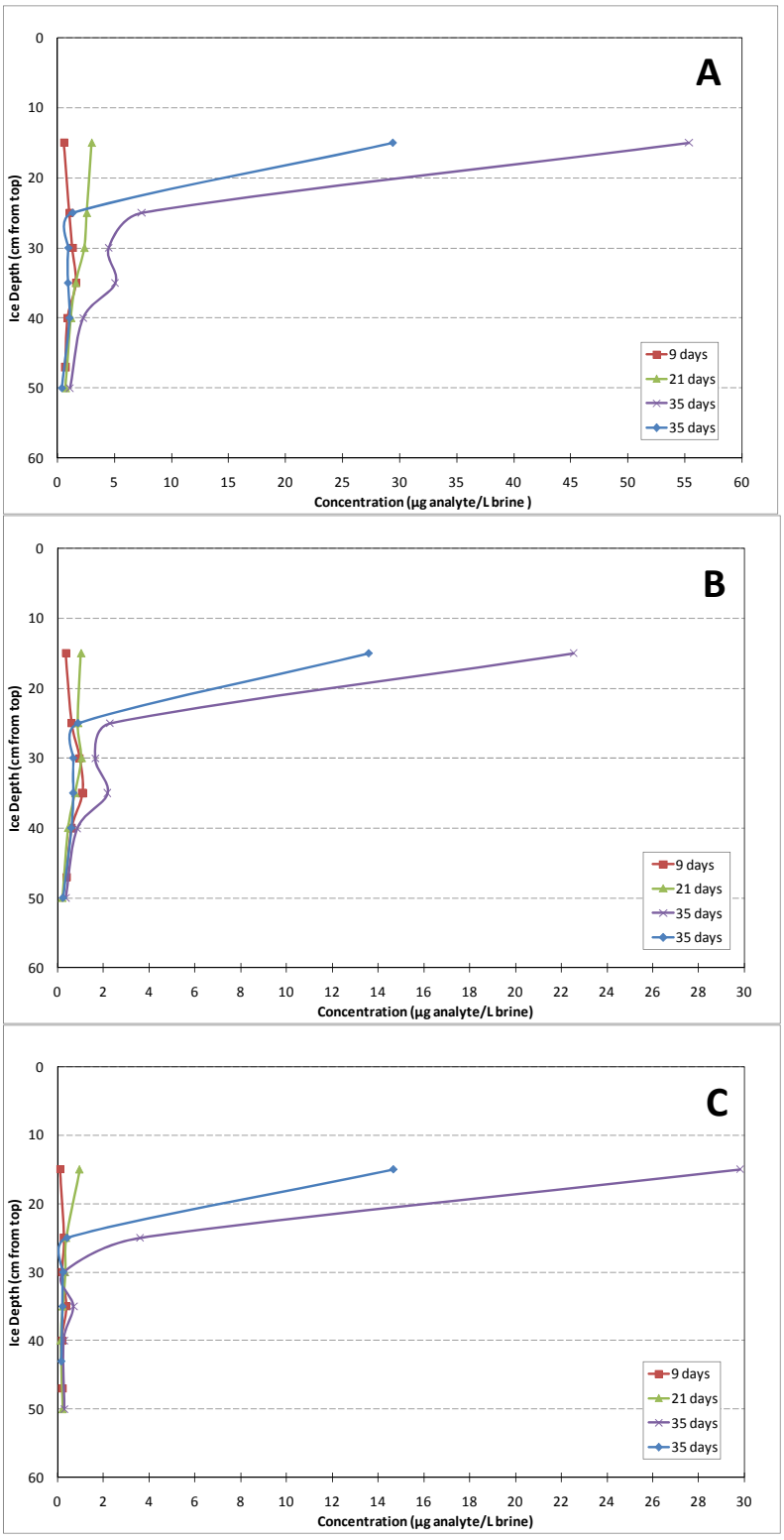

Figure 2.20 Concentrations of total SVOC (A), naphthalenes (B), and 2-3 ring PAHs in ice cores vs depth given in µg analyte/L brine volume (based on the ice core porosity). The concentrations from day 35 are from two different columns.

2.4.3.3 Estimated toxicity in the brine volume

The estimated acute toxicity to marine organisms of the WSC in the ice has been calculated (Table C 2) based on the concentration of the WSC in the brine channels and the log K_{ow} for the components and is expressing acute toxicity as hazard index (HI). A theoretic HI does not take the potential synergetic effect of the components into account, and one can not exclude that there might be non-analyzed components in the oil not included in the predictions of HI that can affect the acute toxicity.

An HI below 1 indicated that the concentration in the brine channels in the ice (5 cm sections) were not high enough to represent an acute toxicity to local marine biota. The HI values for the ice core samples are below one for all reported samples (ranging from 0.001 to 0.96). The estimated acute toxicity was highest just below the encapsulated oil in col 1 sampled on day 35, and the main contributor to the HI was the 2-3 ring PAHs. However, summarizing the HI for all samples in column 1 gives an HI of 1.1, indicating that the toxicity in the brine channels in the ice from 15 to 50 cm might be acute toxic to the ice habitants. If it is assumed that the WSC is distributed in the whole ice core, and not only in the brine channels, all samples had an HI well below 1 (ranging from 0.0001 to 0.13, results not shown). The calculation of estimated toxicities in the ice is very approximate, particularly because they are based on brine volumes and on the assumption that the transport of WSC solely happens through the brine channels. Nevertheless, these results indicate that the ice organisms might possibly be exposed to toxic WSC over several months, causing potentially toxic oil components to enter the Arctic marine food web.

2.5 Summary and conclusions

Examination of ice texture by thin section analysis in phase I and II have shown that columnar ice has been produced, and that the ice seems to be similar to natural sea ice. The salinity measurement and temperature recordings indicate that the ice conditions have changed during the experimental period resulting in ice with increased porosity when simulating spring thawing.

The laboratory experiments have shown that there is a downwards migration of water soluble oil components from oil encapsulated in the ice, and that the migrating starts after spring thawing has increased the porosity of the ice. As long as the temperature in the ice is relatively low, the migration seems to be negligible. These observations are in accordance with the findings in field experiments in first-year sea ice on Svalbard (Faksness and Brandvik, 2008a and 2008b).

An HI below 1 indicated that the concentration in the ice samples (5 cm sections) were not high enough to represent an acute toxicity to local marine biota. The HI values for the ice core samples are below one for all reported samples (ranging from 0.001 to 0.96). The experiments have demonstrated that to simulate ice growth and melting is a challenge in the laboratory. The ice growth conditions seem to be similar to natural conditions, but the melting process might be more difficult to simulate, as the experiments are performed in a closed system where natural processes such as tide movements, currents and sunlight

(albedo effect) were not included. Faksness and Brandvik (2008b) observed an upward migration of oil during their field experiments on Svalbard, but no upward transport was observed during the melting process in these laboratory experiments, indicating that the tide movement, sunlight and albedo effect are important factors that should be taken into account in future experiments.

3 Biodegradation of oil in marine ice

3.1 Introduction

The Polar sea ice contain brine channels of the ice that provide liquid niches that enable motility and respiration of microorganisms at subzero temperatures (Junge et al., 2003, 2004, 2006). The brine channels also act as a matrix for the transport of hydrocarbons (Fingas and Hollebone, 2003; Faksness and Brandvik, 2005). Under conditions with ice temperatures of -20°C and salinity conditions high as 200 ‰, laboratory experiments have shown that bacterium (*Colwellia psychroerythraea*) is able to incorporate amino acids into proteins (Junge et al., 2006). This respiration has been associated with particles or with the surfaces of the brine channels (Junge et al., 2003; Junge et al., 2004). In addition, the ability to grow at sub-zero temperatures has been demonstrated by the bacterium "*Psychromonas ingrahamii*", which has been cultured at temperatures as low as -12°C (Breezee et al., 2004).

Enzymes in bacteria isolated from sea ice may be cold-active, with catalytic activities well below the freezing point of seawater (Groudieva et al., 2004). Temperature optima and stabilities of psychrophilic proteins typically occur at lower temperatures than for mesophilic proteins. Such cold-adaptive proteins are often characterized by reduced strength of stabilizing interactions (Collins et al., 2008). Microbes exposed to large drops in temperature may produce cold shock and cold acclimation proteins (Berger et al., 1996). Psychrophilic and halophilic bacteria are also capable of adjusting the fatty acid composition and protein content composition of their membranes in such a way that the proton permeability at the respective growth temperature remains constant (Whyte et al., 1999; Chintalapati et al 2004). Several bacteria producing cryoprotecting proteins have been reported. These proteins may protect more freeze-labile proteins from freezing and thawing denaturation, or they may have protein refolding activities. Other proteins may control the generation of intracellular ice crystals (Kawahara, 2008).

It has been shown that indigenous bacteria from Polar seawater can degrade n-alkanes and PAHs at water temperatures of 4°C or lower (Michaud *et al.*, 2004; Deppe *et al.*, 2005; Gerdes *et al.*, 2005). However, no studies have been reported so far on the potential of oil biodegradation in Polar sea ice. However, some studies from oil-polluted Arctic soil have indicated slow biodegradation at subzero temperatures (Rike et al., 2003; Børresen et al., 2007). Biodegradation of oil from a helicopter accident in Antarctic lake ice cover has also been described (Jaraula et el., 2009). During a winter field study performed on Svalbard in 2004 we measured changes in n-C_{17}/Pristane and naphthalene/phenanthrene ratios during a 4-month winter experiment, indicating slow biodegradation. However, changes in these ratios were not significant (Brakstad et al., 2008).

Hydrocarbonoclastic bacteria have been isolated from Antarctic sea ice (Delille *et al.*, 1997; Fiala and Delille, 1999), and the oil infested in the ice may represent a surface on which these microbes can attach. Several types of bacteria have been shown to degrade petroleum oil hydrocarbons in marine environments at temperatures close to freezing

(Deppe *et al.*, 2005; Gerdes *et al.*, 2005). Also, catabolic genes for oil degradation (alkane mono-oxygenases and aromatic oxygenases) have been detected in hydrocarbon-contaminated and control soils from Arctic and Antarctic environments (Whyte *et al.*, 2002; Luz *et al.*, 2004). No specific cold-adaption of hydrocarbon-degrading enzymes have been described, although a study of aromatic ring hydroxylating dioxygenase peptide sequences from a cold marine environment (Patagonia) showed less than 70 % identity to previously described dioxygenases (Lozada et al., 2008).

Microbial respiration and motility in these subzero temperature environments have been observed, even down to temperatures of -20 °C, and these respiratory activities have been associated with particles or surfaces in the brine-inclusion networks of the ice (Junge *et al.*, 2003; Junge *et al.*, 2004), caused by salting-out processes during ice development. Sea ice microbes (e.g. *Psychromonas ingrahamii*) have been cultured at temperatures of at least -12 °C (Breezee *et al.*, 2004).

The pollution of cold seawater or marine ice with crude or oil compounds typically influences the microbial concentrations and community structures. The long-term effects of diesel fuel and crude oil on microbial communities were investigated over 9 months in Antarctic land-fast ice (Terre Adélie). In these studies a three orders of magnitude increase in bacterial counts occurred in sea ice contaminated with diesel and crude oil, and the proportion of oil-degrading bacteria increased from < 0.001 % (uncontaminated ice) to 10 % of the community after 30 weeks of contamination (Delille et al., 1997). In the 4-month winter field study we performed at Svalbard (Van Mijen Fjord) oil contamination resulted in 5 times higher concentrations of bacteria in oil-polluted ice than in clean reference ice (Brakstad et al., 2008). Pollution of marine ice with crude oil or oil compounds typically results in shifts of bacterial communities with a relative increase in the abundance of a few genera. Two studies from Svalbard showed that Arctic marine ice with crude oil stimulated growth of the genera *Marinobacter*, *Shewanella*, *Pseudomonas*, *Colwellia* and *Marinomonas* (Gerdes et al., 2005; Brakstad et al., 2008). Several of the bacterial phylotypes described in these studies are typically psychrophilic and associated with Polar seawater and ice in both the Arctic and Antarctic (Bowman et al., 1997; Junge et al., 2002; Brinkmeyer et al., 2003; Zeng et al., 2007).

Bioremediation of oil in marine ice is an intriguing prospect. If biodegradation could be stimulated in ice-infested oil, reducing the toxic compounds migrating out of the ice, this would be of benefit for the organisms inhabiting the polluted ice or nearby areas. Addition of the slow-release oleophilic fertilizer Inipol EAP 22 to ice-covered and ice-free Antarctic seawater enhanced both the concentrations of heterotrophic and hydrocarbon-degrading bacteria and increased the rate of biodegradation during the experiments, measured as n-C_{17}/Pristane and n-C_{18}/Phytane ratios (Delille et al., 1998). In an marine ice experiment at Svalbard with crude oil placed on the ice with or without ferilizer (Inipol EAP 22 mixed with fish meal) no stimulation occurred at temperatures below 0°C (Gerdes and Dieckmann, 2006). However, slow-release fertilizers may not be suitable for Polar regions since they may solidify at low temperatures.

3.2 Study objective

Since biodegradation of petroleum hydrocarbons at subzero temperatures have not yet been shown, the main objective of this part of the project will concentrate on the essential question: Will biodegradation *potentially* contribute to depletion of hydrocarbons in ice? In order to answer this question biodegradation experiments were designed to be conducted at controlled conditions as laboratory experiments. Since microbial activities require fluid environments we have not performed these experiments in ice, but in synthetic brines relevant for defined marine ice temperatures.

Since fertilizers may aid in the detoxification of oil compounds the potentials for the use of these in marine ice should also be of interest. Slow-release fertilizers may be problematic to use due to their high pour points, and initial experiments could therefore be performed with simple inorganic nutrient formulas in static systems.

3.3 Materials and methods

3.3.1 Seawater

Natural seawater was used as microbial source for all experiments. The seawater was collected from 90 m depth in a non-polluted Norwegian fjord (Trondheimsfjord; 63°26'N, 10°26'E). The following seawater parameters were recorded: Temperature (5.8°C), dissolved oxygen (9.07 mg/l), salinity (33.8 ‰), *o*-PO_4 (25.8 mg/l), NH_4^+ (< 5 mg/l), NO_3-NO_2 (136.8 mg/l), dissolved organic carbon (1.1 mg/l) and colony-forming units in Marin Agar 2216 (1.39 x 10^4 CFU/ml). The seawater was filtered (50 µm) to remove coarse particles.

No additional nutrients were added to the seawater, except for the salts used for the generation of artificial brines (see below).

3.3.2 Generation of artificial brines

3.3.2.1 Salts

Red Sea Salt (RSS) was provided by a local pet shop (Tropehagen AS) and is used for marine aquarium fish. Sigma Sea Salt (SSS) was proved from Sigma-Aldrich (product no. S9883).

3.3.2.2 Brine generation

Natural seawater brine was generated by freezing of seawater in buckets at different temperatures (-5, -10 and -20°C). Brines were drained off the ice at the respective freezing temperatures.

Artificial brines were prepared by salting up natural seawater, based on a salinity of 35 ‰ as Practical Salinity Unit (PSU). It was expected that salinity increases of 10‰ was generated for every 9 g l^{-1} of salt added.

The salts were mixed into the seawater by magnetic stirring at room temperature until dissolved. The artificial brines were then frozen to relevant temperatures.

3.3.2.3 Analyses of brines

Salinity was measured refractometrically.

Element analyses were conducted by High Resolution Inductive coupled plasma mass spectrometry (HR-ICP-MS; Element 2, Thermo Fisher Scientific). Seawater and brine samples were diluted 10 times and acidified with 0.1 M HNO_3. The samples were analysed against an external calibration solution of 10% Seawater "cleaned" from trace elements.

3.3.3 Biodegradation experiments 1 (BE1)

Biodegradation experiments were conducted in artificial brines at temperatures of -5 and -10°C, and in natural seawater at 5 and 0°C. The oil used for the experiments was a fresh Statfjord B crude (SINTEF ID 008-0047). Biodegradation experiments were conducted both with water-soluble fractions and thin oil films immobilised on the surface of hydrophobic adsorbents.

The microbial communities present in natural seawater were the source for biodegradation in all experiments.

3.3.3.1 Artificial brines

Sea ice brines at -5 and -10°C are expected to have a salinity of 100 ‰ and 145 ‰, respectively (Mock and Thomas, 2005). SSS was added to natural seawater at the following concentrations:

- 100 ‰: 85.65 g l^{-1}
- 145 ‰: 128.4 g l^{-1}

These amounts were based on studies and measurements described in the results where salt concentrations and salinity measurements were compared.

3.3.3.2 Water-soluble fractions (WSFs)

WSFs of the paraffinic fresh crude oil Statfjord B (SINTEF ID 008-0047) was prepared in seawater and in artificial brines.

For an oil loading of 1:1000 in seawater or artificial brines 4.375 l seawater or brine was spiked with 4.375 g oil in 5 l-bottles, while for 1:10000 oil loading 0.4375 g oil was added to the same volume of seawater or brine. The mixtures were incubated at slow

stirring (avoiding droplet generation) at 4°C for 96 hours. WSFs were removed from a tap in the bottle bottom (see Figure 3.1) distributed on 100 ml serum bottles with butyl rubber septa (appr. 80 ml in each bottle). The WAFs were incubated for up to 24 weeks, as described in Figure 3.1. Abiotic controls were prepared by adding 50 $HgCl_2$ to final concentrations of 50 mg l^{-1}.

WSFs prepared in natural seawater were incubated at 5 or 0°C for up to 8 weeks (5°C) or 24 weeks (0°C). WSFs prepared in brines with 100 ‰ at -5°C for up to 24 weeks, while WSFs in brines with 145 ‰ were incubated at -10°C for up to 24 weeks.

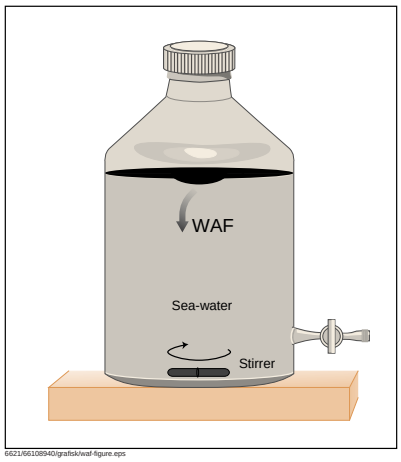

Figure 3.1 System for generation of water-soluble fractions (WSFs)

3.3.3.3 Immobilised oil

Serum bottles with butyl rubber septa were prepared with artificial brines with SSS (100 ‰ or 150 ‰), volumes of appr. 80 ml.

Squares (1 x 1 cm) of hydrophobic Fluortex fabrics (product reference 09-150/36; Sefar Inc., Thal, Switzerland) were cut and washed in dichloromethane (DCM). The fabrics consisted of filaments of tetrafluoethylene and ethylene. Volumes of 50 µl Statfjord oil was warmed (30°C for 30 minutes) and carefully added on the surfaces of sterile (autoclaved at 121°C for 15 minutes) deionised water cooled to room temperature in beakers with inner diameters of 8.5 cm (area 56.7 cm^2), resulting in an average film thickness of 10µm.

Fabrics were placed on the oil film for 30 minutes and were then carefully washed in sterile deionised water to remove excess oil. The fabrics were mounted in thin fish lines (0.030 mm) prewashed in DCM, and the fabrics were submerged in the serum bottles with artificial brines (see Figure 3.2). Fabrics in artificial brines (100 or 145 ‰) were incubated at -5°C (100 ‰) or -10°C (145 ‰) for up to 24 weeks, as described in Table 3.1. Sterile samples with 50 mg l^{-1} of $HgCl_2$ were included.

Figure 3.2 An example of a system for biodegradation studies of immobilised oil. The oil is immobilized on the absorbent submerged in the water phase. In the system shown here a CO_2 trap with potassium hydroxide is shown. This was not included in the current studies

Table 3.1 Experimental setup for BE1 for biodegradation experiments at +5 to -10°C. The set up consisted of water soluble fractions (WSFs) with initial oil-loading of 1 part to 1000 parts seawater (1:1000) or 1 part to 10000 parts seawater (1:10000). Some samples were sterile controls poisoned with $HgCl_2$. Sampling for chemical analyses (C) or microbiological analyses (M) are shown.

Temp. (°C)	**Oil or WSF**	**Oil loading**	**Sampling (weeks)**						
			0	**1**	**2**	**4**	**8**	**11**	**24**
+5	WSF	1:10000	C			C,M	C,M		
	WSF	1:10000 Sterile	C			C	C		
0	WSF	1:10000	C			C,M	C,M		C,M
	WSF	1:10000 Sterile	C			C	C		C
-5	WSF	1:1000	C		C	C,M	C,M		C,M
	WSF	1:10000	C	C	C	C,M	C,M		C,M
	Adsorbents (oil)	--	C	C	C	C	C,M	C	C;M
	Adsorbents (oil) Sterile	--	C			C	C		C
-10	WSF	1:1000	C					C,M	C,M
	WSF	1:10000	C					C,M	C,M
	Adsorbents (oil)	--	C					C,M	C,M

3.3.4 Biodegradation experiment 2 (BE2)

A biodegradation experiment was performed with and without amendment of brines with inorganic nutrients at one temperature (-5°C). Seawater with SSS was prepared at a salinity of 100 ‰, as described above.

WSFs with oil loadings of 1:1000 and 1:10000 were generated in the artificial brine as described above. Some of the WSFs were mixed with 3.27 g l^{-1} Bushnell-Haas irorganic nutrients (Difco). WSFs with and without nutrient amendment were distributed on 100-ml serum bottles with butyl rubber septa (90 ml brine). Some of the WSFs were poisoned with $HgCl_2$ (100 mg l^{-1}) as sterile controls. The WSFs were incubated for up to 12 weeks, as described in Table 3.2.

Fluortex fabrics with immobilised oil (see above) were submerged in SSS with and without amendment with Bushnell-Haas nutrients (3.27 g l^{-1}). Some of the brines were poisoned with $HgCl_2$ (100 mg l^{-1}) as sterile controls. The fabrics in the brines were incubated for up to 24 weeks, as described in Table 3.2.

Table 3.2 Experimental setup for BE2 for biodegradation at -5°C in natural seawater without added nutrients (non-amended) and with Bushnell-Haas inorganic nutrients (BH) added. The set up consisted of water soluble fractions (WSFs) with initial oil-loading of 1 part to 1000 parts seawater (1:1000) or 1 part to 10000 parts seawater (1:10000). Some samples were sterile controls (St) poisoned with $HgCl_2$. Sampling for chemical analyses (C) or microbiological analyses (M) are shown.

Temp. (°C)	**Oil or WSF**	**Oil loading**	**Sampling (weeks)**							
			0	**1**	**2**	**4**	**8**	**12**	**16**	**24**
-5 Non-amended	WSF	1:1000	C			C	C	C		
	WSF	1:10000	C, M	M	M	C, M	C, M	C, M		
	WSF	1:10000 Sterile				C	C	C		
	Adsorbents (oil)	--	C, M			C, M			C, M	C, M
	Adsorbents (oil) Sterile	--				C	C		C	C
-5 Amended BH	WSF	1/1000	C			C	C	C		
	WSF	1/10000	C, M	C, M	C, M	C. M	C. M	C. M		
	WSF	1/10000 Sterile				C. M	C	C, M		
	Adsorbents (oil)	--	C. M			C. M	C		C, M	C, M
	Adsorbents (oil) Sterile	--				C	C		C	C

3.3.5 Sampling and analyses

3.3.5.1 Sampling and chemical analyses

Samples of WSFs or fabrics were sampled as shown in Table 3.1 and 3.2. Complete volumes of WSFs were extracted in 30 ml DCM with drying agent (Na_2SO_4) for analyses of semivolatile organic compounds (SVOCs). The DCM extracts were evaporated to small volumes (100 µl) on a TurboVap 500 closed cell concentrator. A surrogate recovery standard of *o*-terphenyl was added to each sample (final concentration 20 µg ml^{-1}).

SVOC analyses were performed by GC/MS (HP 6890 gas chromatograph with HP 5973 mass selective detector; Agilent) with a HP-5MS (60 m x 0.25 µm) column, helium carrier gas (flow 1.0 ml/min), a temperature programme in the column of 40°C (1 min) – 6°C/min – 300°C (20 min), and with an injector temperature of 300°C. GC-MS analysis included naphthalene, phenanthrene, and the HC-compound groups Naph-1 (C_0-C_1 naphthalenes). Naph-2 (C_2-C_3 naphthalenes), PAH-1 (C_4-naphthalenes, biphenyl, acenaphthylene, acenaphthene, dibenzofurane, C_0- to C_1-fluorenes, C_0- to C_1-phenanthrenes/ anthracenes, C_0- to C_1- dibenzothiophenes), and PAH-2 (C_2- to C_3-fluorenes, C_2- to C_4- phenanthrenes/ anthracenes, C_2- to C_4- dibenzothiophenes, fluoranthrene, pyrene, C_1- to C_3- fluoranthrenes/pyrenes, benz[a]anthracene, C_0- to C_4-crysenes, benzo[b.k]fluoranthene, benzo[e.a]pyrene, perylene, dibenzo[a.h]anthracene, benzo[g.h.i]perylene, indeno[1.2.3-c.d]pyrene).

Fluortex fabrics were removed from the serum bottles as described in Table 3.1 and 3.2 and were transferred to 30 ml DCM with drying agent (Na_2SO_4) for GC-FID analyses. The DCM extracts were evaporated to small volumes (100 µl) and a surrogate recovery standard added as described above for the WSFs. Determination of C_{10}-C_{36} total extractable organic carbon (TEOC). C_{10}-C_{36} *n*-alkanes and *n*-hexadecane in DCM extracts was performed by GC-FID analysis (HP Model HP5890II gas chromatograph with a flame ionisation detector; Agilent Technologies), using a Durabond DB-5 (15 m x 0.25 µm i.d.) column, hydrogen carrier gas (flow 2.2 ml/min), and a temperature programme of 40°C (5 min) - 6°C/min – 310°C (10 min) splitless in 40 sec.

3.3.5.2 Microbiology analyses

Samples for microbiology analyses were collected as described in Table 3.3 and 3.4.

Total numbers of microbial cell were enumerated by epifluorescence microscopy (DAPI). Dilutions were prepared from 10 ml brine or seawater, stained with DAPI, filtered on a black polycarbonate filter (0.2 µm) and analysed in oil immersion fluorescence microscopy at 1250 times magnification.

For determination of heterotrophic bacteria samples 10-fold dilutions of samples in sterile seawater were prepared and 0.2 ml of each dilution inoculated (triplicate) in 1.8 ml of Marine Broth 2216 (Difo Laboratories, Detroit, Mi, U.S.A). After incubation for 14 days

at 4°C most probable number (MPN)-determinations were determined (Rand et al., 1975).

3.3.5.3 PCR-DGGE

Changes in bacterial community structures during biodegradation were measured by polymerase chain reaction (PCR) amplification of bacterial 16S rDNA and denaturing gradient gel electrophoresis (DGGE).

Samples of WSFs in brines (100-200 ml) were filtered through Sterivex filter funnels (exclusion 0.2 µm), and 2 ml of a lysis agent was added to the filter cartridges (Millipore). The lysis buffer in each Sterivex filter was incubated with lysozyme (2 mg) at 37 °C for 30 min, followed by Proteinase K (1 mg) and SDS (1 % [wt/vol]) at 55 °C for 2 hours. The lysate was transferred to sterile tubes, the Sterivex filters washed with 1 ml lysis buffer, and the pooled solution (3 ml) from each filter was extracted twice with 6 ml hot (60°C) phenol-chloroform-isoamylalcohol (25:24:1), pH 8.0, as described by Sambrook et al, 2001. The extracted water phases were precipitated with 2.5 volumes of ethanol (96 %) at -20 °C (3 h) and were then centrifuged (4000 x g; 5 minutes). The pellets were washed (75 % ethanol), recentrifuged, dried (N_2), and dissolved in 100 µl ultra-pure water (Biochrom AG, Berlin, Germany). Nucleic acid extracts were stored at –20 °C. PCR amplification of 16S rRNA gene fragments was performed with bacterial domain-specific primers GM5F (5'-CCT ACG GGA GGC AGC AG-3') and SD907-r (5'-CCC CGT CAA TTC CTT TGA GTT-3') (Muyzer et al., 1993; Teske et al., 1996), yielding a PCR fragment of 550 bp. For DGGE a 40-mer GC-clamp (5'- CGC CCG CCG CGC GCG GCG GGC GGG GCG GGG GCA CGG GGG G-3') was added to the 5'-end of the GM5F primer (Muyzer et al., 1993). PCR was run in 50 µl mixtures, containing 2 µl DNA template, 200 µM of each d'NTP, 0.5 µM of each primer, PCR buffer (10 mM Tris-HCl, pH 8.3; 50 mM KCl; 1.5 mM $MgCl_2$), and 2.5 U *Taq* DNA polymerase (Qiagen GmbH, Hilden, Germany). The PCR mixtures were heated (95°C; 2 minutes), followed by 30 cycles, each consisting of DNA denaturation (95°C; 1 min), annealing (55°C; 1 min), and DNA synthesis (72°C; 1 min), followed by a final extension (72°C; 7 min) and cooling (4°C).

The adsorbent (Fluortex) samples were extracted by ml hot (60°C) phenol-chloroform-isoamylalcohol (25:24:1), pH 8.0, as described above (Sambrook et al, 2001).

DGGE was performed with a continuous gradient of 20-70 % of the denaturing agents urea and formamide (100 % denaturants corresponded to 7 M urea and 40 % deionised formamide), essentially as described by Teske et al (1996). Each gel well contained 0.5-1.0 µg DNA. DGGE was run at 60°C in a DCode Universal Mutation Detection System (Bio-Rad, Hercules, CA, USA) at 150 V constant voltage for 4.5 hours. Gels were stained for 20-30 minutes with SYBR Gold (Molecular Probes. Leiden, The Netherlands), and stained gels were scanned in a GelDoc system (Bio-Rad).

3.4 Results and discussions

The results described here are from three separate experiments, one initial study to decide on the generation of synthetic brines, and two separate biodegradation studies in synthetic brines at subzero temperatures, or in cold seawater.

3.4.1 Generation of synthetic brines

Salinities at -6, -10 and -21°C are expected to be 100, 145 and 216 ‰, respectively (Mock and Thomas, 2005).

In an initial experiment seawater salts from two sources were compared for synthetic brine generation.

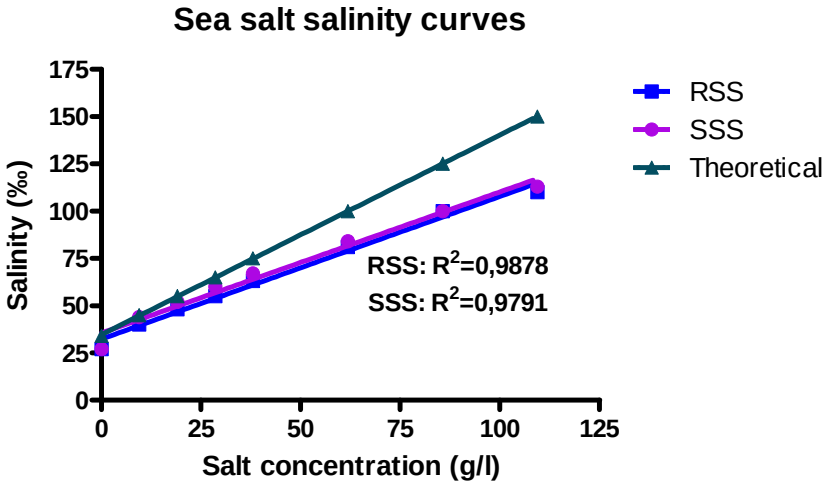

Figure 3.3 Measured and theoretical salinities at different concentrations of marine salts added to normal seawater. Two salts were compared, Red Sea Salt (RSS) from a local pet shop and Sigma Sea Salt (SSS).

Two salts were compared, Red Sea Salt (RSS) and Sigma Sea Salt (SSS). The salts were added to normal seawater in concentration ranges of 0 to 110 g/l, which should correspond to theoretical salinities of 34 to 150 ‰. The added sea salts showed similar salinities, but somewhat lower than the expected when compared to the theoretical curve. (Figure 3.3).

Based on the actual measurements above brines were generated to represent marine ice temperatures of -6 and -10°C, respectively. For these temperatures the expected salinities were 100 and 145‰, respectively, and the added amounts of salts were as follows, based on the refractometer measurements:

- 100 ‰ (PSU): 85.65 g l^{-1} in natural seawater
- 145 ‰ (PSU): 128.4 g l^{-1} in natural seawater

An element analysis was performed on the synthetic brines prepared in seawater and with salinities of 100 and 145 ‰. For salinity comparison natural brines were drained off marine ice generated at -5°C and -10°C. The concentrations of 25 selected elements were compared in the natural and synthetic brines by ICP- MS analyses (Table 3.3)

Table 3.3 Measured element concentrations (µg/l) in natural brine (NB) and in and artificial brines of Res Sea Salt (RSS) and Sigma Sea Salt (SSS) at -5 and -10°C.

	-5°C			-10°C		
Element	**NB**	**SSS**	**RSS**	**NB**	**SSS**	**RSS**
Al	27.55	3.78	646.87	55.55	320.01	795.55
B	14223.39	17467.70	16343.62	21484.40	23829.13	17254.70
Ba	21.71	37.35	56.02	36.30	50.05	55.60
Br	131503.88	200373.03	183440.49	282046.12	332123.57	162664.04
Ca	1262040.7	949376.26	1512122.4	1860677.1	1313607.8	1545968.8
Cl	63306543	67988551	68899688	97339107	91603184	65291732
Co	0.04	0.23	0.46	0.11	0.50	0.52
Cs	0.96	1.87	3.11	1.36	2.54	3.52
Cu	0.50	11.13	49.99	1.09	15.96	55.98
Fe	6.70	2.69	51.62	7.54	14.84	30.35
K	1134525	1256403	1342607	1737642	1814533	1368817
Li	560.64	907.97	614.78	869.87	1242.12	626.05
Mg	3791414	3693494	4151928	5801538	5147818	4308166
Mn	0.92	51.31	60.21	0.78	73.52	64.73
Mo	22.74	13.63	29.18	32.86	16.55	32.61
Na	31266241	33468380	34302833	48315716	47169018	34644436
Ni	1.34	7.10	12.94	1.97	12.09	12.65
P	99.41	43.00	64.12	115.02	51.47	115.36
Pb	1.11	0.78	4.25	0.34	0.01	4.17
Rb	336.81	259.74	548.80	493.23	365.52	583.11
S	2849931	3286446	3147897	4255366	4472005	3259439
Se	0.27	1.05	0.76	1.79	0.70	2.26
Si	115.20	388.99	493.68	673.80	85.68	438.70
Sr	22158.78	26166.31	33388.76	33563.36	36374.32	34022.74
Zn	0.77	13.57	11.53	1.89	14.81	19.37
SUM	103779779	110888403	113592900	159649436	151914760	110635343

When the sums of elements were compared the deviations were smaller between the sums of elements when natural brines and SSS were compared than when natural brines and RSS were compared. One-way ANOVA analyses (Dunnett's Multiple Comparison Test) also showed that mean differences were smaller between natural brines and SSS than between brines and RSS, although differences were not significant ($P>0.05$) for any of the comparisons. It was therefore decided to use the SSS for generation of artificial brines in the biodegradation experiments.

3.4.2 Biodegradation experiment 1 (BE1)

In BE1 WSFs were prepared from Statfjord oil with oil-loadings of 1:1000 and 1:1000. The same oil was immobilised as thin films on the surface of hydrophobic adsorbents. The samples were examined by chemical and microbiological analyses as shown in Table 3.1.

3.4.2.1 Depletion in water-soluble fractions (WSFs)

WSFs were generated in seawater and artificial brines at nominal salinities of 100 and 145 ‰ (PSU). The WSF concentrations are shown in Figure 3.4. The results showed that the WSF concentrations were considerably lower in the brines than in the seawater. Brines with oil-water ratios of 1:1000 showed lower concentrations than seawater with a ratio of 1:10000. No obvious differences in WSF concentrations were measured between comparable brines with different salinities.

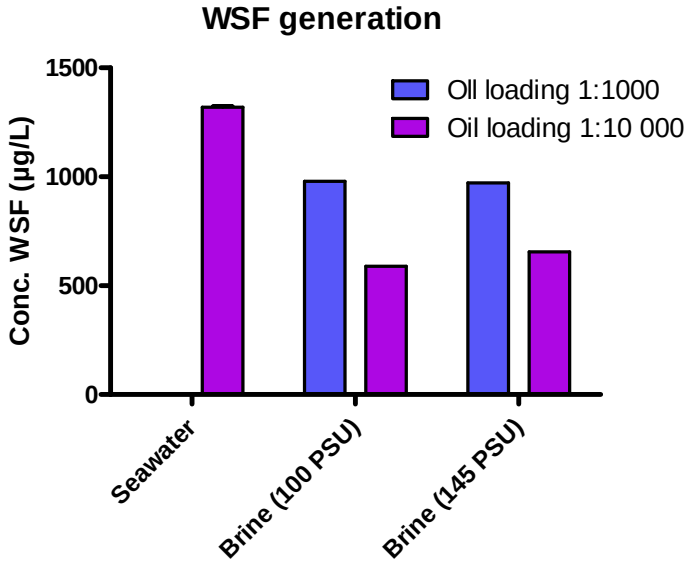

Figure 3.4 Concentrations of total GC/MS target analyses in WSFs generated in seawater and brines at a temperature of 4-5°C over a period of 96 hours. Two oil-water rations (oil-loadings) were used, 1:1000 and 1:10000. In seawater WSF was only prepared with oil-loading 1:10000.

The results from GC/MS analyses of WSFs during the biodegradation experiment are shown in Figure 3.5.

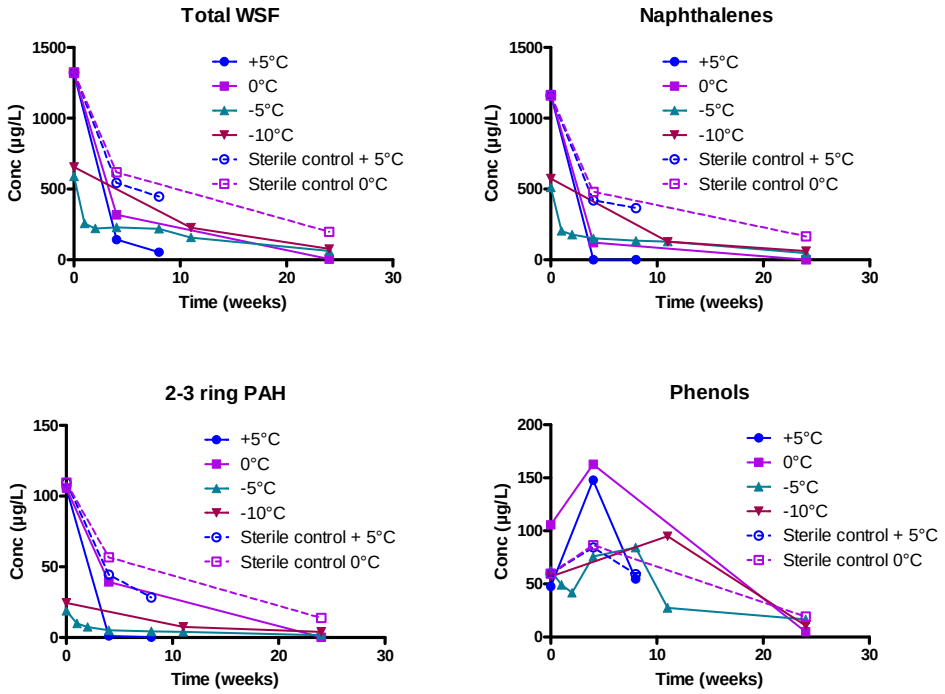

Figure 3.5 Concentrations of total GC/MS target analytes, C0-C4 naphthalenes, 2-3 ring PAH and C0-C4 phenols in the WSFs during the biodegradation experiment. The results are shown for an oil loading of 1:10 000.

All samples showed an immediate depletion after the start of the biodegradation experiment for total WSFs, naphthalenes and PAH compounds. This was shown both for biotic samples and sterile controls. This depletion was rapid in both in seawater and brines and was probably the result of evaporation, since the test systems included some headspace. Further, the oil used in these studies contained considerable amounts of volatile organic compounds (Hokstad et al., 1999). Despite the WSF reductions in all samples, the depletion of compounds was less in the sterile controls than in their corresponding samples in seawater (+5 and 0°C). The depletion in seawater at these temperatures is mostly in agreement with previous studies in our laboratory (Brakstad and Bonaunet, 2006). The depletion rates of compound groups in biotic and sterile systems are shown in Table 3.4. However, the results for phenols showed a temporary increase in the concentrations during the first 2-8 weeks. Also here these trends were shown both for biotic samples and sterile controls, although to a lesser extent in the sterile controls than in their corresponding biotic samples. We have previously observed dramatic temporary increases in phenol concentrations as the results of biodegradation processes (Brakstad et al., 1999). The results shown here therefore indicated biodegradation processes in the samples. We expected that the phenols, at least partly, are metabolites from degradation of monoaromatics (BTEX), explaining that the total GC/MS concentration in the WSFs were measured as higher at the end than at the start of the experiment, since BTEXs were not included in the GC/MS analyses. In previous studies we have not observed temporary increases in phenol concentrations in sterile

controls. Thus, the results here may therefore indicate that sterile controls actually contained viable bacterial concentrations able to metabolize hydrocarbon compounds, although to a modest degree compared to the comparable biotic samples.
The comparison of depletion at different oil loadings (1:1000 and 1:10 000) in brines at -5 and -10°C are shown in Figure 3.6.

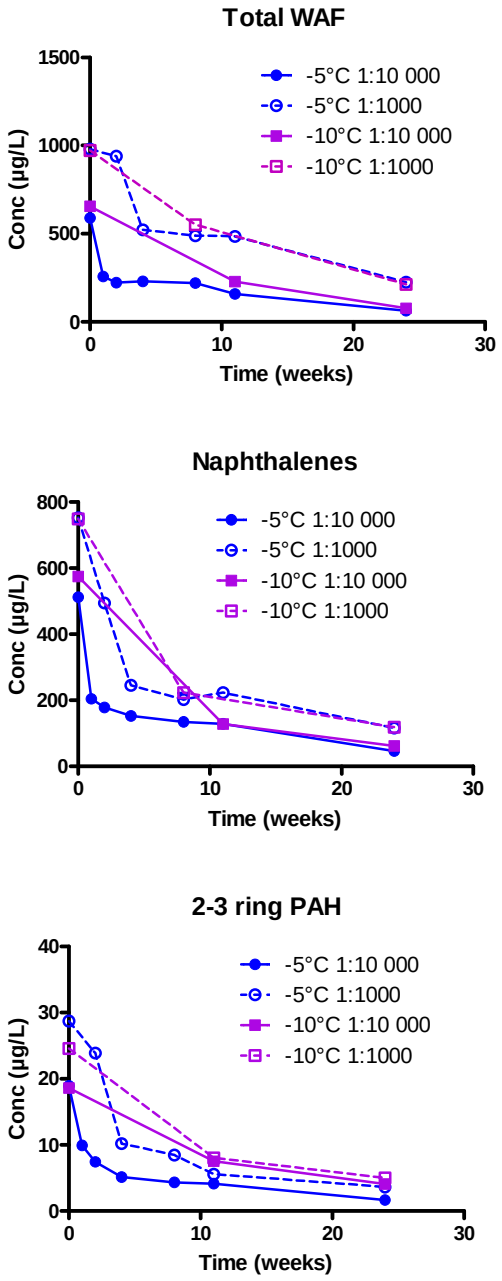

Figure 3.6 Concentrations of total GC/MS target analytes, C0-C4 naphthalenes and 2-3 ring PAHs in the WSFs during the biodegradation experiment. The results are compared for oil loadings of 1:1000 and 1:10 000.

Table 3.4 Calculations of first-order reaction kinetics for depletion of target analytes in biotic and "sterile samples". The results are shown for the complete GC/MS target analytes (WSF), C0-C4 naphthalenes and 2-3 ring PAH compounds.

Analytes	Temp. (°C)	C_0 (µg/l)	K weeks^{-1}	Half-life (weeks)	R^2
WSF (1:10 000)	+5	1315	0.6454	1.1	0.9999
WSF (1:10 000) – sterile contr	+5	1324	0.5241	1.3	1.0000
WSF (1:10 000)	0	1315	0.3578	1.9	1.0000
WSF (1:10 000)- sterile control	0	1324	0.2454	2.8	1.0000
WSF (1:10 000)	-5	586	1.2190	0.6	0.7922
WSF (1:1000)	-5	996	0.1243	5.6	0.9180
WSF (1:10 000)	-10	655	0.1019	6.8	0.9994
WSF (1:1000)	-10	970	0.0805	8.6	0.9934
Naphthalenes (1:10 000)	+5	1167	2.1290	0.3	1.0000
Napht (1:10 000)- sterile contr	+5	1160	0.6450	1.1	1.0000
Naphthalenes (1:10 000)	0	1167	0.5649	1.2	1.0000
Napht (1:10 000)- sterile contr	0	1160	0.2867	2.4	1.0000
Naphthalenes (1:10 000)	-5	507	1.1530	0.6	0.8937
Naphthalenes (1:1000)	-5	752	0.3112	2.2	0.9608
Naphthalenes (1:10 000)	-10	574	0.1776	3.9	0.9998
Naphthalenes (1:1000)	-10	749	0.2214	3.1	0.9986
PAH (1:10 000)	+5	106	1.2070	0.6	1.0000
PAH (1:10 000)- sterile control	+5	1160	0.6450	1.1	1.0000
PAH (1:10 000)	0	106	0.2468	2.8	1.0000
PAH (1:10 000)- sterile control	0	1160	0.2867	2.4	1.0000
PAH (1:10 000)	-5	19	0.6864	1.0	0.9460
PAH (1:1000)	-5	30	0.2226	3.1	0.9541
PAH (1:10 000)	-10	25	0.1497	4.6	0.9956
PAH (1:1000)	-10	25	0.1588	4.4	0.9930

Results of Table 3.4 showed that most of the curves fitted a first-order rate kinetics degradation curve well (R^2-values equal or close to 1.000). When data for biotic and "sterile" controls were compared the depletion rates were higher for most biotic samples, with the exception of 2-3 ring PAH at 0°C.

When temperatures were compared for brines samples the reductions of temperatures from -5 to -10°C also resulted in reduced depletion rates. It was also observed that depletion rates at 0°C were lower than at 5°C.

In general, the depletion rates declined with reduced temperatures, with the exception of rates at -5°C and oil-loading 1:10 000. Reductions in depletion rates were observed in seawater from +5 to 0°C, and in brines from -5 to -10°C. However, at -5°C and with oil-loading of 1:10 000, the depletion rates were faster than at higher temperatures. It was difficult to compare the rates between samples in seawater and brines. One reason for this may be that initial concentrations of target analytes in WSF differed, as described above.

An effect of concentration was also measured. WSFs from oil-loadings of 1:1000 mostly resulted in lower depletion rates than 1:10 000 oil loading, i.e. higher initial concentrations of target analytes resulted in reduced depletion rates. The exceptions were naphthalenes and 2-3 ring PAHs at -10°C, where depletion was comparable for the two oil-loadings. The mechanisms of depletion may be both evaporation and biodegradation. However, since the depletion was most pronounced between 0 and 7 days we expect evaporation to be the main depletion mechanism. For the seawater systems (+5 and 0°C) it may be possible to compare the depletion rates in biotic and sterile samples to correct for abiotic depletion. However, it was observed increased phenol concentrations in sterile controls, indicating that these samples actually were not sterile, although phenol accumulation was smaller than in comparable biotic samples. Thus, correcting for abiotic samples may therefore result in an underestimation of biodegradation rates in the seawater systems.

The comparison of depletion in seawater and brine systems may be problematic. Unfortunately we did not include sterile controls for brine solutions, and the surprisingly high depletion rates in brines from -5°C also indicate that evaporation may be a major depletion mechanism. Another possibility is the high salt concentrations may have affected extraction efficiencies, although this should be similar for all brine samples.

3.4.2.2 Depletion from oil films

Experiments were conducted with immobilized oil films submerged in brines at -5 and -10°C for 24 weeks. Adsorbents with immobilized oil films were removed for solvent extraction at intervals and the extracts analyses for total n-alkanes (*n*C10 – *n*C40). The results for n-alkanes are shown in Figure 3.7. The results showed an initial depletion in the experiments performed at both temperatures, but also in the sterile controls. This may be the results of immediate dissolution of compounds to the water phase. The results also showed variations between some replicates (error bars), and sample-to- sample variations between samples collected from the time series (exemplified with the variations in the sterile control).

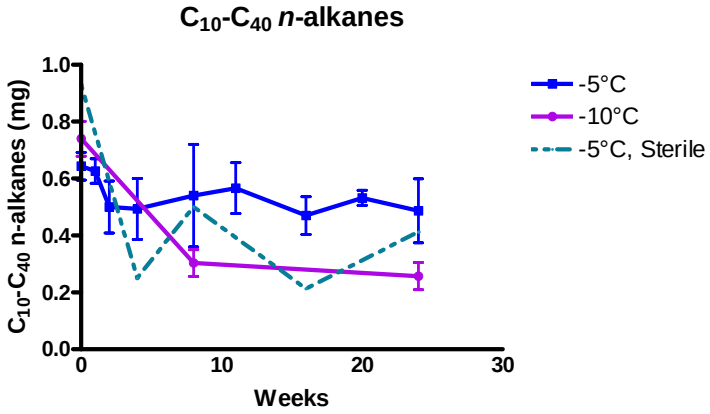

Figure 3.7 Results for C10-C40 n-alkane analyses of immobilized oil film extracts from fabrics with immobilized oil. The error bars of the biotic samples represent standard deviations (sterile control only one replicate).

The *n*C17/Pristane and *n*C18/Phytane results are shown in Figure 3.8. No biodegradation was observed, and this was confirmed for first-order rate kinetics, showing ambiguous results (not shown). We have previously demonstrated that these ratios are dramatically reduced after 4-8 weeks when biodegradation experiments have been conducted in seawater at +5 and 0°C (Brakstad and Bonaunet, 2006).

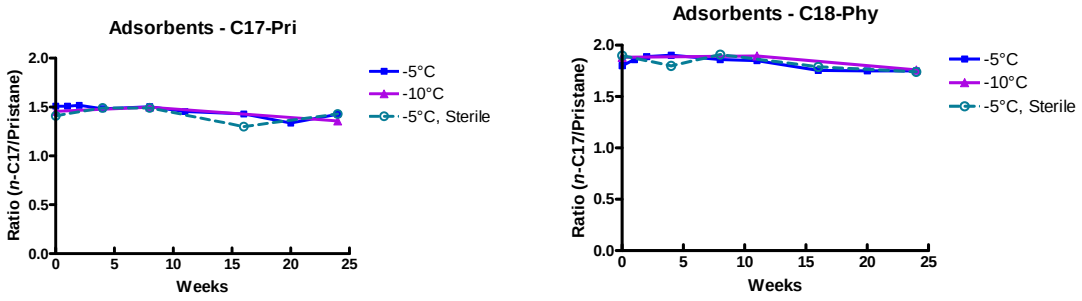

Figure 3.8 The ratios between *n*C17 and Pristane and *n*C18 and Phytane in oil immobilised on the Fluortex adsorbents.

We may assume that at the temperatures used in the current experiment, which are close to or below pour point for this oil, the characteristics of this oil is not optimal for biodegradation by psychrophilic bacteria, due to high viscosity or oil solidification.

3.4.2.3 Microbiological analyses

Microbiological analyses were performed by epifluorescence microscopy with the fluorescent DNA-stain DAPI. The results of Figure 3.9 showed rapid increases in bacterial populations in the seawater experiments (+5 and 0°C), although the concentrations rapidly decreased at in the experiments at 0°C after 8 weeks. Also in the brines at -5°C the concentrations increased during the experiment, from 6.2 x 10^4 cells/ml to 21 x 10^4 to 26 x 10^4 cells/ml. However, for the experiments at -10°C the concentrations decreased from the start to the end of the experiment.

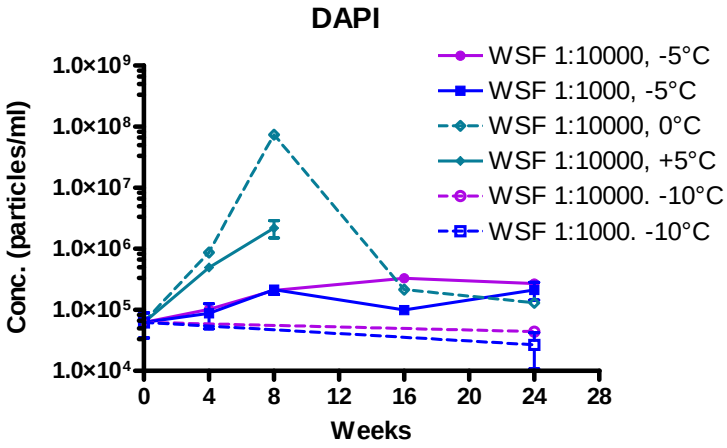

Figure 3.9 Bacterial concentrations in WSFs during biodegradation experiments determined by epifluoroscence microscopy with DAPI-stain.

Changes in bacterial communities were analyzed by PCR-DGGE of bacterial 16S rDNA during the experiment were investigated in the WSFs (Figure 3.10) and oil films (Figure 3.11).

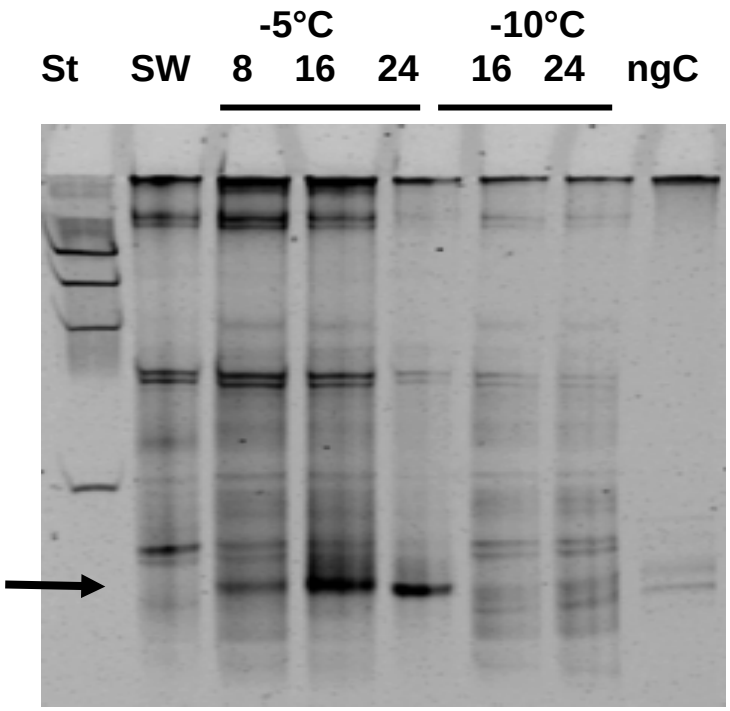

Figure 3.10 Bacterial PCR-DGGE of DNA extracted from WSFs. Only samples from WSFs with oil-loading 1: 10000 were used. The results are shown for normal seawater (SW), and from brines incubated at -5 and -10°C for 8, 16 and 24 weeks. The negative control (ngC) represents DNA extractions of blank samples at week24, while St represent a molecular weight standard.

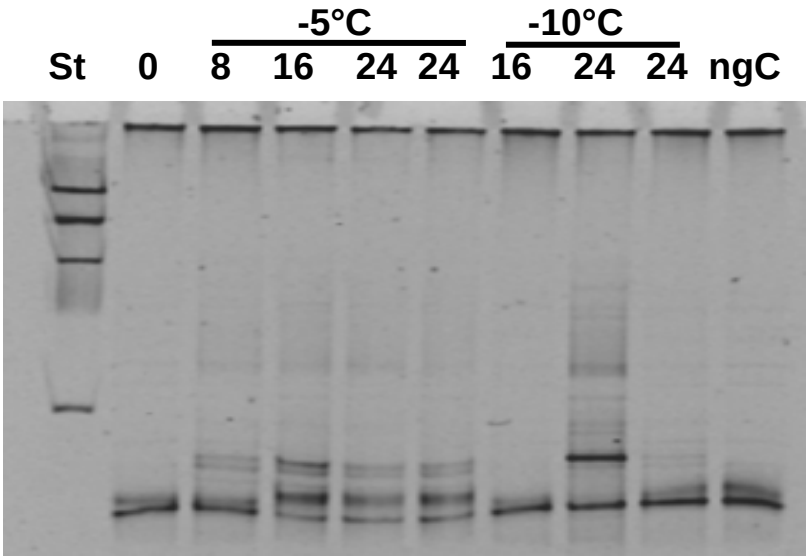

Figure 3.11 Bacterial PCR-DGGE of DNA extracted Fluoretex fabrics (immobilized oil). The results are shown for fabrics placed in brines at -5 and -10°C for 0, 8, 16 and 24 weeks. Duplicate samples were collected and analyzed after 24 weeks of incubation. The negative control (ngC) represents DNA extractions of blank samples at week24, while St represent a molecular weight standard**.**

The results showed that some changes in DGGE patterns appeared in the WSFs when compared to seawater (SW). One strong band (see Figure 3.10 arrow) appeared in brines at -5°C and remained strong for the whole degradation period. The banding patterns of the -10°C samples were weaker, but also here it seemed that unique bands emerged when compared to the seawater. Most of the seawater bands also persisted in the brine samples, indicating bacterial survival and no cell lysis.

The results from the immobilized oil (Figure 3.11) showed poorer bacterial diversities on the oil films than in the WSFs, as expected. The patterns appearing at week 0 (-5°C) and week 16 (-10°C) were similar to the negative control (ngC), but new bands emerged after 8 weeks at -5°C and 24 weeks at -10°C. The pattern at -5°C seemed to persist throughout the degradation period (16 and 24 weeks). While replicate samples seemed to be comparable for samples at -5°C, differences appeared for the 24-week samples at -10°C. Thus, the DGGE results showed that bacteria attached to the oil surface (and probably metabolized some of the oil compounds), although this was not detected by the GC-FID analyses.

3.4.3 Biodegradation experiment 2 (BE2)

3.4.3.1 Depletion of water-soluble fractions

As described above the results from the biodegradation experiments in brines were not conclusive with respect to oil compound biodegradability in brines at -5 and -10°C. An

additional experiment was therefore conducted in brines at -5°C. In this experiment the difference between brines with additional nutrient supply and brines amended with extra inorganic nutrients were investigated. In BE1the depletion in brines were difficult to interpret because sterile controls for brines were not included, and biological activity was indicated in these controls. Therefore concentration of biocide ($HgCl_2$) was increased from 50 to 100 mg/l and the sterile controls were included for the brines for both non-amended and amended brines. The experiments with WSFs were run for a shorter period in BE2, than in BE1, i.e. for 12 weeks. The concentrations of total target analytes, C0-C4 naphthalenes, 2-3 ring PAHs and C0-C4 phenols in the WSFs are shown in Figure 3.12, and first-order rate kinetics in Table 3.5.

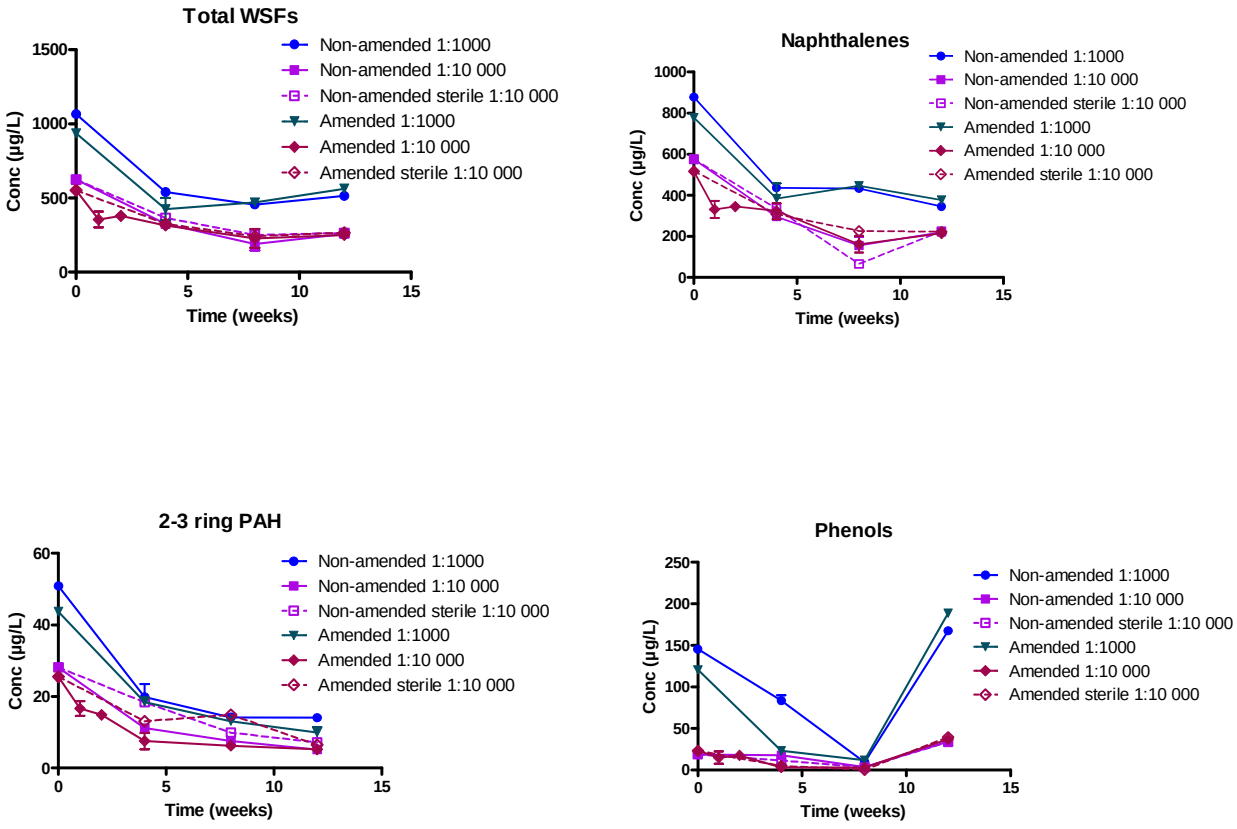

Figure 3.12 Concentrations of total GC/MS target analytes (toal WSFs), C0-C4 naphthalenes, 2-3 ring PAH and C0-C4 phenols in the WSFs during BE2.

Table 3.5 Calculations of first-order reaction kinetics for depletion of target analytes in biotic and "sterile samples" in BE2. The results are shown for the complete GC/MS target analytes (WSF), C0-C4 naphthalenes (Naphth) and 2-3 ring PAH compounds. The biodegradation experiments were conducted at -5°C.

Analytes	C_0 (µg/l)	K weeks^{-1}	Half-life (weeks)	R^2
WSF Non-amended (1:1000)	1066	0.6192	1.1	0.9774
WSF Non-amended (1:10 000)	628	0.3822	1.8	0.8572
WSF Non-amended (1:10 000)-sterile control	625	0.2995	2.3	0.9908
WSF Amended (1:1000)	937	Ambiguous	--	--
WSF Amended (1:10 000)	492	0.4070	1.7	0.5879
WSF Amended (1:10 000)- sterile C	553	0.3639	1.9	0.9873
Naphth Non-amended (1:1000)	876	0.5044	1.4	0.9483
Naphth Non-amended (1:10 000)	581	0.3579	1.9	0.8539
Naphth Non-amended (1:10 000)-sterile control	583	0.2832	2.4	0.8394
Naphth Amended (1:1000)	779	Ambiguous	--	--
Naphth Amended (1:10 000)	445	0.2614	2.7	0.6332
Naphth Amended (1:10 000)-sterile control	518	0.2915	2.4	0.9970
PAH Non-amended (1:1000)	51	0.4539	1.5	0.9281
PAH Non-amended (1:10 000)	28	0.3225	2.1	0.9753
PAH Non-amended (1:10 000)-sterile control	28	0.1174	5.9	0.9929
PAH Amended (1:1000)	44	0.3328	2.1	0.9708
PAH Amended (1:10 000)	25	0.4458	1.6	0.8797
PAH Amended (1:10 000)-sterile control	25	0.1715	4.0	0.8565

The results showed depletion in all samples, also for the "sterile controls". The phenol curves (Figure 3.12) showed significant increases at the last sampling date (12 weeks), and some increase was observed also for the controls.

The depletion rates were smaller for controls than for comparable biotic systems (Table 3.5), indicating that the biocides at least delayed depletion in these samples. The exception was analyses of naphthalenes in amended samples. The differences in depletion rates between controls and biotic samples therefore indicated that biodegradation actually took place in these samples. The depletion rate differences between biotic samples and controls, and the accumulations of phenols, both supported biodegradation of hydrocarbons in WSFs in brines.

Comparison of oil loadings showed that depletion often was reduced at the lower concentrations of target analytes (e.g. for WSFs and naphthalenes). This was not in

agreement with the results from BE1, where higher oil loading resulted in lower depletion rates (see Table 3.4).

The comparison of depletion rates between non-amended and amended samples did not support any added nutrient impact on biodegradation in the brines at subzero temperatures, and it was not possible to determine any effect at all from the addition of Bushnell-Haas medium to the brines.

3.4.3.2 Depletion from oil films

Thin oil films were immobilized on hydrophic Fluotex fabrics as in BE1, and the effects of inorganic nutrient amendment investigated during a period of 24 weeks in the artificial brines at -5°C. The results for C10-C40 *n*-alkanes are shown in Figure 3.13 and the nC17/Pristane and nC18/Phytane ratios are shown in Figure 3.14. No depletion rates were possible to determine for the C10-C40 *n*-alkanes and the *n*C17/Pristane and *n*C18/Phytane ratios.

The results from BE1 and BE2 were in agreement, showing no biodegradation of oil film n-alkanes in the brines at the tested sub-zero temperatures.

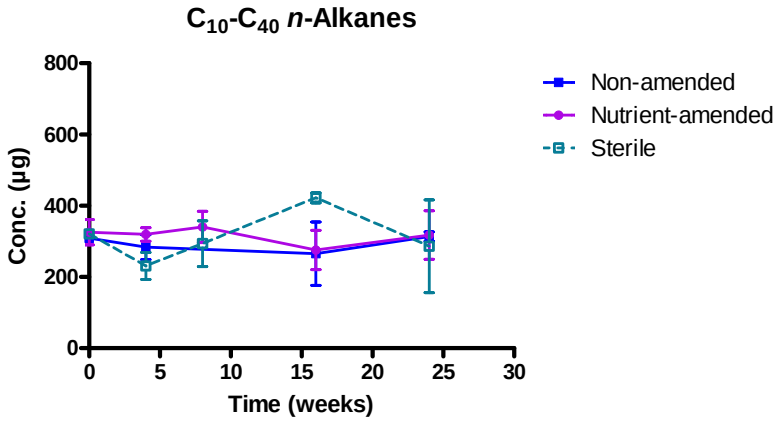

Figure 3.13 Results for C10-C40 n-alkane analyses of immobilized oil film extracts from fabrics with immobilized oil. The error bars of the biotic samples represent standard deviations (sterile control only one replicate).

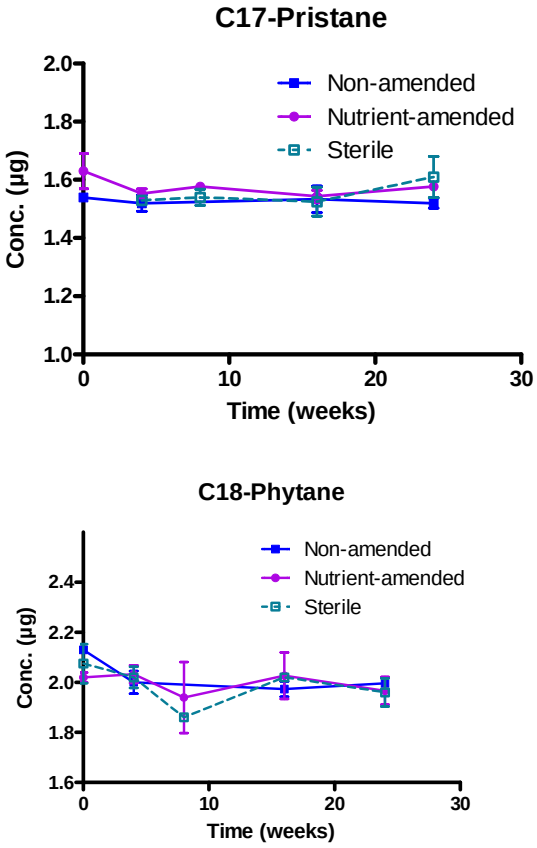

Figure 3.14 The ratios between *n*C17 and Pristane and *n*C18 and Phytane in oil immobilised on the Fluortex adsorbents.

3.4.3.3 Microbiology analyses

Results from epifluorescence microscopy (Figure 3.15) results showed that microbial concentrations remained fairly stable in the brines during the experiment. Interestingly, when sterile controls were counted, microbial concentrations also remained in these samples, and even increased towards the end of the experiment. This indicated that the biocide was not lethal to the complete populations in the brines, and were even stimulated at the end of the experiment, confirming that biodegradation of hydrocarbons actually took place also in the controls.

A DGGE analysis of bacterial PCR-products was performed to analyse the bacterial communities in the brines, by extracting DNA from the water phase in the samples with immobilised oil on fabrics (Figure 3.16). The results showed stronger banding intensities in the non-amended than in the amended samples, but some of the same main DGGE-bands seemed to be present in both samples with and without nutrients. Towards the end of the experimental period the amended samples were dominated by one DGGE-band, indicating poor diversity and the predominance of the one bacterial phylogenetic group. The negative controls showed only traces of DGGE bands. The DGGE-patterns seemed

to change from week 0 to week 4 in non-amended samples, while samples from week 16 and 24 showed similar patterns, although some minor banding changes also appeared after week 4.

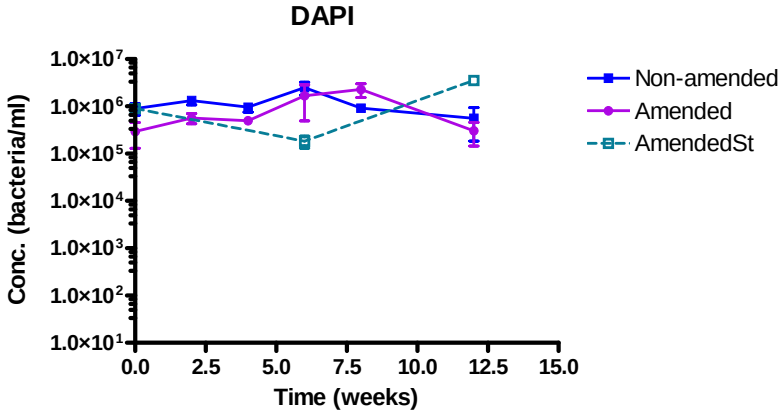

Figure 3.15 Bacterial concentrations in WSFs during biodegradation experiments determined by epifluoroscence microscopy with DAPI-stain.

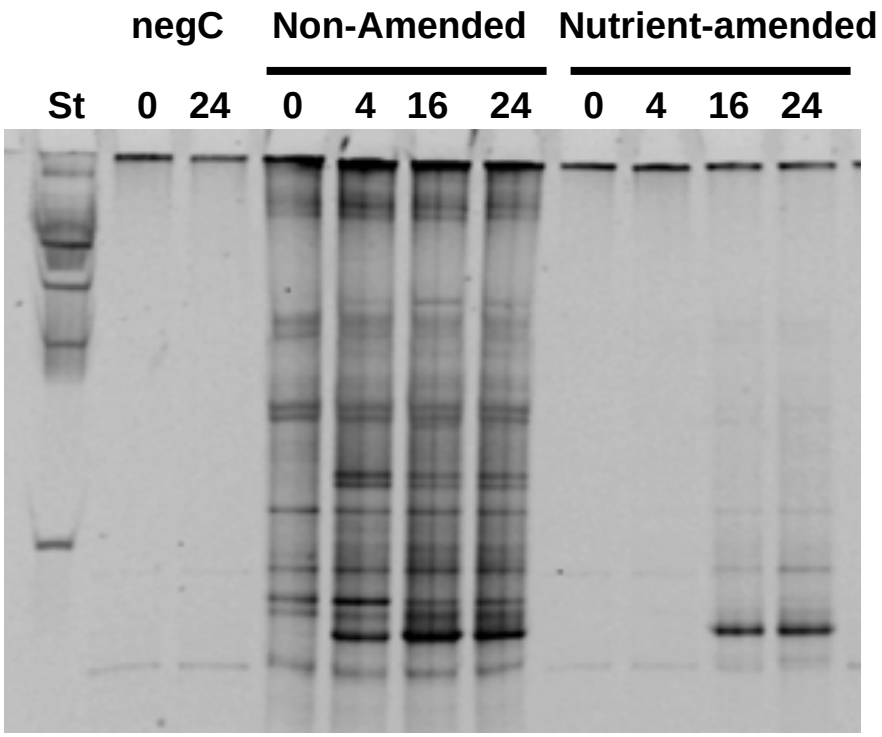

Figure 3.16 Bacterial PCR-DGGE of the water-phase of samples with immobilized oil during biodegradation. Experiment was conducted at -5°C for 24 weeks in seawater-based brines (100 PSU) with or without amendment of inorganic nutrients (Bushnell-Haas formula). Samples were collected from fabrics at week 0, 4, 16 and 24. The negative controls (negC) represent DNA extractions of blank samples at weeks 0 and 24.

3.5 Summaries and conclusions

In this study biodegradation oil petroleum hydrocarbons were investigated in artificial brines at subzero temperatures. The selected conditions were relevant for salinities in brine channels of marine ice at -5 and -10°C. Two commercially available sea salts were added to natural seawater, and element analyses of these artificial brines were compared to natural brines generated by drainage of marine ice. Based on this comparison one of these (Sigma Sea Salt) selected for use in biodegradation studies.

During biodegradation studies water-soluble fractions (WSFs) of oil compounds were generated by careful stirring of a paraffinic oil in seawater. *n*-alkane fractions of the same oil were immobilized to hydrophobic Fluortex adsorbents. Two separate biodegradation studies were performed.

An experiment was conducted with WSFs and immobilized oil in seawater and artificial brines at temperatures of +5, 0, -5 and -10°C. The experiment was performed for a period of 24 weeks, and WSFs examined by GC/MS analyses of total target analytes, C0-C4 naphthalenes, 2-3 ring PAH, and C0-C4 phenols. All compound groups except the phenols showed a rapid depletion, and the depletion was temperature-dependent. However, also sterile controls run at +5 and 0°C also showed depletion, but to lesser extent that in the biotic samples. When WSFs from two different oil:water ratios. 1:1000 and 1:10 000, were compared, depletion was faster for the WSFs with the lowest compound concentrations (oil loading 1:10 000). The phenols showed a temporary increase in concentrations, indicating that metabolic compounds from the biodegradation reactions were detected in this group of compounds by GC/MS analyses. However, phenol concentrations also increased in the sterile controls, indicating that these were not sterile. Thus, it was difficult to predict the contributions of different mechanisms to the depletion, but the results indicated that bacterial degradation took place, also in brines at temperatures at -5 and -10°C. *n*-Alkanes in immobilized oil were analyses by GC-FID, but no *n*-alkane biodegradation was determined, as determined by calculating the ratios between *n*C17/Pristane and *n*C18/Phytane. Microbiology analyses showed temperature-dependent increases in bacterial concentrations. Bacterial concentrations increased also in the brines at -5°C, but not at -10°C. Changes in bacterial communities were investigated by PCR-DGG, and the analyses showed that new bands emerged during the degradation period in the brines.

A second biodegradation study was conducted in artificial brines at -5°C, and with comparison of brines with and without added inorganic nutrients (Bushnell-Haas inorganic medium). The determinations of hydrocarbon groups in WSFs confirmed the results from the first experiment. In the second experiment sterile controls of brines were included and the biocide concentrations increased. However, depletion was recorded in the controls also in these experiments, although to lesser extents than in correspondent biotic samples for most of the WSF compounds. No differences were observed between comparable systems with or without nutrient amendment. In addition, increased oil:water ration resulted in some instances in increased depletion, contrary to the results from BE1. Results for *n*-alkanes in immobilized oil were also in agreement with the results from the

first experiment, and no biodegradation was recorded with or without nutrient amendment.

In conclusion, the experiments indicated that slow biodegradation appeared in brines at subzero temperatures in the water-soluble fraction, but not in the oil phase. One argument for this was the temporary increase in phenol concentrations, previously associated with biodegradation of monoaromatics (Brakstad et al., 1999; Brakstad and Faksness, 2000). However, due to possible biodegradation in the sterile controls, it was not possible to determine the contribution of biodegradation to the depletion of soluble hydrocarbon in the experiments. The potential biodegradation in the brines at sub-zero temperatures were supported by microbiological analyses like epifluorescence microscopy counts and bacterial PCR-DGGE. The results also indicated that no stimulation of biodegradation resulted from the use of a standard inorganic nutrient supply recommended for stimulation of biodegradation in seawater. If bioremediation is to be used in ice it is therefore important to investigate novel systems specially designed for improving biodegradation in sea ice brine.

Further investigations of oil-in-ice biodegradation should be conducted to determine the fate of hydrocarbons in the ice and to include these data as part of the risk assessment of oil in ice. It may also be of interest to investigate the possibilities of treating oil spills in the Arctic with respect to stimulation of oil biodegradation during the arctic winter

4 Modeling

4.1 Introduction

As part of an international effort to describe the fate of water-soluble compounds in sea ice, this section explores the possibility of developing a numerically efficient model of first-year sea ice growth and decay for estimating bounds on wintertime entrainment and summertime release of generic, water-soluble compounds. The model will be applied to the seasonal cycle of un-deformed first-year sea ice.

While the focus of this work is on the development of a column model it should be clear that a single column may not be able to capture average properties of a piece of ice in all detail as even un-deformed landfast sea ice is spatially variable. For example, Figure 4.1 depicts snow dunes on sea ice resulting from the redistribution and packing of snow by wind. Those dunes lead to a spatial variability in heat conduction, transmission of shortwave radiation, and melt progression. The influence on heat conduction is illustrated in the thickness profile transect of Figure 4.1 that shows that deeper snow tend to be associated with thinner ice. Corresponding variability in surface conditions can be observed during the early stages of surface melt (Figure 4.2). If model results are to be compared with field measurements, allowance has to be made for poorly characterized uncertainties in the measurements.

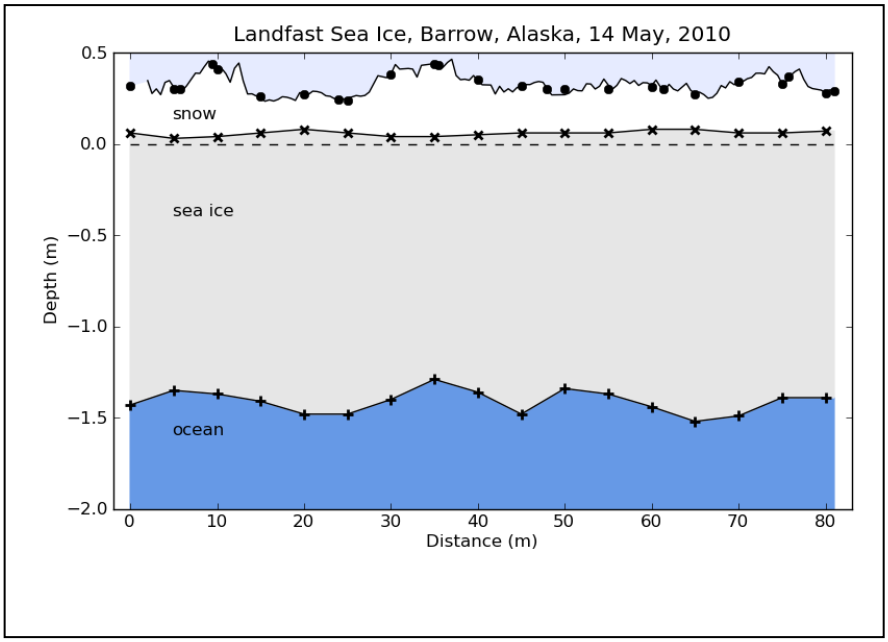

Figure 4.1 Vertical profile along a transect on un-deformed sea ice. Freeboard level is at zero.

Figure 4.2 Early stages of surface melt. Dark veins are from entrained sediment. Barrow, 10 June, 2008.

In what follows, a brief description will be given of pertinent sea ice growth and melt processes. Illustrations in the figures are based on measurement on undeformed landfast first-year sea ice in the Chukchi Sea at Barrow, Alaska. Based on this motivation, the model will be introduced and results will be compared against measurements on landfast sea ice at Barrow, Alaska.

4.1.1 Seasonal evolution, flux, and bulk salinity

In order to motivate the individual components of the model, the processes of brine movement during growth and decay of first-year sea ice will be revisited. The model, in spite of its simplicity, covers the process of desalination involving buoyancy-driven convection during ice growth, and 3 aspects of forced convection due to meltwater flushing.

With the exception of regions of super-cooled water, columnar sea ice forms in response to heat loss from the ocean to the atmosphere (Weeks, 2010). A thin layer of ice crystals forms and congelates at the surface which act as seeds for subsequent columnar ice formation with a characteristic lamellar ice–ocean interface. The bottom layer of sea ice with clearly visible lamellae is called the skeletal layer and is typically between 0.5 and 5 cm thick. The ice crystal lattice of the lamellae themselves is almost devoid of impurities, hence solute is rejected into the surrounding brine, increasing its salinity (Petrich and Eicken, 2010). As the freezing point of brine decreases with increasing salinity, the continuous reduction of the ambient temperature in the skeletal layer due to heat conduction toward the atmosphere results in thickening of the lamellae and further solute enrichment of the brine until the brine is at its freezing point and thermodynamic equilibrium is reached again. Eventually, ice bridges form between the lamellae and a pore space develops of brine pockets interconnected by necks. Since temperature

decreases in the ice with distance from the ice–ocean interface, brine salinity and density increase with distance from the ice–ocean interface. In this hydrostatically unstable configuration, a perturbation in the density field will lead to vertical movement that further exacerbates the perturbation, producing a driving force for brine movement against the friction from the pore space. However, a local mismatch between the freezing point of the perturbation and the surrounding temperature will result in freezing (i.e. enrichment of brine and latent heat release) or melting (i.e. dilution of brine and uptake of latent heat) until equilibrium is reached. The latent heat flux available for this is limited by thermal conduction through the ice, giving rise to a Rayleigh number criterion that relates the magnitude of the driving force to the retarding forces. Naturally driven convection can only occur if the Rayleigh number exceeds a critical value. In growing sea ice, the liquid volume fraction (porosity) and hence the permeability of ice to fluid motion decrease with increasing distance from the ice–ocean interface, confining any significant convection to the bottom 5 to 20 cm. It is often assumed that ice of porosity below approximately 0.05 to 0.07 is essentially impermeable to fluid motion. The fluxes of downward-moving, more saline brine leaving the ice and upward-moving, comparatively less saline seawater have to balance due to mass conservation. As downward-moving, more saline brine dissolves ice in its pathway, it produces chimney-like tubes, termed brine drainage channels. These channels funnel downwelling flow and are of the order of 1 mm wide. Brine streamers emerging from them can readily be observed in the laboratory (Wakatsuchi and Ono, 1983). Channels are separated by a few cm (Wakatsuchi and Saito, 1985), and upwelling takes place predominantly in the interstices between channels (Niedrauer and Martin, 1975. Since the upwelling flow transports less saline seawater into ice otherwise containing solute-enriched brine, a reduction of the bulk sea ice salinity (i.e. the salinity of the melt of a section of sea ice) takes place predominantly between the channels (Cottier et al., 1999). The bulk salinity approximates the seawater salinity at the ice–ocean interface and quickly decreases with increasing distance from the interface, reaching its seasonally stable value between 3 and 10 ppt within centimeters (Figure 4.3). In general, slower-growing ice will reach lower bulk salinity, resulting in a general decrease of the bulk salinity with distance from the ice surface.

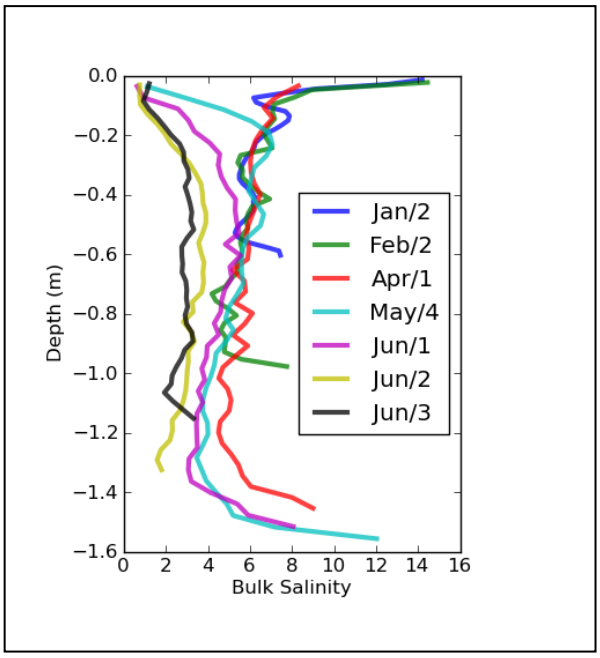

Figure 4.3 Average bulk salinity profiles measured at Barrow, AK in 2008. The time of the profiles is given as "Month / week of the month". Profiles of June have experienced surface ablation.

A reversal of flow direction in a channel leads to the influx of seawater and subsequent enhanced ice formation that can lead to neck formation inside the channel and at the bottom. Similarly, stagnation of flow in a channel will lead to necking at the bottom. If channels are wide enough (approximately 2 mm in diameter), they are able to support counter-flow, i.e. simultaneous upward and downward movement inside the same channel (Lake and Lewis, 1970). The counter-flow inside individual brine channels is irrelevant for bulk desalination due to the small volume the channels occupy. However, it may substantially increase the availability of nutrients to biota inside the channel. The flux of seawater though skeletal layer, pore space, and brine channels is significant and sufficient to resupply nutrients to an ecosystem revolving around ice microalgae (Reeburgh, 1984). The solute-enriched flux leaving the ice contributes to both mixing of the surface layers and the production of deep water in certain parts of the world.

In contrast to buoyancy-driven, natural convection in winter and early spring, the brine flux in late spring and summer is dominated by forced convection from brine above the freeboard level and surface meltwater. As air temperature rises in spring and solar radiation becomes significant, the ice warms and becomes more porous. The ice temperature, instead of being lowest at the ice surface, is now lowest in the ice interior as a result of the heat capacity of sea ice (Figure 4.4).

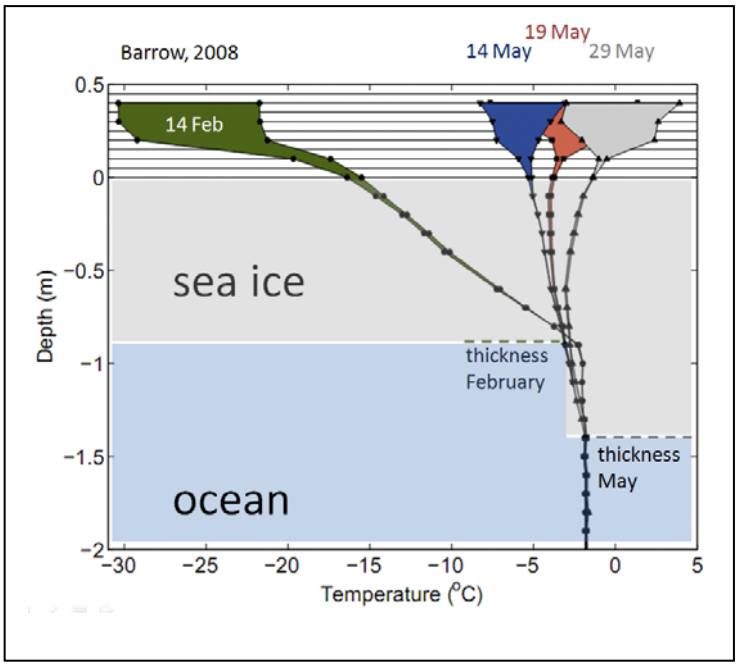

Figure 4.4 Daily temperature range measured in ocean, sea ice, snow, and atmosphere (the latter two are hatched). Snow–ice interface is at 0.

In practice, observing more than one local extremum in the temperature–depth relationship of sea ice is exceedingly rare. At the same time, snow starts to melt, producing meltwater and a latent heat flux to the surface. With increased permeability, finite freeboard, and an additional pressure head from pooled water, meltwater is forced downward through the ice, diverging horizontally as the vertical permeability decreases with distance from the surface to drain through re-opened brine channels. This pathway of successively decreasing vertical, salinity-reducing flux, gives rise to a characteristic, linear bulk salinity profile that is commonly observed in the upper 20 to 50 cm of the ice during melt (Figure 4.3 and Figure 4.5). This profile may develop under a snow cover and before meltponds form. In particular in the presence of a low-salinity, low-porosity surface layer, desalination may be helped from lateral flow of water underneath the low-permeability surface layer. Throughout the melt period, brine channels experience a flow of warm brine that allows them to widen and serve as preferred pathway for drainage. The pore space that develops during the melt season is referred to as secondary pore space, in contrast to the primary pore space that developed during growth.

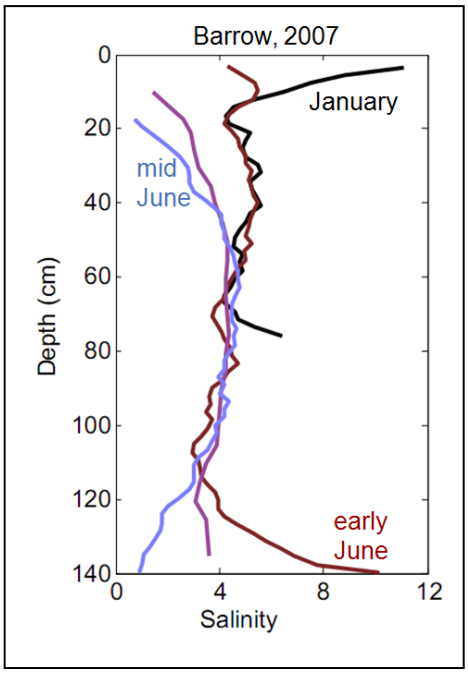

Figure 4.5 Selected bulk salinity profiles from Barrow, AK in 2007. Profiles are corrected for estimated surface ablation based on sediment layer position.

Following the development of the linear bulk salinity profile near the ice surface and upon further warming of the ice, the permeability of the coldest layers will become high enough to support some downward flushing of meltwater, resulting in a gradual decrease of the salinity throughout the ice (Figure 4.3).

At the same time, brine channels act as supply of less saline brine to the ice between the coldest part of the ice and the ice–ocean interface. In this region, desalination is observed that results in a linear bulk salinity profile with the lowest values near the ice bottom (Figure 4.5). It is hypothesized that meltwater moving down the brine channels acts as freshwater source to rinse the pore space. Since the permeability increases with proximity to the ice–ocean interface, so does the flux from the channel into the bulk pore space, resulting in the lowest bulk salinity near the ice–ocean interface.

After the drainage of surface meltwater to the freeboard level, surface and bottom ablation of the ice continue and the bulk salinity decreases predominantly in the upper and middle sections of the ice. This is presumably due to warming of the once coldest ice interior to ambient temperatures, diluting brine noticeably. Salinities near the ice–ocean interface are now highest again since the very low-salinity bottom-most ice melted off (Figure 4.3).

4.1.2 Model Requirements

In order to simulate the brine flux within sea ice, the following key processes have to be included:

- winter/growth:
  - natural convection within the bottom 1 to 10 cm due to unstable brine density stratification, with brine moving upward through the pore space and generally downward through primary drainage channels
- spring/melt:
  - flushing near the upper surface due to increased permeability and lateral percolation of brine from the pore space into secondary drainage channels and flaws
  - flushing near the bottom due to increased permeability and infiltration of the pore space with surface meltwater arriving through secondary drainage channels
  - flushing of the center of the ice due to increased permeability and vertical percolation of brine through the pore space

Hence, the model will have to

- describe the processes of both natural convection and forced convection (flushing),
- discriminate between secondary pore space spanning the entire thickness of the ice on the one hand, and pore space comprised of more-or-less interconnected pores and necks, including primary drainage channels a few centimeters in length near the ice–ocean interface on the other hand, and
- predict the seasonal evolution of the pore space.

In addition, the model should be numerically efficient.

4.2 Methods

4.2.1 Governing Equations

4.2.1.1 Representative Elementary Volume (REV)

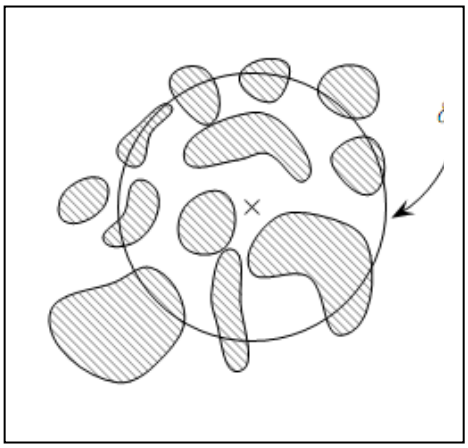

Figure 4.6 Cartoon of a porous medium with hatched areas representing the solid matrix. Microscopic structure and dynamics within the volume δV are assumed to be adequately described by their respective local averages.

Pores and channels within sea ice have been described over six orders of magnitude, from the scale of micrometers to meters (e.g. Perovich and Gow, 1996; Light et al., 2003; Cole et al. 2004). Describing the fluid flow through this network at the pore scale, while possible in principle, is not practical. On the one hand, fluid flow through pores at the micrometer range would need to be described over the ice thickness of approximately one meter. This is challenging not only from the point of view of structural, spatial detail that has to be managed efficiently in computer memory, but also from the point of temporal granularity of the numerical solution. The numerical time step has an upper bound at the order of spatial granularity divided by fluid velocity (Courant limit). Hence, fluid velocities within individual pores of around 10^{-4} to 10^{-6} m/s impose an upper limit of the time step of 0.01 to 1 s at a spatial scale of 10^{-6} m. This is an upper limit, and the maximal time step will be less than 10 % of this time step in practice. Hence, for 1 m of ice to grow in approximately 100 days, a total of 100 x 10^6 time steps would have to be computed, leading to computational times (i.e. wall times) that exceed weeks or even months. The most common alternative to calculating fluid dynamics at the pore level is the volume-averaged, representative elementary volume (REV) approach (Bear and Bachmat, 1990). The assumption underlying this approach is that both pore space (including porosity and permeability) and state variables (velocity, temperature, salinity, pressure) at each point within the porous medium can be described by their respective local volume-averages. This assumption usually applies if the macroscopic properties vary continuously, and if there is not dead pore space (i.e. disconnected pores). It is therefore possible to define a volume δV at that the porous medium is homogeneous (Figure 4.6). From all we know about sea ice, this may impose a lower limit on the spatial scale of the order of tens of micrometers within the ice. By implication, a REV is unable to accurately represent a discrete interface.

4.2.1.2 Dual Porosity, Dual Permeability Approach

The dual porosity, dual permeability approach is applied to porous media that comprise of a pore volume that can be separated into two distinctly different groups. Typically, one pore space is considered to be a network of pores and necks as described above, while the other pore space is considered to be a network of interconnected fractures or channels. Both pore spaces are considered to span the entire domain of the medium, yet they are independent and differ in porosity, permeability, pressure and fluid velocity (and possibly tracer concentration, temperature etc.). Interaction between the pore spaces takes place through transfer coefficients. In the present case, the main interaction is fluid exchange in response to local pressure differentials between the pore spaces. Computationally, the treatment of a second pore space is straight-forward as it simply increases the dimension of the simulation by one. For example, if a single-porosity 1-dimensional (1D) column model (representing the pores and necks in sea ice, for example) is to be extended by a second 1D column of a different pore structure (representing brine channels, for example), then this could be accomplished by performing a 2D, two-column simulation with a suitable description of transfers. Transfer of liquid volume could be achieved by means of a "transfer permeability" and heat by means of a "transfer thermal diffusion coefficient". Further, the columns may assume different permeability descriptions (for example, the permeability of the fractured medium may be higher for a given porosity) in order to account for the difference between the geometry of pores and fractures.

4.2.1.3 Governing Equations

Underlying all approximations are the following conservation equations for heat, solute (or tracers), momentum, and mass. They are the Navier-Stokes equations with Boussinesq approximation in volume-averaged form, consistent with the REV approach. Following the presentation of the dual porosity approach above as a two-column model, the governing equations are given for a system in two dimensions. Note that hence the vertical permeability, Π_z, is a function of x. The equations are valid within both a porous medium (porosity $0<\phi<1$) and a liquid ($\phi=1$).

The governing equations are expressed in terms of local, intrinsic volume averages of temperature, T, solute concentration in the liquid, C, and horizontal and vertical superficial fluid velocity components ϕu and ϕw, respectively. The volume averaging method has been used to derive the governing equations (Ganesan and Poirier, 1990; Bear and Bachmat, 1990). All physical properties of liquid and solid, for example density and heat capacity, are assumed to be constant locally, i.e. within the averaging volume δV.

The volume-averaged mass conservation equation is

$$\left[1-\frac{\rho_i}{\rho_w}\right]\frac{\partial\phi}{\partial t}+\frac{\partial(\phi u)}{\partial x}+\frac{\partial(\phi w)}{\partial z}=0\,, \quad (2.1)$$

where u and w are the interstitial fluid velocity components in the x and z directions, respectively, ϕ is the total porosity (volume fraction of liquid), and $\rho_w = 1000$ kgm^{-3} and $\rho_i = 918$ kgm^{-3} are the constant densities of water and ice, respectively, that characterize the volume change during mass transfer between liquid and solid.

The volume-averaged momentum conservation equations are

$$\rho_w\left[\frac{\partial(\phi u)}{\partial t}+\frac{\partial(\phi uu)}{\partial x}+\frac{\partial(\phi uw)}{\partial z}\right]=\mu\left[\frac{\partial^2(\phi u)}{\partial x^2}+\frac{\partial^2(\phi u)}{\partial z^2}\right]-\phi\frac{\partial p}{\partial x}-\phi\frac{\mu}{\Pi_x}\phi u\,, \quad (2.2)$$

$$\rho_w\left[\frac{\partial(\phi w)}{\partial t}+\frac{\partial(\phi wu)}{\partial x}+\frac{\partial(\phi ww)}{\partial z}\right]=\mu\left[\frac{\partial^2(\phi w)}{\partial x^2}+\frac{\partial^2(\phi w)}{\partial z^2}\right]-\phi\frac{\partial p}{\partial z}+\phi\rho g-\phi\frac{\mu}{\Pi_z}\phi w\,, \quad (2.3)$$

where ρ is the variable density of the liquid in the buoyancy term (third term on the right hand side of (2.3)), which is a function of brine salinity and temperature (Fofono and Millard, 1983), $\mu = 1.8\times10^{-3}$ kgms^{-1} is the dynamic viscosity, p the pressure, Π_x and Π_z are the diagonal components of the permeability tensor of the porous medium (i.e. lateral and vertical permeability, respectively) and depend on porosity ϕ, and $g = -9.8$ ms^{-2} is the acceleration due to gravity.

The volume–averaged form of the energy balance equation is

$$\overline{\rho c}\frac{\partial T}{\partial t}+\rho_w c_w\left[\frac{\partial(T\phi u)}{\partial x}+\frac{\partial(T\phi w)}{\partial z}\right]=\frac{\partial}{\partial x}\left[\bar{k}\frac{\partial T}{\partial x}\right]+\frac{\partial}{\partial z}\left[\bar{k}\frac{\partial T}{\partial z}\right]+\left|\frac{\partial F_{SW}}{\partial z}\right|-\left[T\Delta(\rho c)+L\rho_i\right]\frac{\partial\phi}{\partial t}\,, \quad (2.4)$$

where T is the temperature of solid and liquid, $L = 334\times10^3$ J kg^{-1} is the latent heat of fusion of ice at $T = 0°$ C, $|\partial F_{SW}/\partial z|$ is the absorbed shortwave radiation, and the average quantities in the porous medium are defined as

$$\overline{\rho c}=\phi\rho_w c_w+(1-\phi)\rho_i c_i\,, \quad (2.5)$$

$$\Delta(\rho c)=\rho_w c_w-\rho_i c_i\,, \quad (2.6)$$

$$\bar{k}=\phi k_w+(1-\phi)k_i\,, \quad (2.7)$$

with the specific heat capacities $c_w = 4.2$ kJ kg^{-1}K^{-1} and $c_i = 2.0$ kJ kg^{-1}K^{-1}, and heat conductivities $k_w = 0.56$ Wm^{-1}K^{-1} and $k_i = 2.1$ Wm^{-1}K^{-1} of water and ice, respectively. Note that both c_i and L are properties of pure ice rather than bulk thermal properties of sea ice. Sea ice thermal properties implicitly include changes of latent heat during phase

transition in response to temperature change. However, this is explicitly included in the energy conservation equation through the term $\partial\phi/\partial t$.
The volume–averaged solute (conservation equation is

$$\phi\frac{\partial C}{\partial t}+\frac{\partial\left(C\phi u\right)}{\partial x}+\frac{\partial\left(C\phi w\right)}{\partial z}=\frac{\partial}{\partial x}\left[\phi D\frac{\partial C}{\partial x}\right]+\frac{\partial}{\partial z}\left[\phi D\frac{\partial C}{\partial z}\right]-C\frac{\partial\phi}{\partial t}, \qquad (2.8)$$

with the concentration C of solute in the liquid, and the solute diffusion coefficient $D = 7\times10^{-10}$ m^{2}s^{-1}.

Phase transitions are governed by local thermodynamic equilibrium, i.e. in any volume δV, the temperature T strives to be equal to the freezing point T_F of the brine of concentration C. With consideration given to latent heat release and solute partitioning at the microscopic interface, this constitutes a condition for the change of local liquid volume fraction $\Delta\phi$ required to establish thermodynamic equilibrium. Hence, $\partial\phi/\partial t = \Delta\phi/\Delta t$, where Δt is the computational time step. The phase transition is estimated by considering a location within the domain as adiabatically enclosed and translating the temperature difference between current temperature T and the freezing point T_F of a solution with concentration C into an equivalent latent heat and thereby porosity change. At the same time, account is taken for solute conservation, i.e. changing solute concentration during phase transition. Hence,

$$\Delta\phi=\left(T-T_F\right)\left[\frac{T\Delta\left(\rho c\right)+\rho_s L}{\overline{\rho c}}-\frac{C}{\phi}\left(\frac{\partial T_F}{\partial C}\right)_{\text{at } C}\right]^{-1}. \qquad (2.9)$$

Other estimates are conceivable. Ultimately, the actual porosity change is found by iteratively solving the governing equations and successively adjusting the phase transition estimate. In addition to the processes included in the equation above, the iterative procedure takes account for heat and solute advection, thermal and solute diffusion, and absorption of shortwave radiation during time step Δt.

4.2.1.4 Parameters for Snow

In the snow layer, the following thermal properties are used: k_{snow} = 0.3 Wm^{-1}K^{-1}, ρc =0.3 $\rho_i c_i$. Only energy conservation is considered with $\partial\phi/\partial t$ =0. The treatment of surface ablation is presented below. Fluid movement and solute conservation are not calculated for snow layers.

4.2.1.5 Common Simplifications

The following models share certain simplifications of the governing equations. In particular, the following terms are neglected: volume expansion during freezing (in mass conservation equation); inertia (i.e. advection of momentum), shear (i.e. dispersion of momentum); advection of heat; diffusion of solute. Further, the freezing temperature is described as

$T_F = m\ C$,

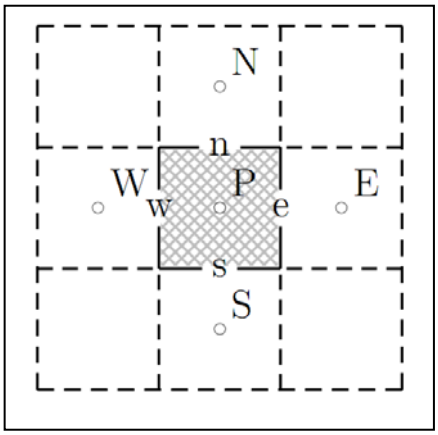

Figure 4.7 Illustration of the compass notation to refer to cells and interfaces adjacent to cell *P*.

where m=-0.054 Km^3kg^{-1} is the slope of the liquidus. In sea ice, this is appropriate only for temperatures above the precipitation of mirabilite ($NaSO_4 \cdot 10H_2O$), i.e. above approx. –8.2º C. Given that brine is in thermodynamic equilibrium, the brine density is primarily a function of solute concentration and calculated from

$\rho = \rho_0 + \beta\ C$,

where ρ_0 is the density at C=0, and β=0.8.

4.2.1.6 Discretization

The volume-integrated governing differential equations are spatially discretized on a grid and solved at discrete times. As a result of the simplifications stated above, the mass and momentum conservation equations can be combined to yield a Laplace equation (i.e. diffusion equation) for the pressure field, which will be solved for implicitly. Based on the pressure field, the volume flux can then be calculated from the momentum equation explicitly. The conservation equation of solute and other tracers is a purely advective equation and yields an explicit solution based on the volume flux. The energy conservation equation reduces to a diffusion equation that has to be solved implicitly. The equations are coupled tightly as they depend on knowledge of both porosity (momentum, solute, energy conservation) and the rate of change in porosity (solute, energy conservation). At the same time, solute advection in the presence of heat diffusion will lead to local thermodynamic disequilibrium that feeds back into porosity and the rate of change thereof. In practice, to obtain a converged solution during any given time step, the rate of change of porosity has to be found iteratively, i.e. by repeatedly solving all governing equations above. It was found in this study that this may require the update of the rate of phase change and the solution of the implicit equations for heat of the order of 12 times during each time step. In the following, we use the compass notation of Patankar (1980) to refer to a cell *P*, its vertical neighbors *N* and *S*, and horizontal neighbors *E* and

W (Figure 4.7). Further, the respective faces of P are denoted as *n*, *s*, *e*, and *w*, respectively.

The momentum conservation equations are reduced to their most dominant term inside a porous medium, which happens to be Darcy's law,

$$\phi u = -\frac{\Pi_x}{\mu}\frac{\partial p}{\partial x} \text{ and}$$

$$\phi w = -\frac{\Pi_z}{\mu}\left(\frac{\partial p}{\partial z} - \rho g\right).$$

Calculation of the derivative with respect to *x* and *z*, respectively, and substitution into the mass conservation equation yields

$$\frac{\partial}{\partial x}\left[\frac{\Pi_x}{\mu}\frac{\partial p}{\partial x}\right] + \frac{\partial}{\partial z}\left[\frac{\Pi_z}{\mu}\left(\frac{\partial p}{\partial z} - \rho g\right)\right] = 0,$$

i.e. a second-order differential equation in *p*. Evaluating the pressure gradient at the faces of each cell *P*, we find

$$-\frac{1}{\Delta x}\left[\left(\frac{\Pi_x}{\mu}\right)_e \frac{p_E - p_P}{(\Delta x)_e} - \left(\frac{\Pi_x}{\mu}\right)_w \frac{p_P - p_w}{(\Delta x)_w}\right]$$
$$-\frac{1}{\Delta z}\left[\left(\frac{\Pi_z}{\mu}\right)_n \frac{p_N - p_P}{(\Delta z)_n} - \left(\frac{\Pi_z}{\mu}\right)_s \frac{p_P - p_s}{(\Delta z)_s}\right] = -\frac{1}{\Delta z}\left[\left(\frac{\Pi_z}{\mu}\right)_n (\rho g)_n - \left(\frac{\Pi_z}{\mu}\right)_s (\rho g)_s\right].$$

Here, Δx and Δz are the dimension of cell *P*, while $(\Delta x)_e$ is the distance between cell centers *P* and *E* etc. Note that permeability and density will have to be evaluated at the cell interfaces rather than the cell center. Face conductivities (in this case permeability) are usually the distance-weighted harmonic means of the conductivities at the respective cell centers, i.e. the algebraic mean resistivity is calculated between cell centers (Patankar, 1980). Defining transfer coefficients

$$a_E = -\left(\frac{\Pi_x}{\mu}\right)_e \frac{1}{\Delta x\,(\Delta x)_e}, \quad a_W = -\left(\frac{\Pi_x}{\mu}\right)_w \frac{1}{\Delta x\,(\Delta x)_w},$$

$$a_N = -\left(\frac{\Pi_z}{\mu}\right)_n \frac{1}{\Delta z\,(\Delta z)_n}, \quad a_S = -\left(\frac{\Pi_z}{\mu}\right)_s \frac{1}{\Delta z\,(\Delta z)_s},$$

$$a_P = -\left(a_N + a_S + a_E + a_W\right),$$

and source term

$$b = -\frac{1}{\Delta z}\left[\left(\frac{\Pi_z}{\mu}\right)_n (\rho g)_n - \left(\frac{\Pi_z}{\mu}\right)_s (\rho g)_s\right],$$

we will have to solve for a system of equations based on
$a_P p_P + a_N p_N + a_S p_S + a_E p_E + a_W p_W = b$
with coefficients determined for each cell P.

Once the pressure field is known, we can calculate the fluxes at the cell interfaces from

$$(\phi u)_e = -\left(\frac{\Pi_x}{\mu}\right)_e \frac{p_E - p_P}{(\Delta x)_e}, \qquad (\phi u)_w = -\left(\frac{\Pi_x}{\mu}\right)_w \frac{p_P - p_W}{(\Delta x)_w},$$

$$(\phi w)_n = -\left(\frac{\Pi_z}{\mu}\right)_n \left[\frac{p_N - p_P}{(\Delta z)_n} - (\rho g)_n\right], \; (\phi w)_s = -\left(\frac{\Pi_z}{\mu}\right)_s \left[\frac{p_P - p_S}{(\Delta z)_s} - (\rho g)_s\right],$$

where care has to be taken to use the same values for permeability and density as during the calculation of the transfer coefficients a and source term b above. Note that it is advantageous from the point of view of numerical precision to perform the calculations of the velocity field assuming a reduced density

$\rho \leftarrow \rho - \rho_{ref}$,

where ρ_{ref} is an arbitrarily chosen density of the same order of magnitude as the average density of the system.

The simplified solute conservation equation is

$$\phi \frac{\partial C}{\partial t} + \frac{\partial (C \phi u)}{\partial x} + \frac{\partial (C \phi w)}{\partial z} = -C \frac{\partial \phi}{\partial t}$$

and is discretized as

$$\frac{C_P^t - C_P^{t-1}}{\Delta t} + \frac{C_e^* (\phi u)_e - C_w^* (\phi u)_w}{\phi^* \Delta x} + \frac{C_n^* (\phi w)_n - C_s^* (\phi w)_s}{\phi^* \Delta z} = -\frac{C_P^*}{\phi^*} \frac{\partial \phi}{\partial t},$$

which is explicitly solved for C_P at time step t. The bounded first-order upwind scheme is used to determine the concentrations C at the interfaces (Patankar, 1980): if the flux is directed out of cell P then the respective interface concentration is C_P. However, if the flux is directed into cell P, then the interface concentration is the concentration of the respective neighboring cell. The starred concentration and porosity values are the current best estimates of concentration and porosity, which could the values at time step t-1.

The simplified energy conservation equation is

$$\overline{\rho c}\frac{\partial T}{\partial t} = \frac{\partial}{\partial x}\left[\overline{k}\frac{\partial T}{\partial x}\right] + \frac{\partial}{\partial z}\left[\overline{k}\frac{\partial T}{\partial z}\right] + \left|\frac{\partial F_{SW}}{\partial z}\right| - \left[T\Delta(\rho c) + L\rho_i\right]\frac{\partial \phi}{\partial t},$$

which will be solved implicitly and is discretized similarly to the equation for pressure as

$$\overline{\rho c}\frac{T_P - T_P^{t-1}}{\Delta t} = \frac{1}{\Delta x}\left[\overline{k_e}\frac{T_E - T_P}{(\Delta x)_e} - \overline{k_w}\frac{T_P - T_W}{(\Delta x)_w}\right] + \frac{1}{\Delta z}\left[\overline{k_n}\frac{T_N - T_P}{(\Delta z)_n} - \overline{k_s}\frac{T_P - T_S}{(\Delta z)_s}\right] + \left|\frac{\partial F_{SW}}{\partial z}\right| - \left[T_P^{t-1}\Delta(\rho c) + L\rho_i\right]\frac{\partial \phi}{\partial t}.$$

Hence, after collecting terms,

$$a_E = -\frac{\overline{k_e}}{\Delta x\,(\Delta x)_e}, \quad a_W = -\frac{\overline{k_w}}{\Delta x\,(\Delta x)_w},$$

$$a_N = -\frac{\overline{k_n}}{\Delta z\,(\Delta z)_n}, \quad a_S = -\frac{\overline{k_s}}{\Delta z\,(\Delta z)_s},$$

$$a_P = -(a_N + a_S + a_E + a_W) + \frac{\overline{\rho c}}{\Delta t},$$

$$b = \left|\frac{\partial F_{SW}}{\partial z}\right| - \left[T^{t-1}\Delta(\rho c) + L\rho_i\right]\frac{\partial \phi}{\partial t} + \overline{\rho c}\frac{T^{t-1}}{\Delta t},$$

resulting in a linear system of equations based on

$a_P\,T_P + a_N\,T_N + a_S\,T_S + a_E\,T_E + a_W\,T_W = b$

for each cell P.

4.2.1.6.1 Boundary Conditions

Matrix coefficients a and vector b require special treatment at the boundaries, depending on the boundary conditions.

4.2.1.6.2 Temperature Boundary Conditions

Since the domain is laterally mirror symmetric, the lateral temperature boundaries are adiabatic, i.e. the lateral conductive flux is $F_c = -k\,\partial T/\partial x = 0$ (note that in the following, F_c is expressed with respect to the x-direction rather than in direction towards or away from any particular interface). The bottom boundary has a temperature fixed at T_b (usually the freezing point), and the top boundary is defined by both a temperature T_t (i.e. air temperature) and a thermal resistance R (i.e. the reciprocal of the heat transfer coefficient.

Note that R may be 0 if the surface temperature is to be specified). The transfer coefficients are thus modified as follows:

- East: with $F_c = 0$, $a_P \leftarrow a_P + a_E$, $b \leftarrow b - \frac{F_c}{\Delta x}$, $a_E \leftarrow 0$.

- West: with $F_c = 0$, $a_P \leftarrow a_P + a_W$, $b \leftarrow b + \frac{F_c}{\Delta x}$, $a_W \leftarrow 0$.

- North: with $\tilde{k} = \frac{\Delta z}{\frac{0.5\,\Delta z}{\bar{k}} + R}$, $a_P \leftarrow a_P + a_N + \frac{\tilde{k}}{(\Delta z)^2}$, $b \leftarrow b + \frac{\tilde{k}\,T_t}{(\Delta z)^2}$, $a_N \leftarrow 0$.

- South: $a_P \leftarrow a_P + a_S + \frac{\bar{k}}{0.5\,(\Delta z)^2}$, $b \leftarrow b + \frac{\bar{k}\,T_b}{0.5\,(\Delta z)^2}$, $a_S \leftarrow 0$.

4.2.1.6.3 Pressure / Velocity Boundary Conditions

Since the domain is mirror symmetric laterally, the lateral pressure gradient at the boundary is 0 (and hence, u=0). A pressure is defined at the bottom of the domain, p_b, and the top of the domain has either a pressure defined (p_t) or a zero-velocity surface boundary (i.e. zero pressure gradient). Implicit in the implementation of the temperature boundary conditions is that the temperature profile between boundary cell and interface is linear, i.e. the boundary heat flux is proportional to the temperature difference between boundary cell and boundary cell interface. However, a linear vertical temperature profile will lead to a linear brine salinity and density profile and hence to a quadratic pressure profile. Thus, the matrix coefficients are adjusted such that correct solutions are found for up to second-order pressure profiles. It should be clarified here that the pressure at a cell P is the integral $p=\int \rho\, g\, \mathrm{d}z$ calculated from 0 to the *center* of any given cell P.

- East: with $\phi u = 0$, $a_P \leftarrow a_P + a_E$, $b \leftarrow b - \frac{\phi u}{\Delta x}$, $a_E \leftarrow 0$.

  However, if the pressure is prescribed in cell E rather than the flux at the e boundary:

  with $p_E = p_E^{bnd}$, $a_P \leftarrow a_P$, $b \leftarrow b - a_E\, p_E^{bnd}$, $a_E \leftarrow 0$.

- West: with $\phi u = 0$, $a_P \leftarrow a_P + a_W$, $b \leftarrow b + \frac{\phi u}{\Delta x}$, $a_W \leftarrow 0$.

- North: $a_P \leftarrow a_P + a_N + \frac{3}{(\Delta z)^2}\left(\frac{\Pi_z}{\mu}\right)_n$, $b \leftarrow b + \frac{8}{3(\Delta z)^2}\left(\frac{\Pi_z}{\mu}\right)_n p_t$,

  $a_S \leftarrow a_S - \frac{1}{3(\Delta z)^2}\left(\frac{\Pi_z}{\mu}\right)_n$, $a_N \leftarrow 0$.

  This is valid only if cells P and S at the boundary are of equal size Δz.

- South: $a_P \leftarrow a_P + a_S + \frac{3}{(\Delta z)^2}\left(\frac{\Pi_z}{\mu}\right)_s$, $b \leftarrow b + \frac{8}{3(\Delta z)^2}\left(\frac{\Pi_z}{\mu}\right)_s p_b$,

  $a_N \leftarrow a_N - \frac{1}{3(\Delta z)^2}\left(\frac{\Pi_z}{\mu}\right)_s$, $a_S \leftarrow 0$.

  This is valid only if cells P and N at the boundary are of equal size Δz.

The vertical pressure boundary conditions assume that the pressure profile is parabolic from the boundary past the center of the boundary cell and to the center of the next adjacent cell. Since the vertical flux depends on the pressure gradient at the interface, the pressure gradient has to be calculated consistent with this assumption. Therefore, the vertical fluxes at the respective domain interfaces are calculated as follows:

$$(\phi w)_n = -\left(\frac{\Pi_z}{\mu}\right)_n \left[\frac{8p_t - 9p_P + p_S}{3\Delta z} - (\rho g)_n\right], \text{ and}$$

$$(\phi w)_s = -\left(\frac{\Pi_z}{\mu}\right)_s \left[\frac{-8p_b + 9p_P - p_N}{3\Delta z} - (\rho g)_s\right].$$

Note that the weights (+8,-9,+1) apply only if the two cells closest to the boundary (i.e. *P* and *S*, or *P* and *N*, respectively) have the same size Δz.

4.2.1.6.4 Time Step

The maximum computational time step is determined by the Courant limit,

$$\Delta t < \frac{\Delta z}{|w|}, \frac{\Delta x}{|u|}$$

since, exceeding this limit, would cause brine to be advected over distances larger than a cell size in a single time step. Failing to observe this criterion tends to lead to excessive flow velocities. In practice, the maximum time step should not exceed 10% of the ratio ofdomain size and maximum intersticial fluid speed $|u|$ and $|w|$.

4.2.1.7 Coupling of Equations

In a model that fully couples the governing equations, the procedure is during each time step:

1. Precipitate snow
2. Calculate absorbed solar energy for each cell in the domain
3. Guess that all fields at current time step *t* will be the same as during the previous time step *t-1*.
4. Outer loop:
   - 4.1. Calculate the mass flux at time *t* based on the current best guess of the porosity field
   - 4.2. Check Courant number criterion: if flux is too high, reduce time step and continue at 2.1.
   - 4.3. Guess that phase change during time step *t* will be 0.
   - 4.4. Inner loop:
     - 4.4.1. Calculate solute advection
     - 4.4.2. Adjust estimate of phase change based on current thermodynamic disequilibrium
     - 4.4.3. Calculate heat diffusion
     - 4.4.4. Update best estimate of porosity field based on porosity at *t-1* and current assumption of phase change
5. Calculate and apply ice growth, and ice and snow ablation

Typically, the temperature field is converged after the inner loop has been executed a total of 12 times (i.e. for example, the inner loop is run 4 times and the outer loop is run 3 times).

While energy conservation is calculated for the snow–sea ice system, pressure and mass flux are calculated only for sea ice.

4.2.2 Irradiance

4.2.2.1 Down-welling Solar Radiation

In the absence of measurements, the down-welling irradiance is calculated from the elevation angle of the sun, optical thickness of the atmosphere, reflection at the upper side of the cloud layer, and multiple reflection between the cloud underside and the ground. Given the cloud albedo α_c=0.9, the cloud cover fraction c=0.6, and the ground albedo α_g=0.8, the down-welling shortwave radiation is

$$F_{\downarrow}^{SW} = F_{\downarrow}^{CS} \frac{1 - c\alpha_c}{1 - c\alpha_c \alpha_g}$$

where the clear sky radiation

$$F_{\downarrow}^{CS} = I_0\, e\, \exp(-c_o\, m_o)\, \sin\theta$$

depends on the solar constant I_0=1366 W/m^2, excentricity e, atmospheric absorption coefficient c_o=0.15 of a clear atmosphere, optical mass of the atmosphere m_o, and solar elevation angle θ. The excentricity is calculated from

$$e = \left[1 + 0.33412\, \cos\left(2\pi \frac{d-3}{365}\right)\right]^{-1},$$

where d is the day of the year (1 Jan being d=1). The optical mass is
$m_o = \left[\sin\theta + 0.025\, \exp(-11 \sin\theta)\right]$.

The solar elevation angle is calculated from
$\sin\theta = \cos h \cos\delta \cos\Phi + \sin\delta \sin\Phi$,

where Φ is the present latitude, δ is the declination angle

$$\delta = -\frac{\pi}{180} 23.44\, \cos\left(2\pi \frac{d+10}{365}\right),$$

and h is the hour angle,

$$h = \pi \frac{H-12}{12},$$

with local solar time H (solar noon being H=12).

4.2.2.2 Absorption in Snow and Ice

Radiative absorption in snow and ice follows an exponential decay but does account neither for spectral absorption characteristics nor for the optical properties of a scattering layer near the ice surface. Instead, optical properties are prescribed as follows: bulk extinction coefficients in snow and sea ice are κ_e=200 m^{-1} and κ_e=0.5 m^{-1}, respectively. The surface albedo α of snow covered ice, bare ice and ponded ice is 0.85, 0.65, and 0.3, respectively.

With irradiance absorbed in snow, ice or water

$$F_{\downarrow} = (1-\alpha) F_{\downarrow}^{SW},$$

absorption in snow at a distance from z to $z+\Delta z$ from the snow surface is

$$\frac{\partial F^{SW}}{\partial z} = -F_{\downarrow} \frac{\kappa_e^{snow}}{\Delta z}\left[\exp\left(-\kappa_e^{snow} z\right) - \exp\left(-\kappa_e^{snow}(z+\Delta z)\right)\right].$$

Absorption in ice at a distance from z to $z+\Delta z$ from the ice surface is

$$\frac{\partial F^{SW}}{\partial z} = -F_{\downarrow}^{ice-surface} \frac{\kappa_e^{ice}}{\Delta z}\left[\exp\left(-\kappa_e^{ice} z\right) - \exp\left(-\kappa_e^{ice}(z+\Delta z)\right)\right],$$

Where

$$F_{\downarrow}^{ice-surface} = F_{\downarrow} \exp\left(-\kappa_e^{snow}\ h_s\right),$$

and h_s is the snow depth.

Justification for using an exponential: (NB: *The notation for the extinction coefficient differs in this paragraph: the extinction coefficient is κ rather than κ_e, and κ_a and κ_s are absorption and scattering coefficient, respectively* .) Assuming a rate of absorption proportional to the exponential of depth is appropriate even from the point of view of a two-stream scattering model – apart from the bottom quarter of an optically thick slab, where absorption is overestimated (however, the magnitude of absorption is so low that we won't have to be concerned here). Following the general notation of Petrich and Eicken (2010), the rate of extinction is

$$\frac{\partial F^{SW}}{\partial z} = \frac{\partial (I_{\downarrow} - I_{\uparrow})}{\partial z} = -F_{\downarrow}^{SW}\ (1-\alpha_{\infty})\ \kappa \exp(-\kappa z)\ \frac{1 - \frac{r}{\alpha_{\infty}} \exp\left(-2\kappa\left[z_0 - z\right]\right)}{1 - r\ \exp\left(-2\kappa\ z_0\right)},$$

where z_0 is the slab thickness, z is the distance from the slab interface, κ is the bulk extinction coefficient, α_{∞} is the albedo of an slab of infinite thickness and r is a shorthand defined below. $I_{\downarrow}$ and $I_{\uparrow}$ are the downwelling and upwelling irradiance inside the slab, respectively. The solution above can be approximated by

$$\frac{\partial F^{SW}}{\partial z} = -F_{\downarrow}^{SW}\ (1-\alpha_{\infty})\ \kappa' \left[\exp(-\kappa'\ z) + 1 - \frac{\kappa'}{\kappa}\right],$$

(except near the bottom of thick slabs) where

$$\kappa' = \kappa\left[1 + \frac{m}{\alpha_{\infty}} \exp\left(-2\kappa\ z_0\right)\right], \qquad r = \frac{\alpha_{\infty}^2 - \alpha_{\infty}\alpha_b}{1 - \alpha_{\infty}\alpha_b},$$

α_b is the albedo beneath the slab considered (typically α_b =0 beneath sea ice), and

$$\kappa = \left(\kappa_a^2 + 2\kappa_a\kappa_s\right)^{1/2}, \quad \alpha_\infty = \frac{\kappa - \kappa_a}{\kappa + \kappa_a}$$

are the extinction coefficient (e.g. Perovich, 1980) and albedo of a slab of infinite thickness, respectively, and κ_a and κ_s are bulk absorption and scattering coefficient, respectively. Note that $\kappa=\kappa_a+\kappa_s$ only in the limiting case of single-scattering, i.e. if $\kappa_a >> \kappa_s$.

4.2.3 Snow Deposition, Ablation and Ponding

The processes of snow deposition and melt are included. During ablation of a snow volume Δh_{snow}, meltwater is produced at a ratio of $\Delta h_{pond} = 0.33\ \Delta h_{snow}$.
Snow precipitation for Barrow, Alaska is derived from hourly precipitation measurements reported by NOAA for the Barrow airport. Cumulative snow precipitation over the previous hour is reported as liquid equivalent with a precision of 0.01 inches (0.254 mm), as traces, or as none. The following procedure is used to reproduce the mean snow depth on sea ice at the Seasonal Ice Zone Observing Network (SIZONet) mass balance probe: all reports of traces are translated into 0.0035 inches liquid-equivalent precipitation. Liquid-equivalent precipitation is transferred into snow deposition by multiplying the liquid-equivalent precipitation with 3.

Starting in May, snow ablation in Barrow becomes significant. Two snow melt processes are included, melt due to warming of the surface of the snow pack beyond the melting point of snow, and melt due to a combination of condensation of atmospheric water vapor and enhanced longwave absorption. The former process is based on energy conservation and translates enthalpy due to above-melting temperatures into equivalent melt. This process has to be included explicitly because the phase transition in snow is assumed to be zero in the energy conservation equation. If the temperature of the snow T is above melting, then the following snow depth is being ablated:

$$\Delta h_{snow} = \Delta z\, \frac{\rho_i c_i}{\rho_i L_i}\left(T - T_{melt}\right),$$

where the constants are those of freshwater ice, and T_{melt}=0° C.

The large difference between the latent heat of evaporation and the latent heat of fusion leads to melt as a by-product of condensation in spring and summer. In addition a net heating due to an excess of incoming longwave radiation increases with air temperature (the highest possible snow surface temperature is T_{melt}, regardless how much warmer the air might be). We assume that any time the air temperature exceeds the melting point T_{melt}, snow is ablated at a rate of 2 cm per day for each degree C above melting, i.e. in addition to snow melt calculated above,

$$\Delta h_{snow} = 0.02\ \mathrm{m\,day^{-1}K^{-1}}\left(T - T_{melt}\right)\Delta t\ .$$

It is unlikely that either sublimation or melt of snow is of any significance in winter. While the relative humidity is always quoted with respect to the vapor pressure of water, the relative humidity in the air at Barrow is always 100% with respect to the vapor pressure of ice as long as the air temperature is below freezing. This should effectively prevent net sublimation. Condensation in winter will not lead to ablation because heat conduction and longwave radiative heat loss should lead to immediate freezing of any meltwater.

4.2.4 Ice Growth, Ocean Heat Flux, Surface Ablation

4.2.4.1 Bottom ice growth and melt

Ice growth rate v is determined from the residual of the bottom energy balance, where the ocean heat flux F_w is prescribed, and the vertical conductive heat flux F_c is derived from the temperature gradient in the bottom-most cell, i.e

$$F_c = k_i \frac{T - T_b}{\frac{1}{2}\Delta z},$$

Where T is the average cell temperature, and T_b is the prescribed interface temperature at the bottom. The bottom energy balance is

$$v \rho_i L_i \left(1 - \bar{\phi}\right) = F_c - F_w,$$

where v is the ice growth rate (positive for ice growth), F_c is the upward conductive heat flux (generally positive during freezing), and F_w is the ocean heat flux (positive if heat is supplied to the interface from the ocean). $\bar{\phi}$ is the porosity of the ice formed at the interface for the purpose of energy conservation, typically 0.05 to 0.1.

4.2.4.2 Surface Ablation

Surface melt is a combination of a continuous and a discontinuous process. Continuous warming of ice increases the porosity throughout the slab to a degree that may be structurally very unstable yet a matrix remains in place. Although a significant amount of ice can be melted this way, this process does not initially lead to significant surface ablation. Since melting is generally most pronounced near the surface, this process leads to a continuous reduction of the surface level that is initially small and later possibly very rapid. However, discontinuities in bulk salinity, air inclusions, and sediment concentration can lead a porosity profile with lowest porosity several centimeters below the actual ice surface. In this case, discontinuous surface ablation will occur. If the ice is ponded, chunks of ice detaching from the slab will float to the pond surface and likely melt quickly as lateral meltwater flow within the ponds enhances the heat flux that can be delivered to that ice. If the ice is not ponded then the upper ice layer may sag as ice below it disintegrates. These dynamics of discontinuous surface melt are not considered in this model.

4.3 Results of Different Models

4.3.1 Porous Medium CFD

Using the conservation equations described above, the 2-dimensional, coupled equations are solved in a 2-column domain discretized on a time-independent grid. This is essentially a full-fledged computational fluid dynamics simulation through sea ice. This was the first model implemented and ultimately highlights limitations of this approach, i.e. the necessity to solve the coupled equations at a time step of approximately 1 second, and grid size dependence of the solution.

4.3.1.1 Model Domain, Boundary Conditions, Initial Conditions

The vertical grid size is 10 mm, and the domain is 25 cells high. The left hand side column is 50 mm wide, while the right hand side column is 2.5 mm wide.
The following domain boundary conditions are imposed: fixed temperatures at the top and bottom (T_{top}=const, T_{bottom}=const), no vertical flux through top and bottom boundaries (w_{top}=w_{bottom}=0). The permeability–porosity relationship is isotropic (i.e.

$\Pi = \Pi_z = \Pi_x$) with

$$\Pi = \Pi_0 \phi^3,$$

where $\Pi_0=10^{-8}$ m^2.

The domain is initialized with a temperature/salinity profile and left to evolve freely from there on, constrained by the boundary conditions. Initially, the bottom-most row of cells is liquid and at the freezing point. The temperature T decreases linearly above the bottom row to -5° C at the top of the domain. In the left hand side column, the bulk salinity $S=C$ φ decreases with distance from the interface raised to the power of -8 from 35 to 5 ppt. In the right hand side column, the bulk salinity S is slightly above (by 0.01 ppt) the thermodynamic equilibrium salinity at the given cell temperature.

The initial porosity profile is calculated from

$$\phi = \frac{mS}{T}$$

and confined to $0<\varphi \leq 1$. This results in an initial porosity profile that is supposed to reflect bulk sea ice in the left hand side column, and an all-liquid brine channel in the right hand side column. Figure 4.8 illustrates the initial conditions.

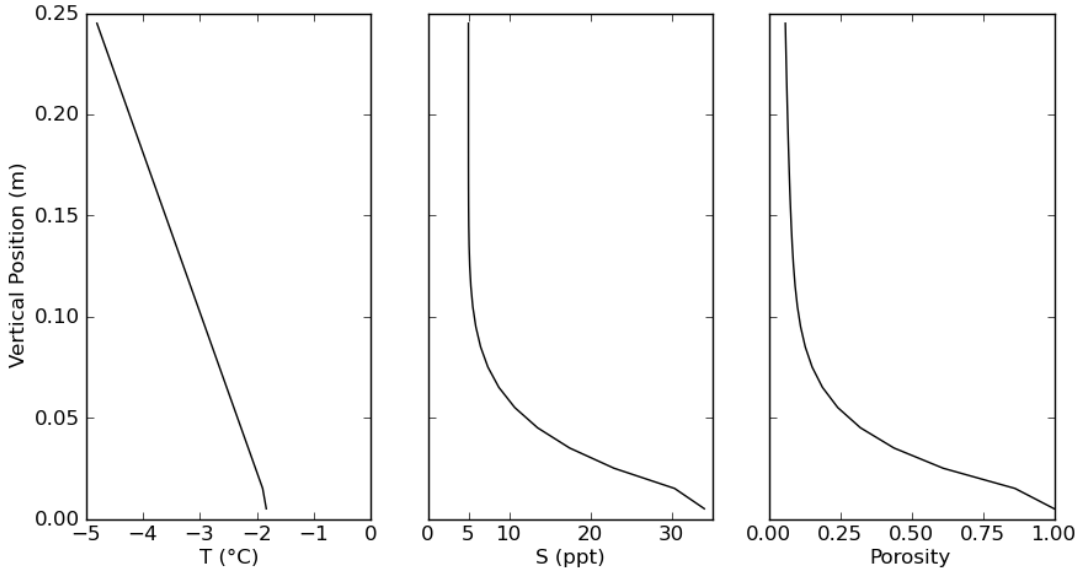

Figure 4.8 Initial vertical profiles of temperature, bulk salinity, and porosity.

4.3.1.2 Results and Discussion

With the fluid initially at rest, the brine flux increases with time to eventually develop an almost steady-state flow field. The simulated time required depends on the permeability of the channel but is generally of the order of t=10^3 s. The model produces vertical ice–ocean interface fluxes of the order of 10^{-6} ms^{-1} in left hand side column, which is the expected order of magnitude. The Courant number limit on the speed of advection limited the computational time step to Δt=3 s. As expected, the flow is upward through the porous medium (left hand side column) and downward through the channel (right hand side column). The magnitude of the flux was found to depend on the size ratio between left-hand-side and right-hand-side column, the permeability of the channel (both of these effects can probably combined to define a representative domain permeability), and the domain width (i.e. channel spacing). This is consistent with laboratory and field measurement on young first-year sea ice. For example, Wakatsuchi and Saito (1985) found a positive association between brine channel density and growth rate, and Wakatsuchi and Ono (1983) determine in ice growth experiments a positive association between growth rate and ice–ocean brine flux.

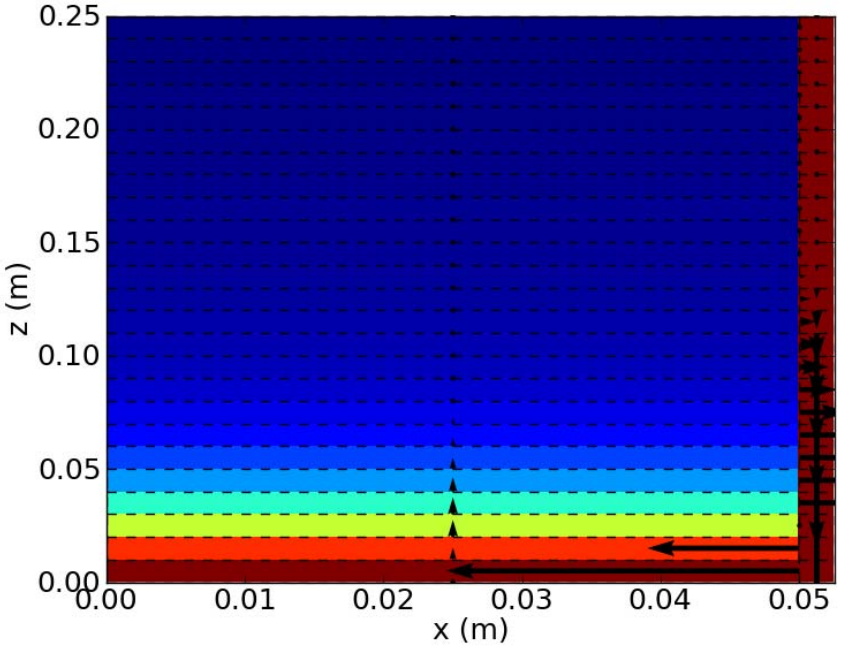

Figure 4.9 Example flow path through in the domain. Arrows indicate the direction of flow, length of arrows is proportional to the flux. Color indicates bulk salinity with dark red 35 ppt or higher, and dark blue 5 ppt in this figure.

These observations can be interpreted as imposing serious limitations on the usefulness of this approach to brine flux calculations:

a. Unlike forced convection, the flow field of natural, buoyancy-driven convection cannot be trivially computed because motion is driven by pressure differences that themselves exist only because the fluid is in motion. There is one trivial solution to a natural convection problem, the state of no convection at all. However, this state is dynamically unstable and any microscopic perturbation will tend to grow in magnitude, eventually resulting in macroscopic fluid motion. Hence, while forced Darcian flow responds to changes in driving forces instantaneously, the flow field in natural convection responds to changes in the environment (e.g. heat flux) with an intrinsic time constant, and fluid dynamics simulations need to resolve this dynamic adjustment.

b. Simulations take a long time. The time step is exceedingly small compared to the length of the seasonal cycle, which is of the order of 3×10^7 s. Even if computations proceed at a rate of one time step every 10 ms wall time (i.e. time the computer is busy), simulating a single year would take more than one day.

c. The size of the convective cells affects the brine flux, and in a two-column formulation the size of the convective cells is prescribed rather than simulated.

The physical size of the natural convective cells was found in experiments to depend on growth conditions. Hence, one might wonder whether it wouldn't be possible and more efficient to prescribe the brine flux directly as a function of growth conditions.

Hence, it was deemed in this project that simulating the fluxes during desalination in response to natural convection is likely to be at least as error prone as parameterizing the fluxes directly (c). Further, using a parameterization of brine fluxes would provide the option to calculate fluxes at discrete instances in time, similar to forced convection, rather than require the continuous calculation of adjustments of the flux (a). With prescribed fluxes, brine redistribution can be calculated explicitly (and hence very quickly), addressing concerns of excessive computational wall time requirements (b).

4.3.2 Weakly Coupled Growth and Flux Models

The approach followed to arrive at a fast-computing ice growth and brine flux model was to decouple temperature simulations from flux/salinity/tracer calculations, and to perform temperature simulations at constant bulk salinity on a rather coarse grid. In a separate step, high resolution simulations are performed for the advection of salinity and tracers, using an interpolated temperature profile. Rather than using a fixed grid to simulate temperature profile and ice thickness, it was assumed that a Semter (1976)-type model could be sufficiently accurate. Semter proposed the use of a three-layer model, one layer to characterize snow, and two layers for sea ice. All layers are time-varying in thickness.

4.3.2.1 Governing Equations

As a result of the decoupling, an inner loop to explicitly solve for temperature and phase transition can be avoided because the bulk salinity is assumed to be constant (typically around 5 to 10 ppt) for the purpose of thermal calculations. The latent heat release during phase transition is therefore folded into the heat capacity (Petrich and Eicken, 2010). The effective heat capacity of sea ice of constant bulk salinity S can be expressed in terms of the change in enthalpy H with temperature as

$$(\rho c)_{seaice} = \left(\frac{\partial H}{\partial T}\right)_{S=\cos nt} = \frac{\partial}{\partial T}\left[\rho_i c_i T + \Delta\rho c\,\phi T - \rho_i L_i\,(1-\phi)\right] = \rho_i c_i + \Delta\rho c\,\phi + \left[\Delta\rho c T + \rho_i L_i\right]\frac{\partial \phi}{\partial T}$$

,

and using the equation of state $\phi = \frac{mS}{T}$, the derivative of porosity with respect to temperature at constant salinity S is

$$\left(\frac{\partial \phi}{\partial T}\right)_{S=const} = -\frac{mS}{T^2} = -\frac{\phi}{T}.$$

Hence,

$$(\rho c)_{seaice} = \rho_i c_i - \rho_i L_i \frac{\phi}{T} = \rho_i c_i - \rho_i L_i \, m \frac{S}{T^2} .$$

This equation is identical to the empirical relationship given by Untersteiner (1961). With this expression, the energy conservation equation simplifies to

$$(\rho c)_{seaice} \frac{\partial T}{\partial t} = \frac{\partial}{\partial x}\left[\bar{k}\frac{\partial T}{\partial x}\right] + \frac{\partial}{\partial z}\left[\bar{k}\frac{\partial T}{\partial z}\right] + \left|\frac{\partial F_{SW}}{\partial z}\right| .$$

For the purpose of simulating the temperature profile, the bulk sea ice salinity is assumed to be S=5 ppt, regardless of position within the ice.

Bulk salinity and tracer concentration are tracked on a grid independent of the temperature simulations. The grid used for salinity and tracers is equidistant and has a grid size that is fixed at Δz=10 mm. During each time step, the volume of ice grown is calculated in conjunction with the bulk salinity and tracer uptake that would have taken place in that volume. The total bulk salinity and tracer mass of a cell is then the volume-averaged bulk salinity and volume-integrated tracer mass, respectively.
Ice–ocean interface flux and bulk salinity developed during ice growth are parameterized. For the bulk salinity, the results of Petrich et al. (2006) are used and the stable bulk salinity is calculated from the instantaneous growth rate v,

$$S = 34 \times 0.14 \times \left(\frac{v}{1.35 \times 10^{-7} \text{ m/s}} \right)^{0.33} .$$

While the majority of the desalination usually takes place over the course of a week, this approach assumes instantaneous desalination. As a consequence, the simulated bulk salinity is too low by design in the bottom 0.1 m of the ice during growth, only.

The interface flux of tracers into the ice is parameterized as

$$\phi w = \left(10^{-4} \text{ s/m } v\right)^{0.5} .$$

Tracers are accumulated in the bottom-most cell of the ice. However, in this study tracers were injected with relative mass 1.0 at discrete, pre-defined horizons to visualize brine movement and dispersion later during the melt season.

The brine flux within the ice is calculated on a separate grid with specified number of cells. The porosity is the mean porosity of the salinity cells, calculated from the bulk salinity of the salinity cells and temperature profile, linearly interpolated to the respective salinity cells according to

$$\phi = \frac{mS}{T}.$$

The permeability of the brine channel is assumed to be infinite. As a consequence, the pressure profile in the brine channel is the prescribed hydrostatic pressure. This reduces calculations of the brine flux to a one-dimensional problem that can be solved for very efficiently. The upper pressure boundary conditions in the porous medium column are constant pressure, with the hydrostatic pressure of the ponded water at the upper surface, and the integrated hydrostatic pressure of the column at the bottom surface. The upper pressure boundary of the brine channel column is assumed to be zero. For the sake of calculation of forced convection, the density of the fluid is taken to be independent of salinity and hence independent of position, in both porous layer column and brine channel column. For the purpose of forced convection, the following permeability parameterizations are used.

$$\Pi_z = 3\times10^{-9}\,\mathrm{m}^2\ \phi^3,$$
$$\Pi_x = 6\times10^{-11}\,\mathrm{m}^2\ \phi^3.$$

Further, $\Delta x = 0.1$ m.

The pressure boundary conditions for the porous medium column are

$$p_{top} = -\rho_w g\ h_{pond} \text{ and}$$
$$p_{bottom} = -\sum \rho_w g\ \Delta z.$$

In this configuration, the bottom pressure is the hydrostatic pressure in the absence of pressure loading of the liquid, while the surface pressure is the air pressure (set to 0) increased by a load proportional to the meltpond depth. Hence, downward movement will be introduced in the presence of meltwater. Note that the freeboard level is not accounted for.

The pressure boundaries used to calculate the parabolic pressure profile in the brine channel are

$$p_n^{bnd} = -0.5\rho_w g\ h_{pond} \text{ and}$$
$$p_s^{bnd} = -0.5\rho_w g\ h_{pond} - \sum \rho_w g\ \Delta z,$$

corresponding to a hydrostatic water column that is loaded with a water level of half the pond depth.

4.3.2.2 Results and Discussion

The model was driven with data of observed snow precipitation and air temperatures at the Barrow airport, assuming an ocean heat flux of 0. Air temperature data are shown in Figure 4.10 for reference. Figure 4.11 shows a comparison between field measurements of thickness and temperature profiles and model output.

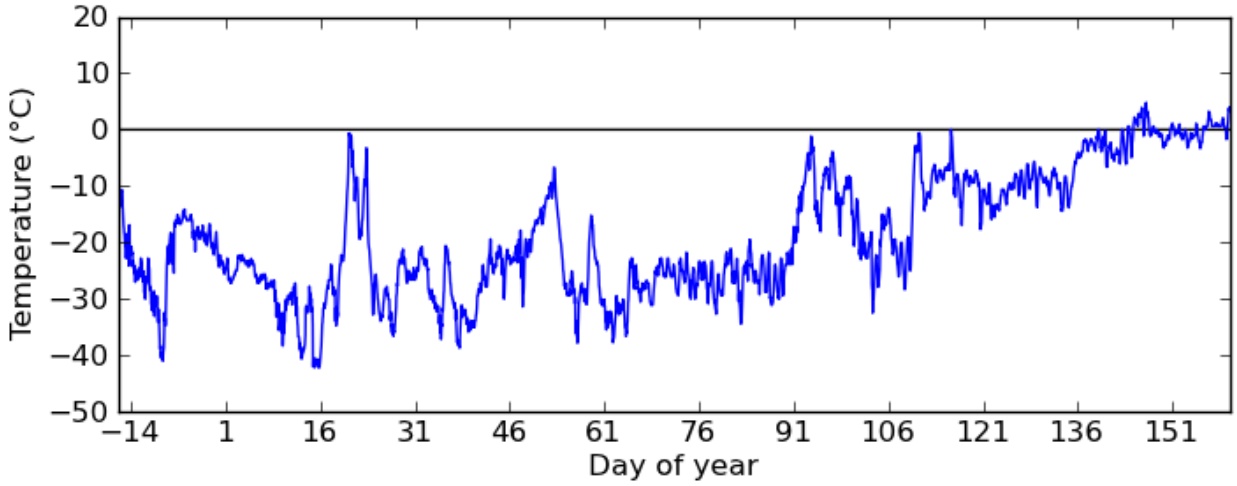

Figure 4.10 Air temperature observed at the Barrow airport in 2008.

Field data were acquired with a thermistor string that contained 30 thermistors separated vertically by 0.1 m, with the upper-most thermistor located 0.4 m above the ice–snow interface. Independent snow and ice thickness measurements were performed with acoustic sounders located approx. 10 m from the thermistor string.

Note that in the field data, snow depth and ice thickness data are measured approximately 5 m separated from the air–snow–ice–water temperature profile. The model simulations start on the observed date of ice formation. The plot in the middle is based on a model simulation with a single snow layer and two ice layers, while the output at the bottom is based on a run with 15 snow layers and 100 ice layers. Differences between the temperature output of the models are most pronounced in spring when the model predict significantly different snow depth. The temperature profile modeled with high resolution agrees well with the observed temperature profile. However, surface ablation of ice sets in later than observed in 2008 (data not shown). The depth-propagation of diurnal temperature fluctuations is exaggerated in the simulation with small number of cells.
The corresponding simulated example bulk salinity profile is shown in Figure 4.12. The bulk salinity due to natural convection at the ice–ocean interface is parameterized as reasoned for in Section 3.1. It is stable by design in winter but starts to change as the ice begins to warm in summer. As expected, flushing of surface meltwater reduces the surface salinity and creates a bulk salinity profile that increases with depth.

Simultaneously, the bulk salinity near the bottom of the ice decreases in response to brine channel-borne freshwater that infiltrates the porous medium. Bulk desalination at the center of the ice is less pronounced because temperature and brine salinity are nearly independent of depth, hence the vertical flux does not contribute to desalination.

The corresponding tracer mass profile is shown in Figure 4.13. Noticeable movement of tracers starts around day 110, and tracers move downward as the season progresses. Tracer concentration decreases as the individual pockets get dispersed by water that infiltrates the porous medium laterally from the brine channel. The direction of lateral flow is shown in Figure 4.14.

Comparison of the downward flux in Figure 4.15 with the temperature profile in Figure 4.10 shows that rather than being continuous, the downward flux increases during hot spells.

Selected profiles of temperature, bulk salinity, porosity, and tracer mass during melt are shown in Figure 4.16. This figure may be compared to the figures in the introduction, specifically Figure 4.3 and Figure 4.4. The temperature plot in Figure 4.16 indicates that the lowest temperature is consistently at the center of the ice. Bulk salinity decreases with time, and tracers disperse. Note that, compared with field observations, the bulk salinity at the surface should have been closer to 0 at the end of the simulations.

Magnitude and, to a limited extent direction of fluxes depends on the combination of vertical and lateral permeabilities and on pressure boundary conditions. For example, if the bottom pressures of channel is and porous medium are equal (i.e. no meltwater load on the channel), desalination tends to be limited to the near-surface region of the ice. If the surface pressure of channel and porous medium are equal (i.e. channel is loaded with meltwater), desalination tends to be limited to the near-bottom regions of the ice. In addition, the parameter space spanned by magnitude of permeability and porosity-dependence of permeability of both Π_x and Π_z affects the mode of preferential drainage, i.e. whether most fluid motion happens at the surface or at the bottom, or whether significant vertical brine movement takes place.

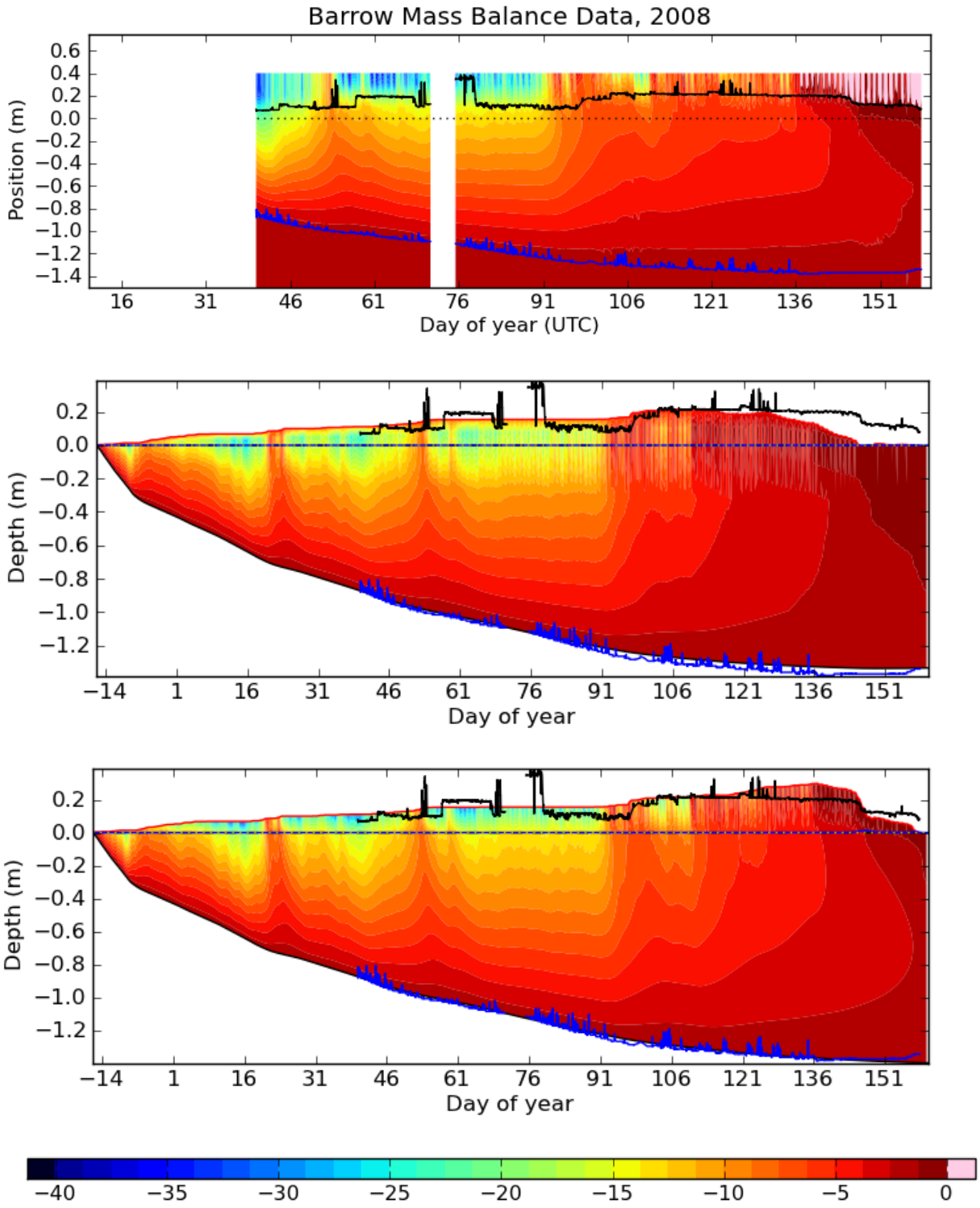

Figure 4.11: Comparison of Mass Balance temperature profile, ice thickness and snow depth data (top) with simulations using three layers (center) and over 100 layers (bottom). Note the different scales. Temperature (in °C) profiles use the same color scale. Note that missing temperature data around day 75 are interpolated in the topmost figure. Measured snow depth is shown as a black line, measured ice thickness is shown as the blue line.

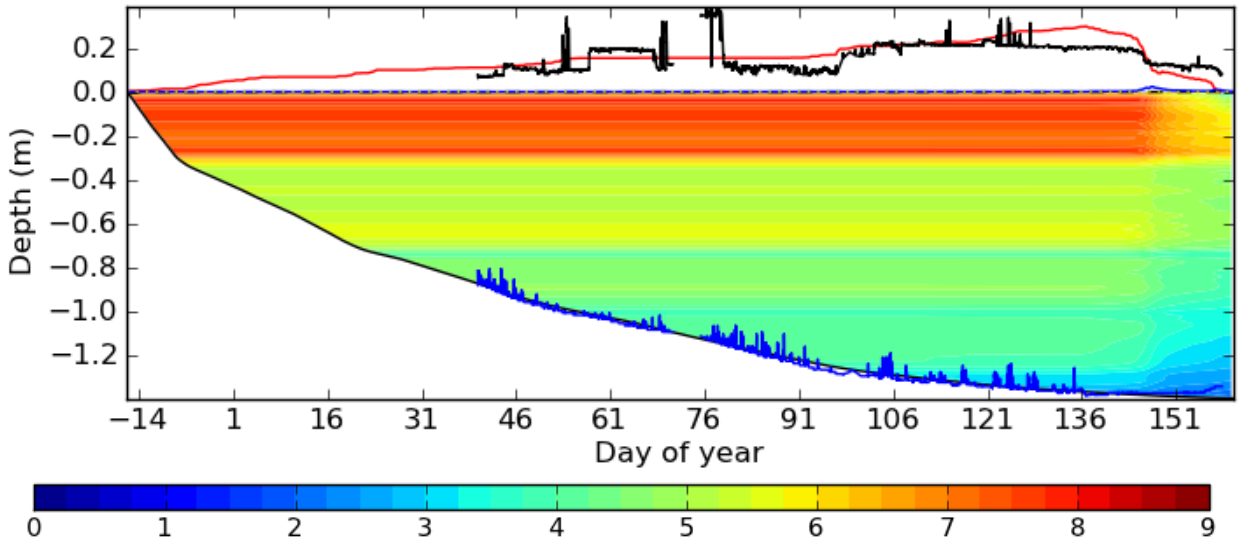

Figure 4.12 Evolution of the simulated bulk salinity profile in 2008. Salinity is given in ppt.

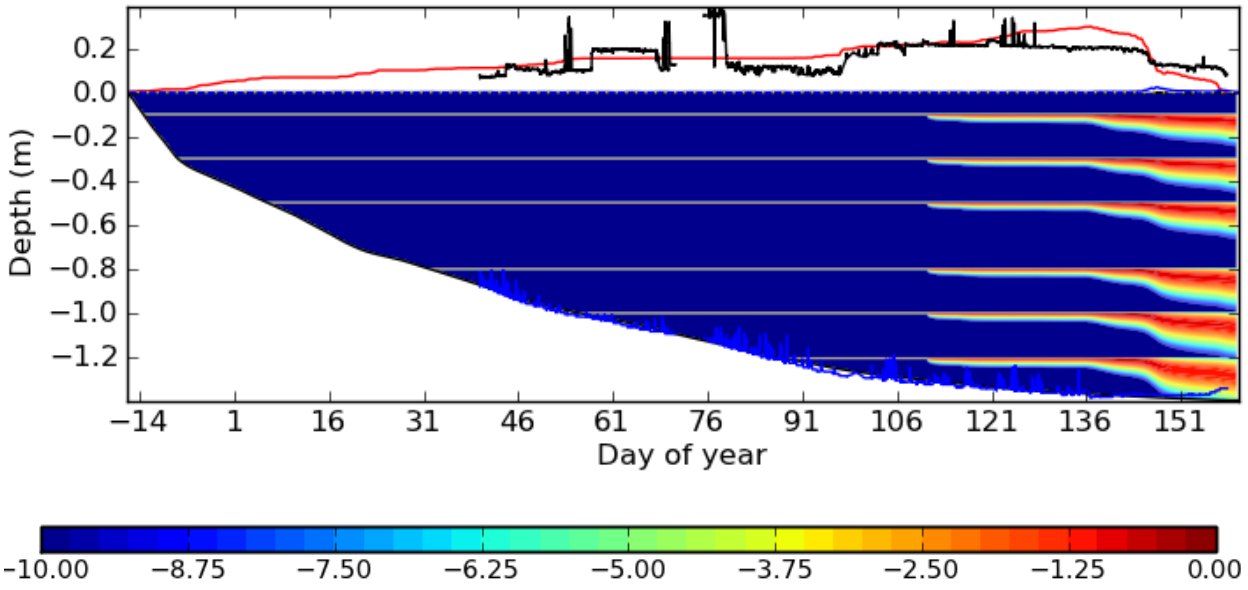

Figure 4.13 Relative concentration of tracers on logarithmic scale (base 10).

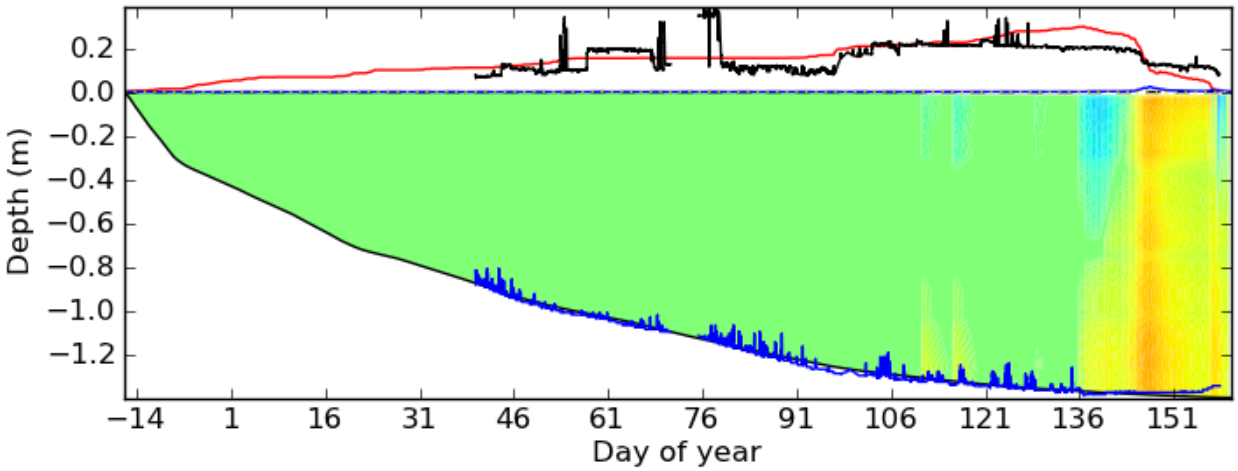

Figure 4.14 Illustration of the direction of the lateral flux on logarithmic scale. Blue indicates brine leaving the pore space into the channel, while yellow indicates brine moving from the channel into the pore space.

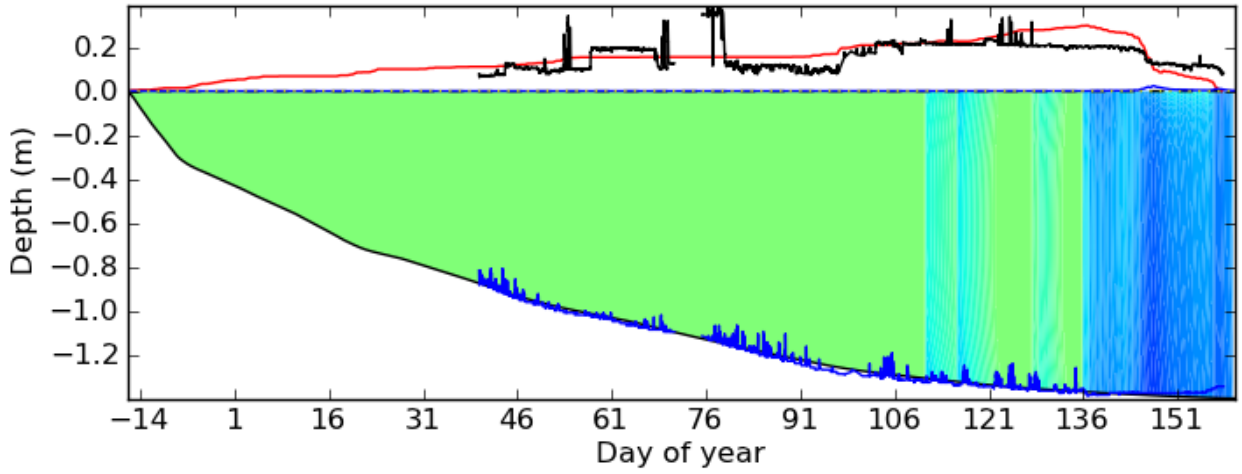

Figure 4.15 Illustration of the time-dependence of the vertical flux on logarithmic scale. Blue indicates downward movement, while green is stationary.

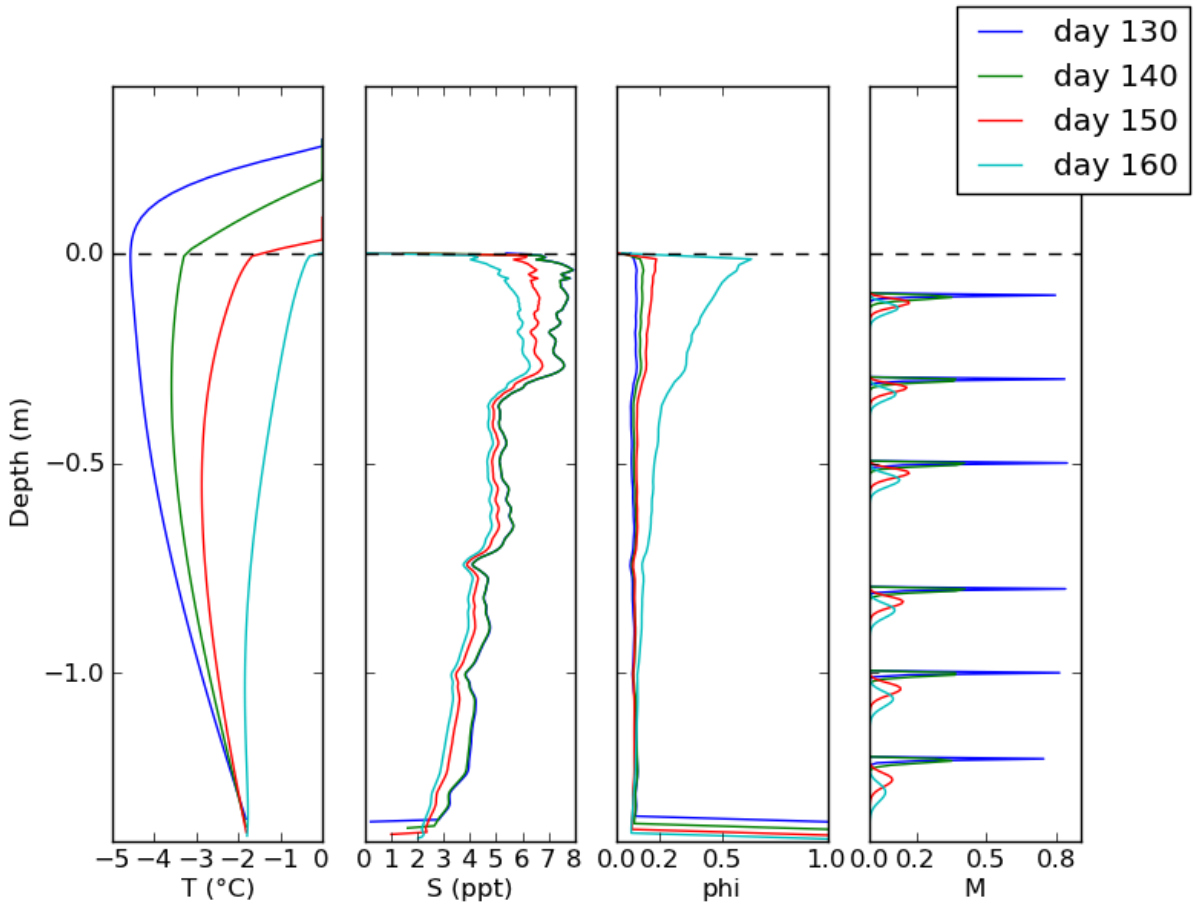

Figure 4.16 Simulated vertical profiles of temperature, bulk salinity, porosity, and tracer mass at selected times.

4.4 Summary and Conclusion

This work represents an attempt to join a thermal model of snow and sea ice growth and melt with ice-internal fluxes, including natural convection during ice growth, forced convection during desalination, and exchange between fluid in porous medium and brine channels. At the same time, high numerical efficiency has been sought. In accomplishing these goals, the project has been relatively successful.

It was found that first-principle fluid-dynamics simulations in a two-column system took too much time to compute and that they introduced grid-size dependence of the ice–ocean interface flux during natural convection. In order to address the problem of computational speed, thermal evolution and fluid dynamics were decoupled at the possible expense of numerical accuracy. Further, brine channels were assumed to have infinite permeability, which allowed for extremely efficient computation of the flow field. In order to address the grid-size dependence, parameterizations of natural convection were introduced.

An ice growth model was implemented based on a fixed number of grid cells that are adjusted in size during growth and melt. A description of surface ablation of ice was included, although this could not be thoroughly validated in this project and should be revisited in future work.

An approach was developed to derive snow depth from precipitation measurements, and to quantify snow ablation based on air temperature reports. Compared with field measurements, simulated snow depth appears to be realistic. In conjunction with the ice growth model, derived ice temperature profiles reproduce field measurements well.

It was found that there is little computational advantage in keeping the number of grid cells small in 1-dimensional simulations. Hence, the approach of using three different grids, for temperature, solute and tracer concentration, and pressure and flow field, respectively, proved to introduce unnecessary complications.

Based on the simulated development of bulk salinity profile, the flow field inside sea ice may have been reproduced qualitatively correctly. However, it became clear that the parameter space is large, in spite of simplifying assumptions such as those of constant brine density and infinite vertical permeability of brine channels. In addition, the current investigations do not include drainage effects due to finite freeboard, and porosity due to air entrained in the ice. Clearly, pressure boundary conditions and permeability parameter space are areas for future investigations, possibly including an analytical investigation of qualitative fluid motion.

Future work should include the development of a better description of surface ice melt, and the treatment of water-soluble compounds that travel at rates slower than the fluid velocity.

The experience gained from the numerical implementation of the models described above leads to the conclusion that, in future, a 1-dimensional implementation should be considered based on a grid with fixed cell sizes in the ice domain. Using variable cell

sizes with the potential to reduce computation effort proved instructive as seen in the case of the temperature profiles, but the merit is limited for strictly 1-dimensional simulations where numerical solutions can be obtained extremely efficiently with direct solvers, such as with a Tri-Diagonal Matrix Algorithm (TDMA) that scales with $O(N)$.

4.5 Acknowledgements

Sea ice field data were obtained from Nation Science Foundation (NSF) Office of Polar Programs project OPP-0632398 and OPP-0856867 (SIZONET). Air temperature and precipitation data at Barrow, Alaska (PABR), were extracted from aviation weather reports of the National Oceanic and Atmospheric Administration (NOAA). The photos were taken by Chris Petrich.

5 Discussion and importance to oil spill response/restoration

The ice-column experiments have shown that there is a downwards migration of water soluble oil components from oil encapsulated in the ice, and that the migrating starts after spring thawing has increased the porosity of the ice. As long as the temperature in the ice is relatively low, the migration seems to be negligible. These observations are in accordance with the findings in field experiments in first-year sea ice on Svalbard (Faksness and Brandvik, 2008a and 2008b). In addition, migrating oil compounds may be subjected to slow biodegradation. However, the degree of complete mineralization has not been investigated in the current project. The results of the biodegradation studies are in agreement with a previous field study from Svalbard where sea ice bacterial communities were significantly impacted by oil pollution in the ice (Brakstad et al., 2008).The content of bio-available WSC and their estimated acute toxicity in the brine channels have been calculated. The HI values for the ice core samples are below one for all reported samples (ranging from 0.001 to 0.96), implying that the concentration in the ice samples (5 cm sections) were not high enough to represent an acute toxicity to local marine biota. The estimated toxicity was highest just below the encapsulated oil, and summarizing the HI for all samples in the column with highest concentration of WSC gives an HI of 1.1, indicating that the toxicity in the brine channels might be toxic to the ice habitants. The calculation of estimated toxicities in the ice are very approximate, particularly because they are based on brine volumes an on the assumption that the transport of WSC solely happens through the brine channels. Nevertheless, these results indicate that the ice organisms might be exposed to toxic WSC over several months, causing potentially toxic oil components to enter the Arctic marine food web. Biodegradation of the WSC may attribute to the toxicity of the migrating compounds. If degradation processes results in detoxification of harmful compounds this may be of importance to the survival and restoration of ice organisms. However, previous studies have shown that the acute toxicity may not be immediately reduced during biotransformation (Brakstad et al., 1999). However, once released in the seawater below the ice most WSCs will biodegrade at a faster speed than in the ice, as show in this and previous studies (Brakstad and Bonaunet, 2006).

The experiments have demonstrated that the simulation of ice growth and spring thawing is a challenge in the laboratory. The ice growth conditions seem to be similar to natural conditions, but the spring thawing is more difficult to simulate, as the experiments are performed in a closed system where natural processes such as tide movements, currents and sunlight (albedo effect) are not included. Faksness and Brandvik (2008b) observed an upward migration of oil during their field experiments on Svalbard, but no upward transport was observed during the melting process in these laboratory experiments, indicating that the tide movement, sunlight, and albedo effect are important factors that should be taken into account in future experiments.

It was not possible from the current experiments to determine if bioremediation by traditional nutrient supply was an option for stimulated oil biodegradation in the ice. Since no degradation was measured in the oil phase, traditional fertilizers need to be reformulated if used in ice. Oleophilic fertilizers may not be efficient due to the low

temperatures in the ice, and the salt compositions of the brines may influence the efficiency of traditional fertilizers. If bioremediation is an option in ice it is therefore important to investigate novel systems specially designed for improving biodegradation in sea ice brine.

The 1-D model developed here is appropriate for implementation as a sub-model or module in regional ice models, such that numerical forecasting experiments can be carried out to determine the extent to which oil frozen into the ice may eventually represent a risk to biota during the melting phase. The model therefore represents a contribution to decision support tools for oil spill response in the Arctic

The overall objective with this project has been to gain new knowledge regarding encapsulation of oil in ice with focus on transport and degradation of oil and water soluble components. This knowledge needed for both operational use and for environmental risk and impact assessments. The findings presented in this report represent an important contribution and improvement of our present understanding of oil encapsulation in ice. At present state it is difficult directly to utilize these findings in response operations with oil in ice. However, when these findings are implemented into models describing the fate of oil spills in ice, they will contribute to decision support tools for oil spill response in the Arctic.

6 Technology transfer

The results of this work will be published in international scientific journals and/or conferences.

7 Achievement and dissemination

The publishing journals have not yet been selected for the possible manuscripts, but both Marine Pollution Bulletin and Cold Regions Science and Technology are relevant refereed journals.

References: Transport and physical fate of oil hydrocarbons in ice

Brandvik, P.J., I. Singsaas, and P.S. Daling. 2004. Oil Spill R&D in Norwegian Arctic Waters with special Focus on Large-scale Oil Weathering Experiments. In Proceedings from INTERSPILL 2004, Trondheim Norway.

Chen, E.C., C.K. Overall, and C.R. Phillips. 1974. Spreading of crude oil on an ice surface. Can J Chem Engineer 52: 71-74.

Cox, G.F.N., and W.F. Weeks. 1983. Equations for determining the gas and brine volumes in sea-ice samples. Journal of Glaciology, 29(102), 306-316

DiToro, D.M., J.A: McGrath, and W.A. Stubblefield. 2007. Predicting the toxicity of neat and weathered crude oil: Toxic potential and the toxicity of saturated mixtures. Environmental Toxicity and Chemistry 26: 24-36.

Eicken, H. 2003. From the microscopic to the macroscopic to the regional scale: Growth, microstructure and properties of sea ice. In Sea ice – An introduction to its physics, biology, chemistry and geology (Thomas, D. and Dieckmann, G.S (eds)). Blackwell Science, London, pp. 22-81

Eicken, H., and J. Karlsson. 2009. Report on stratigraphic analysis of artificial sea ice grown in columns at SINTEF, Trondheim, Norway – March 2009.

Eicken H., 2010. Personal communication – Notes on SINTEFs oil in ice experiments, May 14, 2010.

Faksness, L.G., and P.J. Brandvik. 2005. Dissolution of water soluble components from oil spills encapsulated in ice. In proceedings to the 28th Arctic and Marine Oilspill Program Technical Seminar, Calgary, Canada, June 7-9, 2005, 59-74.

Faksness, L.G., and P.J. Brandvik. 2008a. Distribution of water soluble components from Arctic marine oil spills – a combined laboratory and field study. Cold Region Science and Technology 54: 97-105.

Faksness, L.G., and P.J. Brandvik. 2008b. Distribution of water soluble components from oil encapsulated in Arctic sea ice. Summary of three field seasons. Cold Region Science and Technology 54, 106-114.

Faksness, L.G., P.J. Brandvik, and L.K. Sydnes . 2008. Chemical characterization of water soluble components from Arctic marine oil spills – A combined laboratory and field study. Marine Pollution Bulletin 56:1746-1754.

Fingas, M.F. and B.P. Hollebone. 2003. Review of behaviour of oil in freezing environments. Mar Poll Bull 47: 333-340.

French McCay, D.P. 2002. Development and application of an oil toxicity and exposure model, OilToxEx. Environmental Toxicology and Chemistry 21, 2080-2094.

Kawamura P., D. Mackay, and M. Goral. 1986. Spreading of chemicals on ice and snow. Environment Canada Report EE79, pp 106.

Lohmann, R. 2010. Detecting dissolved PAHs from oil spills using passive samplers in cold water and ice cores. Final report to CRRC.

Martin, S. 1979. A field study of brine drainage and oil entrainment in first-year sea ice. Journal of Glaciology 22, 473-502.

McCarty, L.S., Mackay, D., Smith, A.D., Ozburn, G.W., and Dixon, D.G. (1992). Residue-based interpretation of toxicity and bioconcentration QSARs from aquatic bioassays: Neutral narcotic organics. Environmental Toxicology and Chemistry 11, 917-930.

McCarty, L.S., Mackay, D., Smith, A.D., Ozburn, G.W., and Dixon, D.G. (1993). Residue-based interpretation of toxicity and bioconcentration QSARs from aquatic bioassays: Polar narcotic organics. Ecotoxicology and Environmental Safety 25, 253-270.

Neff, J.M. 2002. Bioaccumulation in marine organisms. Effects of contaminants from oil well produced water. Amsterdam, The Netherlands: Elsevier. 452 p.

Neff, J.M. Stout, S.A., and Gunstert, D.G. 2005. Ecological risk assessment of polycyclic aromatic hydrocarbons in sediments: Identifying sources and ecological hazard. Integrated Environmental Assessment and Management, 1, 22-33

Neff, J.M., S. Johnsen, T.K. Frost, T.I.R. Utvik, and G.S. Durell, 2006. Oil well produced water discharges to the North Sea. Part II: Comparison of deployed mussels (*Mytilus edulis*) and the DREAM model to predict ecological risk. Marine Environmental Research 62, 224-246.

NORCOR Engineering and Research Ltd. 1975. The interaction of crude oil with arctic sea ice, Beaufort Sea Technical Report, No. 27, Beaufort Sea Project, Department of the Environment, Victoria, BC, 201 p.

Payne, J.R., G.D. McNabb, and J.R. Clayton. 1991. Oil-weathering behavior in Arctic environments. Polar Research 9, 631-662.

Reed, M., Ø. Johansen, P.J. Brandvik, P.S. Daling, A. Lewis, R. Fiocco, D. Mackay, and R. Prentki. 1999. Oil Spill Modeling towards the Close of the 20th Century: Overview of the State of the Art. Spill Science and Technology Bulletin, Vol. 5, no. 1, pp.3-16.

US EPA, 1996. Method 3510C. Separatory Funnel Liquid-Liquid Extraction. http://www.epa.gov/wastes/hazard/testmethods/sw846/pdfs/3510c.pdf

US EPA, 1986. Method 8100. Polynuclear Aromatic Hydrocarbons. www.epa.gov/osw/hazard/testmethods/sw846/pdfs/8100.pdf

US EPA, 2007. Method 8270D. Semivolatile Organic Compounds by GC/MS. http://www.epa.gov/wastes/hazard/testmethods/sw846/pdfs/8270d.pdf

References: Biodegradation in marine ice

Berger, F., Morellet, N., and Corrieu, G. 1996. Cold shock and cold acclimation proteins in the psychrophilic bacterium *Arthrobacter globiformis* SI55. *Journal of Bacteriology* 178:2999-3007.

Bowman, J.P., McCammon, S.A., Brown, M,V,, Nichols,D.S., and McMeekin, T.A. 1997. Diversity and association of psychrophilic baceria in Antarctic sea ice. *Applied Environmental Microbiology* 63:3068-3078.

Brakstad, O.G., and Bonaunet, K. Biodegradation of petroleum hydrocarbons in seawater at low temperatures (0-5°C) and bacterial communities associated with degradation. *Biodegradation* 17: 71 – 82, 2006.

Brakstad, O.G, Daling, P.S., Faksness, L.-G. and Singsås, I. (1999). Biodegradation in seawater of oil components in the water-accomodated fraction (WAF). Proceedings to the 1999 Arctic and Marine Oilspill Program Technical Seminar, Calgary, Canada, June 2-4 1999.

Brakstad, O.G. and Faksness, L.-G. (2000). Biodegradation of water-accommodated fractions and dispersed oil in the seawater column. *Proceedings to the SPE International Conference on Health, Safety, and the Environment in Oil and Gas Exploration and Production*, Stavanger, Norway, 26–28 June 2000.

Brakstad, O.G., Nonstad, I., Faksness, L.-G., and Brandvik, P.J. 2008: Responses of microbial communities in Arctic sea ice after contamination by crude petroleum oil. *Microbial Ecology*. 55: 540-552.

Breezee, J., Cady, N., and Staley, J.T. 2004. Subfreezing growth of the sea ice bacterium "*Psychromonas ingrahamii*". *Microbial Ecology* 47:300-304.

Brinkmeyer, R., Knittel, K., Jürgens, J., Weyland, H., Amann , R., and Helmke, E. 2003. Diversity and structure of bacterial communities in Arctic versus Antarctic pack ice. *Applied and Environmental Microbiology* 69:6610-6619.

Børresen, M.H., Barnes, D.L., and Rike, A.G. 2007. Repeated freeze-thaw cycles and their effects on mineralization of hexadecane and phenanthrene in cold climate soils. *Cold Regions Science and Technology* 49: 215-225.

Chintalapati, S., Kiran, M.D., and Shivaji, S. 2004. Role of membrane lipid fatty acids in cold adaptions. *Cellular and Molecular Biology* 50:631-642.

Collins, T., Roulling, F., Piette, F., Marx, J.-C., Feller, G., Gerday, C., and D'Amico, S. 2008. fundamental of cold-adapted enzymes. In: *Psychrophiles. From biodiversity to biotechnology*, ed. R. Margesin, F. Schinner, J.-C. Marx, and C. Gerday, 211-227. Springer-Verlag, Berlin, Heidelberg.

Delille, D., Basseres, A., and Dessommes, A. 1997. Seasonal variation of bacteria in sea ice contaminated by diesel fuel and dispersed crude oil. *Microbial Ecology*. 33: 97-105.

Delille, D., Basseres, A., and Dessommes, A. 1998. Effectiveness of bioremediation for oil-polluted Antarctic seawater. *Polar Biology* 19: 237-241.

Deppe, U., Richnow, H.-H., Michaelis, W., and Antranikian, G. 2005. Degradation of crude oil by an arctic microbial consortium. *Extremophiles* 9:461-470.

Faksness, L.-G., and Brandvik, P.J. 2005. Dissolution of water soluble components from oil spills encapsulated in ice. Proceedings to the 2005 Arctic and Marine Oilspill Program Technical Seminar, Calgary, Canada, pp. 59-73.

Fiala, M., and Delille, D. 1999. Annual changes of microalgae biomass in Antarctic sea ice contaminated by crude oil and diesel fuel. *Polar Biology* 21: 391-396.

Fingas, M.F., and Hollebone, H.P. 2003. Review of the behaviour of oil in freezing environments. *Marine Pollution Bulletin* 47: 333-340.

Gerdes, B., Brinkmeyer, R., Dieckmann, G., and Helmke, E. 2005 Influence of crude oil on changes of bacterial communities in Arctic sea-ice. *FEMS Microbiology Ecolology* 53: 129-139.

Gerdes, B., and Dieckmann, G. Biological degradation of crude oil in sea ice. Abstract to the report "Growth Project GRD-2000-30112 ARCOP Technology and Environment WP 6 Workshop Activities, 16.02.2006 (http://www.arcop.fi/reports/workshop_report8.pdf).

Groudieva, T., Kambourova, M., Yosuf, H., Royter, M., Grote, R., Trinks, H., and Antranikian, G. 2004. Diversity and cold-active hydrolytic enzymes of culturable bacteria associated with Arctic sea ice, Spitzbergen. *Extremophiles* 8:475-488.

Hokstad, J.N., Faksness, L.-G., Daling, P.D. and Almås, I.K. (1999). Chemical Characterization and Microtox ® Testing of Water-Accomodated Fractions, *Proceedings to the 3d MEMS*, Lillehammer, Norway, pp. 15.

Jaraula, C.M.B., Kenig, F., Doran, P.T., Priscu, J.C. and Welch, K.A. (2009). Composition and biodegradation of a synthetic oil spilled on the perennial ice cover of Lake Fryxell, Antarctica. *Environmental Science and Technology* 43: 2708.2713.

Junge, K., Eicken, H., and Deming, J.W. 2003. Motility of *Colwellia psychrerythraea* strain 34H at subzero temperatures. *Applied and Environmental Microbiology* 69: 4282-4284

Junge, K., Eicken, H., and Deming, J.W. 2004. Bacterial activity at -2 and -20°C in Arctic wintertime sea ice *Applied and Environmental Microbiology* 70: 550-557

Junge, K., Eicken, H., Swanson, B.D., and Deming, J.W. 2006. Bacterial incorporation of leucine into protein down to -20°C with evidence for potential activity in sub-eutectic saline formations. *Cryobiology* 52: 417-429.

Junge, K., Imhoff, F., Staley, T., and Deming, J.W. 2002. Phylogenetic diversity of numerically important Arctic sea-ice bacteria cultured at subzero temperature. *Microbial Ecology* 43:315-328.

Kawahara, H. 2008. Cryoprotectants and ice-binding proteins. In: *Psychrophiles. From biodiversity to biotechnology*, ed. R. Margesin, F. Schinner, J.-C. Marx, and C. Gerday, 2229-246. Springer-Verlag, Berlin, Heidelberg.

Lozada, M., Mercadal, J.P.R, Guerrero, L.D., Di Marzio, W.D., Ferrero, M.A., and Dioniso, H.M. 2008. Novel aromatic ring-hydroxylating dioxygenase genes from coastal marine sediments of Patagonia. *BMC Microbiology* 8:50. Open Access article (http://www.biomedcentral.com/1471-2180/8/50).

Luz, A.P., Pellizari, V.H., Whyte, L.G., and Greer, C.W. 2004. A survey of indigenous microbial hydrocarbon degradation genes in soils from Antarctica and Brazil. *Canadian Journal of Microbiology* 50:323-333.

Michaud L, Lo Giudice A, Saitta M, De Domenico M, Bruni V (2004) The biodegradation efficiency on diesel oil by two psychrotrophic Antarctic marine bacteria during a two-month-long experiment. *Mar Poll Bull* 49: 405-409.

Mock T and Thomas DN (2005) Recent advances in sea-ice microbiology. *Environmental Microbiology*. 7:605-619.

Muyzer G, Dewaal EC & Uitterlinden AG (1993) Profiling of complex microbial populations by denaturing gradient gel electrophoresis analysis of polymerase chain reaction-amplified genes coding for the 16S rRNA. *Appl Environ Microbiol* 59: 695-700.

Rand, M.C., A.E. Greenberg and M.J. Taras (Eds.), *Standard Methods for the Examination of Water and Wastewater*, 14th edition. American Public Health Association, Washington DC, 1193 p., 1975.

Rike, A.G., Haugen, K.B., Børresen, M., Engene, B., and Kolstad, P. 2003. In situ biodegradation of petroleum hydrocarbons in frozen arctic soils. *Cold Regions Science and Technology* 37: 97-120.

Sambrook J, Russel DW (eds) Molecular Cloning. A Laboratory Manual. Third edition. Cold Spring Harbor Laboratory Press, New York 2001

Teske A, Wawer C, Muyzer G & Ramsing NB (1996) Distribution of sulfate-reducing bacteria in a stratified fjord (Mariager Fjord, Denmark) as evaluated by most-probable-

number counts and denaturing gradient gel electrophoresis of PCR-amplified ribosomal DNA fragments. *Appl Environ Microbiol* 62: 1405-1415

Whyte, L.G., Slagman, S.J., Pietrantonio, F., Bourbonniére, L., Koval, S.F., Lawrence, J.R., Inniss, W.E., and Greer, C.W. 1999. Physiological adaptations involved in alkane assimilation at a low temperatures by *Rhodococcus* sp. strain Q15. *Applied and Environmental microbiology* 65: 2961-2968.

Whyte, L.G., Schultz, A., van Beilen, J.B., Luz, A.P., Pellizari, V., Labbe, D., and Greer, C.W. 2002. Prevalence of alkane monooxygenase genes in Arctic and Antarctic hydrocarbon-contaminated and pristine soils. FEMS *Microbiology Ecology* 41:141-150.

Zeng, Y.X., Li, H.R., Yong, Y., Boz, Z., and Zheng, T.L. 2007. Phylogenetic diversity and phenotypic characterization of cultivable bacterioplankton isolated from polar oceans. *Acta Oceanologica Sinica* 26: 93-103.

References: Modeling

Bear, J. and Y. Bachmat (1990) Introduction to modeling of transport phenomena in porous media. Kluver, Dordrecht. 584pp.

Cole, D.M., H. Eicken, K. Frey, L.H. Shapiro (2004) Observations of banding in first-year Arctic sea ice. J Geophys Res, 109(C08012), 16pp.

Cottier F., H. Eicken, and P. Wadhams (1999) Linkages between salinity and brine channel distribution in young sea ice. J Geophys Res, 104(C7), 15,859–15,871.

Fofonoff, N.P. and R.C. Millard (1983) Algorithms for computation of fundamental properties of seawater. UNESCO Tech Papers in Mar Sci 44, 53 pp.

Ganesan, S. and D.R. Poirier (1990) Conservation of mass and momentum for the flow of interdendritic liquid during solidification. Met and Materials Trans B, 21(1), 173–181.

Lake, R.A. and E.L. Lewis (1970) Salt rejection by sea ice during growth. J Geophys Res, 75(3), 583–597.

Light, B., G.A. Maykut, T.C. Grenfell (2003) Effects of temperature on the microstructure of first-year Arctic sea ice. J Geophys Res, 108(C2), 3051.

Niedrauer, T.M and S. Martin (1975) An experimental study of brine drainage and convection in young sea ice. J Geophys Res, 84(C3), 1176–1186.

Patankar, S.V. (1980) Numerical Heat Transfer and Fluid Flow. Taylor & Francis, New York. 214pp.

Perovich, D.K. and A.J. Gow (1996) A quantitative description of sea ice inclusions, J Geophys Res, 101(C8), 18,327–18343.

Petrich, C., P.J. Langhorne, and Z.F. Sun (2006) Modelling the interrelationships between permeability, effective porosity and total porosity in sea ice. Cold Regions Science and Technology, 44(2), 131–144.

Petrich, C. and H. Eicken (2010) Growth, structure, and properties of sea ice. In *Sea Ice, 2nd ed.*, Thomas, D.N. and G.S. Dieckmann (eds), Wiley-Blackwell.

Reeburgh, W.S. (1984) Fluxes associated with brine motion in growing sea ice. Pol Biol. 3(1), 29–33.

Untersteiner, N. (1961) On the mass and heat budget of Arctic sea ice. Archive fur Meteorl Geophys Bioklim Series A, 12, 151–182.

Wakatsuchi, M. and N. Ono (1983) Measurements of salinity and volume of brine excluded from growing sea ice. J Geophys Res, 88(C5), 2943–2951.

Wakatsuchi, M. and T. Saito (1985) On brine drainage channels of young sea ice. Ann Glaciol, 6, 200–202.

Weeks, W.F. (2010) On Sea Ice. University of Alaska Press, USA, 664 pp

Appendices

Appendix A Results from ice column experiments, phase II

A1 Thin section analysis

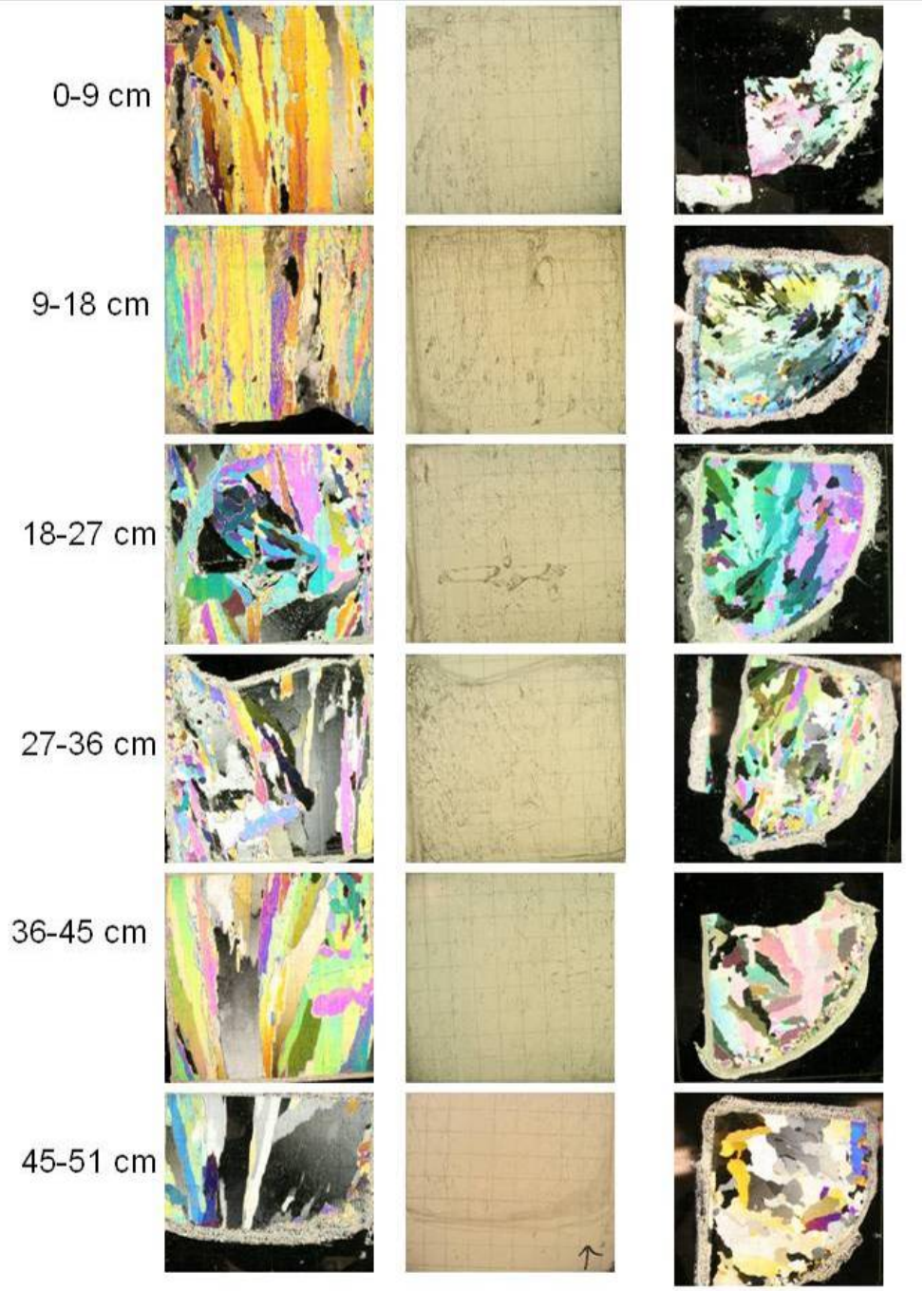

Figure A 1 Thin sections from the reference column (Col 1): Vertical slides at the left and horizontal at the right, photographed between crossed polarizers. Middle column shows horizontal thin sections photographed in plain transmitted light. Ice depth given from top to bottom.

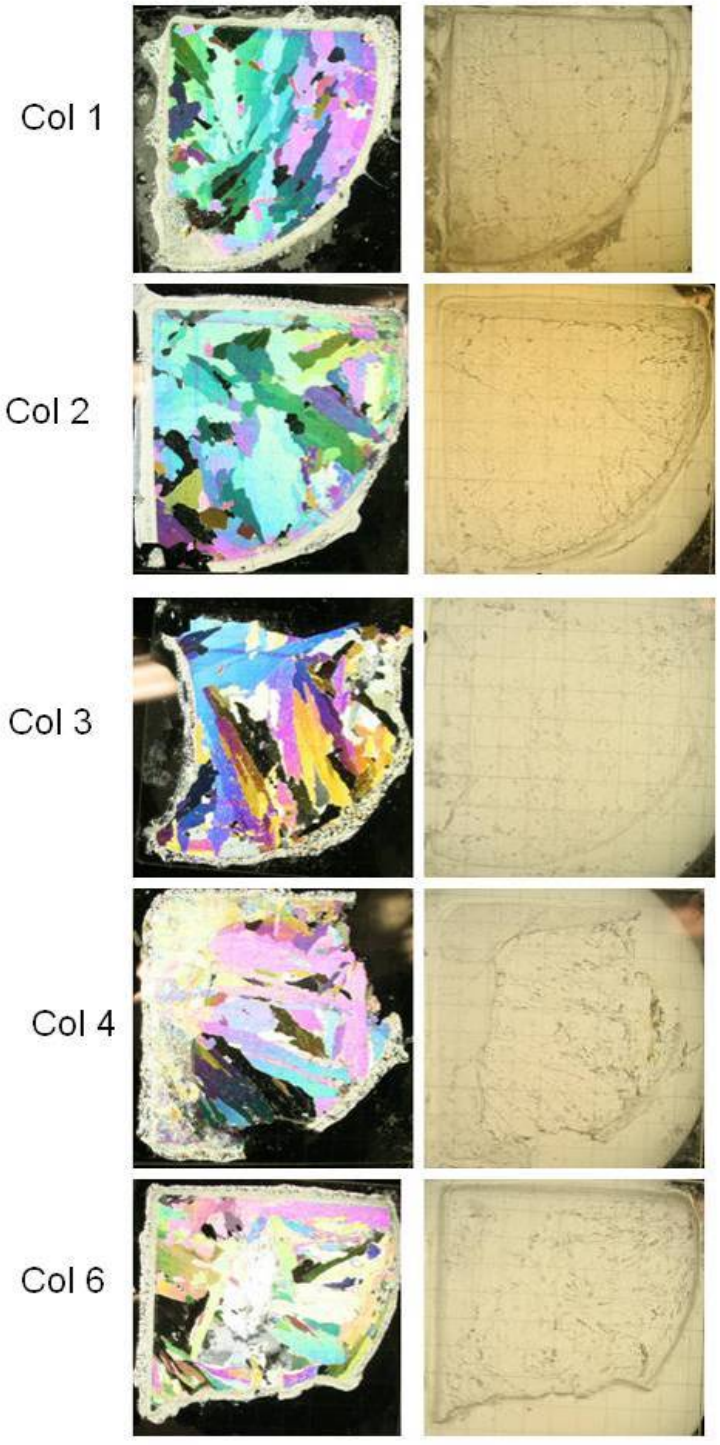

Figure A 2 Thin sections: Horizontal slides from 25-26 cm depth.

A2 Chemical analysis

Table A 1 Target PAH and PAH groups (SVOC: Semi volatile organic compounds) analyzed by GC/MS-SIM. Abbreviations included.

Group	Compound		Group	Compound	
Decalin	Decalin	D	4-6	Benz[*a*]anthracene	BA
	C1-decalins	D1	PAH	Chrysene	C
	C2-decalins	D2		C1-chrysenes	C1
	C3-decalins	D3		C2-chrysenes	C2
	C4-decalins	D4		C3-chrysenes	C3
Naph-	Naphthalene	N		C4-chrysenes	C4
thalene	C1-naphthalenes	N1		Benzo[*b*]fluoranthene	BBF
	C2-naphthalenes	N2		Benzo[*k*]fluoranthene	BK
	C3-naphthalenes	N3		Benzo[*e*]pyrene	BEP
	C4-naphthalenes	N4		Benzo[*a*]pyrene	BA
2-3 ring	Biphenyl	B		Perylene	PE
PAHs	Acenaphthylene	ANY		Indeno[*1,2,3-c,d]*pyrene	IN
	Acenaphthene	ANA		Dibenz[*a,h]*anthracene	DB
	Dibenzofuran	DBF		Benzo[*g,h,i*]perylene	BPE
	Fluorene	F	C0-C4	Phenol	PH
	C1-fluorenes	F1	phenols	C1-Phenols	PH1
	C2-fluorenes	F2		2-methylphenol	
	C3-fluorenes	F3		4-methylphenol	
	Phenanthrene	P		C2-Phenols	PH2
	Anthracene	A		4-ethylphenol	
	C1-phenanthrenes/anthracenes	P1		2,4-dimethylphenol	
	C2-phenanthrenes/anthracenes	P2		3,5-dimethylphenol	
	C3-phenanthrenes/anthracenes	P3		C3-Phenols	PH3
	C4-phenanthrenes/anthracenes	P4		4n-propylphenol	
	Dibenzothiophene	D		2,4,6-trimethylphenol	
	C1-dibenzothiophenes	D1		2,3,5-trimethylphenol	
	C2-dibenzothiophenes	D2		C4-Phenols	PH4
	C3-dibenzothiophenes	D3		4n-butylphenol	
	C4-dibenzothiophenes	D4		4-tertbutylphenol	
4-6 ring	Fluoranthene	FL		4-isopropyl-3-methylphenol	
PAH	Pyrene	PY			
	C1-fluoranthenes/pyrenes	FL1			
	C2-fluoranthenes/pyrenes	FL2			
	C3-fluoranthenes/pyrenes	FL3			

Table A 2 Overview SPME sampling from ice core experiment. Yellow color in the table indicates that no sampling was performed due to problems with removing the SPMEs from the column and/or SPME breakage. Orange color indicates that oil migration had reached the SPMEs.

No sampling
Bulk oil migration

Col 5	Ice depth (cm)	Day 2	Day 11	Day 25	Day 65	Day 65	Day 65
	15			5D3	5D4-1	5D4-2	5D4-3
	25	5C1			5C4		
	35			5B3	5B4		
	55	5A1	5A2	5A3	5A4		
Col 7*		Day 6	Day 11	Day 25	Day 65		
	15			7D3			
	25			7C3			
	35	7B1	7B2	7B3			
	55			7A3			
Col 8		Day 6	Day 11	Day 25	Day 65	Day 65	Day 65
	15			8D3	8D4-1	8D4-2	8D4-3
	25		8C2	8C3	8C4		
	35		8B2	8B3	8B4-1	8B4-2	
	55	8A1		8A3	8A4		

*COL 7: Experiment finalized after 30 days due to temperature problems (ice melted)

Table A 3 Semi volatiles from reference SPMEs (not exposed in ice or seawater), given in ng analyte/mg SPME**.**

	SPME blank 1 ref (not in ice) ng/mg SPME	SPME blank 2 ref (not in ice) ng/mg SPME	SPME blank 3 ref (not in ice) ng/mg SPME
Naphthalene	0.20	0.19	0.20
C1-naphthalenes	0.32	0.27	0.32
C2-naphthalenes	ND	ND	ND
C3-naphthlens	ND	ND	ND
C4-naphthalenes	ND	ND	ND
Biphenyl	ND	ND	ND
Fluorene	ND	ND	ND
Phenanthrene	ND	ND	ND
C1-phenanthrenes	ND	ND	ND

Table A 4 Semi volatiles from SPME in column 5, given in ng analyte/mg SPME and ng analyte/L pore water (based on porosity) days (d) after oil application.

COL 5	5A1 (d 2) 55 cm ng/mg	5C1 (d 2) 25 cm ng/mg	5A2 (d 11) 55 cm ng/mg	5A3 (d 25) 55 cm ng/mg	5B3 (d 25) 35 cm ng/mg	5A4 (d 65) 55 cm ng/mg	5B4 (d 65) 35 cm ng/mg
Naphthalene	0.37	0.27	1.06	0.25	0.25	0.53	0.45
C1-naphthalenes	0.41	0.35	2.08	0.26	0.26	0.48	0.47
C2-naphthalenes	ND	ND	3.11	ND	ND	ND	0.37
C3-naphthalenes	ND	ND	2.76	ND	ND	ND	ND
C4-naphthalenes	ND	ND	ND	ND	ND	ND	ND
Biphenyl	ND	ND	ND	ND	ND	ND	ND
Fluorene	ND	ND	ND	ND	ND	ND	ND
Phenanthrene	ND	ND	ND	ND	ND	ND	ND
C1-phenanthrenes	ND	ND	ND	ND	ND	ND	ND
	ng/L	ng/L	ng/L	ng/L	ng/L	ng/L	ng/L
Naphthalene	225	852	918	216	235	754	428
C1-naphthalenes	272	1134	1913	239	250	759	478
C2-naphthalenes	ND	ND	854	ND	ND	ND	113
C3-naphthlenses	ND	ND	205	ND	ND	ND	ND
C4-naphthalenes	ND	ND	ND	ND	ND	ND	ND
Biphenyl	ND	ND	ND	ND	ND	ND	ND
Fluorene	ND	ND	ND	ND	ND	ND	ND
Phenanthrene	ND	ND	ND	ND	ND	ND	ND
C1-phenanthrenes	ND	ND	ND	ND	ND	ND	ND

ND; Not detected (< 0,01 ng/mg)

Table A 5 Semi volatiles from SPME in column 7, given in ng analyte/mg SPME and ng analyte/L brine water (based on porosity) days (d) after oil application.

. COL 7	7B1 (d 6) 35 cm ng/mg	7B2 (d 11) 35 cm ng/mg	7A3 (d 25) 55 cm ng/mg	7B3 (d25) 35 cm ng/mg	7C3 (d 25) 25 cm ng/mg
Naphthalene	1.20	0.45	0.26	0.24	0.68
C1-naphthalenes	2.63	0.47	0.28	0.22	0.65
C2-naphthalenes	3.75	ND	ND	ND	ND
C3-naphthlens	2.69	ND	ND	ND	ND
C4-naphthalenes	ND	ND	ND	ND	ND
Biphenyl	0.67	ND	ND	ND	ND
Fluorene	ND	ND	ND	ND	ND
Phenanthrene	1.69	ND	ND	ND	ND
C1-phenanthrenes	0.87	ND	ND	ND	ND
	ng/L	ng/L	ng/L	ng/L	ng/L
Naphthalene	1262	423	225	226	1204
C1-naphthalenes	2822	451	258	211	1180
C2-naphthalenes	1161	ND	ND	ND	ND
C3-naphthlens	218	ND	ND	ND	ND
C4-naphthalenes	ND	ND	ND	ND	ND
Biphenyl	442	ND	ND	ND	ND
Fluorene	ND	ND	ND	ND	ND
Phenanthrene	246	ND	ND	ND	ND
C1-phenanthrenes	11.7	ND	ND	ND	ND

ND; Not detected (< 0,01 ng/mg)

Table A 6 Semi volatiles from SPME in column 8, given in ng analyte/mg SPME and ng analyte/L brine water (based on porosity) days (d) after oil application.

COL 8	8A1 (d 6) 55 cm ng/mg	8B2 (d 11) 35 cm ng/mg	8C2 (d 11) 25 cm ng/mg	8A3 (d 25) 55 cm ng/mg	8B3 (d25) 35 cm ng/mg	8C3 (d 25) 25 cm ng/mg
Naphthalene	0.30	0.27	0.38	0.26	0.24	0.67
C1-naphthalenes	0.19	0.34	0.31	0.23	0.36	1.63
C2-naphthalenes	ND	ND	ND	ND	ND	1.02
C3-naphthlens	ND	ND	ND	ND	ND	ND
C4-naphthalenes	ND	ND	ND	ND	ND	ND
Biphenyl	ND	ND	ND	ND	ND	ND
Fluorene	ND	ND	ND	ND	ND	ND
Phenanthrene	ND	ND	ND	ND	ND	ND
C1-phenanthrenes	ND	ND	ND	ND	ND	ND
	ng/L	ng/L	ng/L	ng/L	ng/L	ng/L
Naphthalene	183	254	673	225	226	1186
C1-naphthalenes	126	327	563	212	346	2959
C2-naphthalenes	ND	ND	ND	ND	ND	537
C3-naphthlens	ND	ND	ND	ND	ND	ND
C4-naphthalenes	ND	ND	ND	ND	ND	ND
Biphenyl	ND	ND	ND	ND	ND	ND
Fluorene	ND	ND	ND	ND	ND	ND
Phenanthrene	ND	ND	ND	ND	ND	ND
C1-phenanthrenes	ND	ND	ND	ND	ND	ND

COL 8	8A4 (d 65) 55 cm ng/mg	8B4-1 (d 65) 35 cm ng/mg	8B4-2 (d 65) 35 cm ng/mg	8D4-1 (d 65) 15 cm ng/mg	8D4-2 (d 65) 15 cm ng/mg
Naphthalene	0.58	1.27	1.25	4.66	14.4
C1-naphthalenes	0.59	1.23	1.11	6.15	11.8
C2-naphthalenes	ND	ND	ND	3.34	4.38
C3-naphthlens	ND	ND	ND	1.16	0.82
C4-naphthalenes	ND	ND	ND	ND	ND
Biphenyl	ND	ND	ND	ND	1.13
Fluorene	ND	ND	ND	ND	0.22
Phenanthrene	ND	ND	ND	ND	0.20
C1-phenanthrenes	ND	ND	ND	ND	ND
	ng/L	ng/L	ng/L	ng/L	ng/L
Naphthalene	825	1209	1190	39328	121866
C1-naphthalenes	932	1252	1130	55692	107038
C2-naphthalenes	ND	ND	ND	9113	11951
C3-naphthlens	ND	ND	ND	862	609
C4-naphthalenes	ND	ND	ND	ND	ND
Biphenyl	ND	ND	ND	ND	6331
Fluorene	ND	ND	ND	ND	1048
Phenanthrene	ND	ND	ND	ND	258
C1-phenanthrenes	ND	ND	ND	ND	ND

Table A 7 Semi volatiles in ice cores (melted ice), given in µg analyte/L water (days after oil application). Red letters indicate that oil droplets were present.

In melted ice	Tot SVOC* µg/L	Naphth µg/L	2-3 ring PAH µg/L	4-6 ring PAH µg/L	C_0-C_4 phenols µg/L	Decalins µg/L
Day 6						
col 3 15-20 cm	166	81.6	68.4	12.2	28.5	3.41
col 3 20-25 cm	11.1	6.18	4.29	0.573	2.40	0.03
col 3 26-31 cm	3.79	1.63	1.94	0.223	2.17	ND
col 3 31-36 cm	2.26	1.26	0.91	0.089	1.69	ND
col 3 37-42 cm	1.32	0.73	0.53	0.058	2.38	ND
col 3 42-47 cm	1.21	0.71	0.45	0.048	2.21	ND
col 3 48-53 cm	1.42	0.52	0.81	0.092	2.49	ND
col 3 53-63 cm	1.77	0.57	1.04	0.164	4.50	ND
Day 11						
col 6 15-20 cm	0.27	0.20	0.06	0.011	3.17	ND
col 6 20-25 cm	0.64	0.48	0.15	0.014	3.99	ND
col 6 26-31 cm	0.30	0.16	0.13	0.016	2.25	ND
col 6 31-36 cm	0.16	0.12	0.04	0.009	3.12	ND
col 6 37-42 cm	0.11	0.07	0.04	0.009	2.97	ND
col 6 42-47 cm	0.12	0.06	0.05	0.013	1.18	ND
col 6 48-53 cm	0.24	0.14	0.08	0.020	4.83	ND
col 6 53-58 cm	0.11	0.06	0.04	0.007	2.38	ND
Day 65						
col 2 15-20 cm	97.8	56.1	34.6	4.508	2.04	2.55
col 2 20-25 cm	0.95	0.57	0.34	0.035	1.14	ND
col 2 26-31 cm	0.73	0.43	0.25	0.037	2.91	0.01
col 2 31-36 cm	1.06	0.58	0.43	0.049	1.67	ND
col 2 37-42 cm	1.92	0.92	0.92	0.086	1.54	ND
col 2 42-47 cm	0.49	0.27	0.20	0.025	1.12	ND
col 2 48-58 cm	0.35	0.21	0.13	0.007	0.79	ND
col 2 53-58 cm	0.44	0.28	0.14	0.017	0.85	ND
Water (below ice)						
Col. 1	0.68	0.38	0.29	0.011	3.74	ND
Col. 2	0.43	0.30	0.13	0.008	4.43	ND
Col. 3	0.66	0.45	0.19	0.019	1.01	ND
Col. 4	0.19	0.16	0.02	0.005	3.95	ND
Col. 6	0.36	0.22	0.11	0.029	3.17	ND
Reference (no oil)						
col 1 0-9cm	0.48	0.15	0.27	0.062	26.8	ND
col 1 18-27cm	0.68	0.07	0.42	0.187	8.55	ND
col 1 36-45cm	0.17	0.06	0.06	0.050	4.03	ND
Seawater (laboratory blank)						
Average±stdev	0.09±0.08	0.03±0.03	0.06±0.04	0.004±0.004	0.03±0.02	ND

*Phenols not included in tot SVOC

ND: Not detected, or <0.01 µg/L

Table A 8 Semi volatiles in ice cores (melted ice), given in µg analyte/L brine volume (based on porosity). Red letters indicate that oil droplets were present.

Corrected for porosity	Tot SVOC* µg/L	Naphth µg/L	2-3 ring PAH µg/L	4-6 ring PAH µg/L	C_0-C_4 phenols µg/L	Decalins µg/L
Day 6						
col 3 15-20 cm	10349	5100	4275	761	1781	213
col 3 20-25 cm	615	343	238	31.9	134	1.91
col 3 26-31 cm	181	77.8	92.3	10.6	103	ND
col 3 31-36 cm	151	84.3	60.7	5.91	113	ND
col 3 37-42 cm	21.9	12.1	8.87	0.97	39.7	ND
col 3 42-47 cm	16.1	9.44	6.00	0.64	29.5	ND
col 3 48-53 cm	11.0	4.01	6.31	0.71	19.3	ND
col 3 53-63 cm	10.4	3.32	6.10	0.96	26.3	ND
Day 11						
col 6 15-20 cm	15.0	11.4	3.07	0.60	176	ND
col 6 20-25 cm	40.2	29.7	9.54	0.88	249	ND
col 6 26-31 cm	8.19	4.26	3.51	0.42	60.8	ND
col 6 31-36 cm	4.46	3.11	1.10	0.24	84.2	ND
col 6 37-42 cm	1.64	0.98	0.52	0.14	43.7	ND
col 6 42-47 cm	1.77	0.88	0.71	0.18	17.4	ND
col 6 48-53 cm	2.40	1.42	0.78	0.20	48.8	ND
col 6 53-58 cm	1.13	0.62	0.44	0.07	24.0	ND
Day 65						
col 2 15-20 cm	8887	5097	3148	410	186	232
col 2 20-25 cm	86.0	51.8	30.9	3.20	104	ND
col 2 26-31 cm	22.0	13.1	7.52	1.13	88.3	0.31
col 2 31-36 cm	29.4	16.2	11.8	1.36	46.3	ND
col 2 37-42 cm	20.3	9.73	9.63	0.90	16.2	ND
col 2 42-47 cm	5.50	3.00	2.22	0.28	12.4	ND
col 2 48-58 cm	3.65	2.19	1.39	0.07	8.32	ND
col 2 53-58 cm	5.14	3.27	1.68	0.20	9.84	ND

*Phenols not included in tot SVOC
ND: Not detected, or <0.01 µg/L

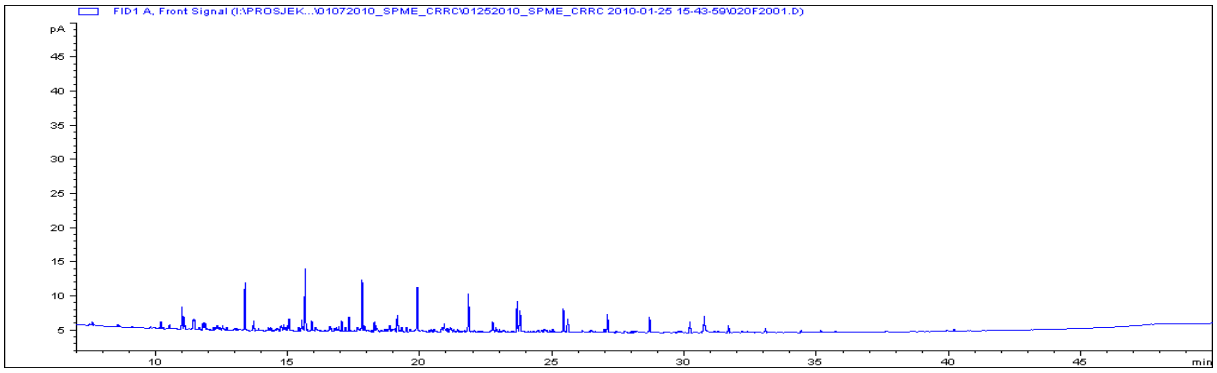

Figure A 3 Column 7, sampling SPME day 25, 15 cm from ice surface (sample 7D3)

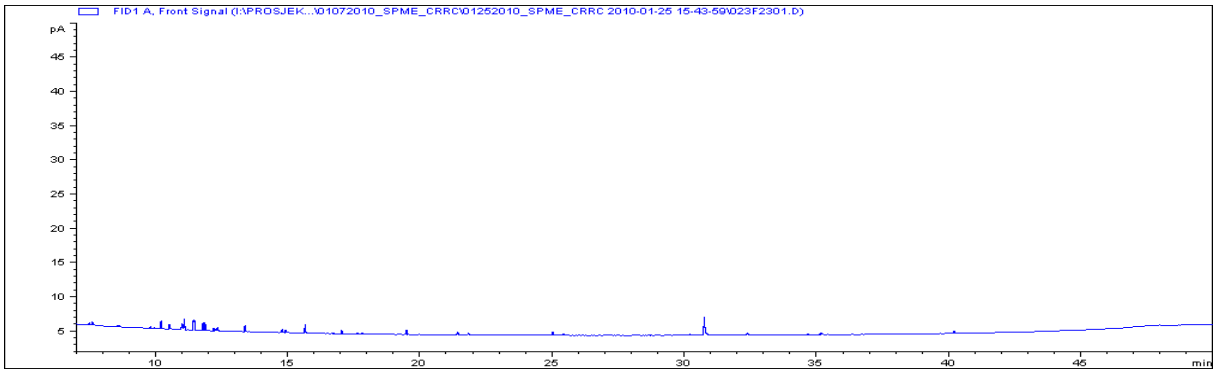

Figure A 4 Col 7, sampling SPME day 25, 25 cm from ice surface (sample 7C3)

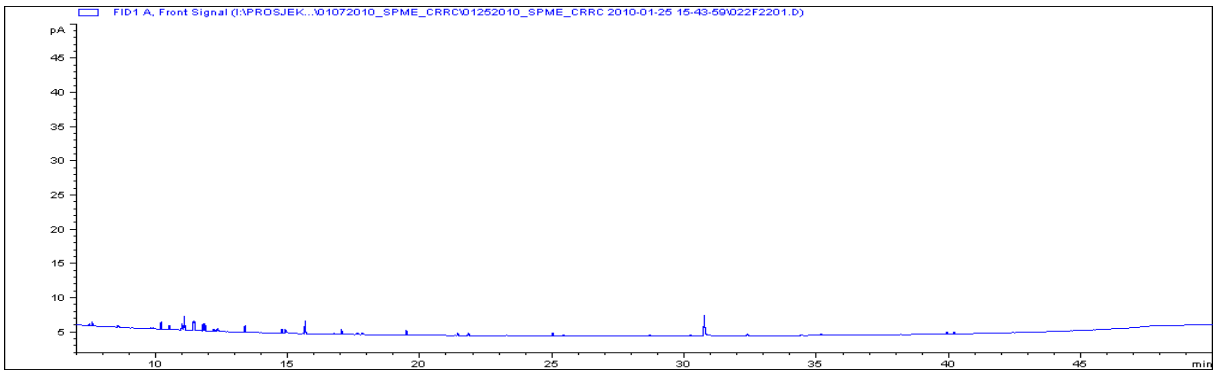

Figure A 5 Col 7, sampling SPME day 25, 35 cm from ice surface (sample 7B3)

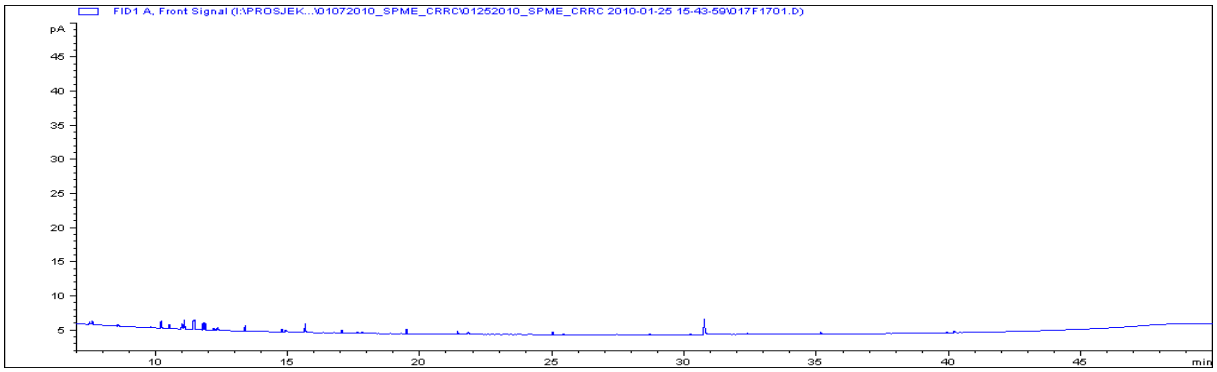

Figure A 6 Col 7, sampling SPME day 25, 55 cm from ice surface (sample 7A3)

Appendix B Results from ice column experiments, phase III

Table B 1 Semi volatiles in ice cores, given in µg analyte/L melted ice. No decalins were detected (Phenols not included in tot SVOC).

	Tot SVOC µg/L	Naphthalenes µg/L	2-3 ring PAH µg/L	4-6 ring PAH µg/L	C0-C4 phenols µg/L
Day 9					
col 6 15-20	3.55	2.01	1.51	0.026	1.88
col 6 20-25	12.2	6.53	5.60	0.090	2.03
col 6 25-30	4.09	2.18	1.87	0.032	0.87
col 6 31-36	5.05	2.57	2.44	0.042	0.87
col 6 36-41	1.97	0.96	0.98	0.023	1.01
col 6 41-46	0.38	0.24	0.14	0.008	1.18
col 6 46-51	0.20	0.12	0.07	0.006	2.13
col 6 51-58	0.27	0.15	0.12	0.006	1.14
col 8 15-20	0.05	0.04	0.01	0.004	0.30
col 8 20-25	0.06	0.04	0.02	0.004	0.15
col 8 25-30	0.09	0.07	0.02	0.005	0.29
col 8 31-36	0.11	0.07	0.03	0.004	0.35
col 8 36-41	0.10	0.07	0.02	0.005	1.33
col 8 41-47	0.07	0.04	0.03	0.004	0.54
Day 21					
col 3 15-20	10.3	2.85	6.52	0.928	0.30
col 3 20-25	0.87	0.15	0.65	0.070	0.27
col 3 25-30	0.14	0.09	0.05	0.005	0.29
col 3 31-36	0.12	0.09	0.03	0.006	0.23
col 3 36-41	0.14	0.09	0.04	0.006	0.29
col 3 41-50	0.09	0.06	0.03	0.005	0.20
col 4 15-20	0.13	0.08	0.05	0.006	0.55
col 4 20-25	0.07	0.05	0.02	0.005	0.80
col 4 25-30	0.08	0.06	0.02	0.004	0.29
col 4 31-36	0.07	0.06	0.01	0.004	0.29
col 4 36-41	0.07	0.06	0.01	0.003	0.36
col 4 41-50	0.06	0.03	0.03	0.004	0.57
Day 35					
col 1 15-20	7.00	3.09	3.68	0.233	1.40
col 1 20-25	0.61	0.25	0.35	0.008	1.10
col 1 25-30	0.22	0.19	0.03	0.004	1.24
col 1 31-36	0.40	0.33	0.07	0.006	1.83
col 1 36-41	0.16	0.13	0.03	0.003	0.74
col 1 41-50	0.15	0.09	0.06	0.004	0.59
col 5 15-20	5.48	2.68	2.59	0.211	0.82
col 5 20-25	0.12	0.09	0.03	0.005	0.67
col 5 25-30	0.08	0.06	0.02	0.005	0.42
col 5 31-36	0.08	0.06	0.01	0.005	0.55
col 5 36-41	0.14	0.08	0.02	0.006	0.45
col 5 41-50	0.07	0.04	0.02	0.005	0.31

Table B 2 Semi volatiles in reference ice cores, given in µg analyte/melted ice, water samples from below the ice, and laboratory blank sample (seawater). No decalins were detected.

	Tot SVOC* µg/L	Naphthalenes µg/L	2-3 ring PAH µg/L	4-6 ring PAH µg/L	C0-C4 phenols µg/L
Ref - 35 d					
col 7 15-20	1.06	1.02	0.03	0.002	0.21
col 7 20-25	0.23	0.21	0.01	0.003	0.08
col 7 25-30	0.68	0.64	0.03	0.003	0.19
col 7 31-36	0.96	0.92	0.04	0.002	0.14
col 7 36-43	0.33	0.30	0.03	0.002	0.20
Water sample - 35 d					
col 1	0.17	0.13	0.03	0.008	2.10
col 2	0.06	0.04	0.02	ND	2.66
col 5	0.28	0.11	0.12	0.040	0.36
col 7	0.10	0.04	0.05	0.006	0.62
Lab blank (seawater)					
sw 1/10	0.02	0.02	ND	ND	ND
sw 26/10	0.03	0.03	ND	ND	0.02
sw 27/10	ND	ND	ND	ND	ND
sw 28/10	ND	ND	ND	ND	ND
sw 29/10	0.05	0.05	ND	ND	ND

*Phenols not included in tot SVOC

ND: Not detected, or <0.01 µg/L

Table B 3 Semi volatiles in ice cores (melted ice), given in µg analyte/L brine volume, based on porosity. No decalins were detected.

	Tot SVOC* µg/L	Naphthalenes µg/L	2-3 ring PAH µg/L	4-6 ring PAH µg/L	C0-C4 phenols µg/L
Day 9					
col 6 15-20	32.9	19.1	12.3	1.49	3.64
col 6 20-25	157	89.5	65.0	2.91	4.19
col 6 25-30	52.6	29.1	21.1	2.35	1.96
col 6 31-36	58.7	31.3	25.2	2.22	1.79
col 6 36-41	19.8	9.19	8.88	1.70	1.72
col 6 41-46	4.80	2.02	1.25	1.53	1.91
col 6 46-51	3.59	0.89	0.60	2.10	3.11
col 6 51-58	1.56	0.49	0.40	0.67	0.64
col 8 15-20	0.59	0.36	0.12	0.10	0.77
col 8 20-25	1.07	0.62	0.28	0.16	0.25
col 8 25-30	1.32	0.97	0.21	0.14	1.14
col 8 31-36	1.63	1.08	0.37	0.18	1.35
col 8 36-41	0.91	0.62	0.18	0.11	3.04
col 8 41-47	0.71	0.39	0.21	0.10	1.24
Day 21					
col 3 15-20	75.7	19.8	49.3	6.58	0.51
col 3 20-25	9.93	1.57	7.58	0.78	0.80
col 3 25-30	2.25	1.26	0.87	0.12	1.28
col 3 31-36	1.67	1.05	0.52	0.10	0.79
col 3 36-41	1.62	0.98	0.56	0.08	0.29
col 3 41-50	0.73	0.38	0.31	0.05	0.11
col 4 15-20	3.02	1.02	0.97	1.03	1.44
col 4 20-25	2.59	0.89	0.38	1.32	3.09
col 4 25-30	2.38	1.04	0.34	1.00	0.96
col 4 31-36	1.61	0.77	0.23	0.61	0.77
col 4 36-41	1.20	0.46	0.14	0.59	0.50
col 4 41-50	0.73	0.21	0.23	0.29	0.78
Day 35					
col 1 15-20	55.4	22.5	29.8	3.01	9.86
col 1 20-25	7.39	2.29	3.61	1.49	2.03
col 1 25-30	4.48	1.65	0.29	2.54	2.30
col 1 31-36	5.07	2.19	0.70	2.19	2.73
col 1 36-41	2.24	0.86	0.28	1.10	0.99
col 1 41-50	1.10	0.35	0.31	0.44	0.50
col 5 15-20	29.4	13.6	14.7	1.14	1.13
col 5 20-25	1.36	0.89	0.40	0.07	2.12
col 5 25-30	0.99	0.68	0.23	0.07	1.57
col 5 31-36	0.95	0.68	0.20	0.07	1.91
col 5 36-41	1.09	0.60	0.15	0.05	0.92
col 5 41-50	0.42	0.23	0.16	0.03	0.49
Ref - 35 d					
col 7 15-20	11.2	10.5	0.37	0.31	0.42
col 7 20-25	2.61	2.05	0.16	0.40	ND
col 7 25-30	8.15	7.46	0.40	0.29	0.42

col 7 31-36	12.3	11.3	0.63	0.35	ND
col 7 36-43	4.20	3.57	0.41	0.21	0.53

*Phenols not included in tot SVOC
ND: Not detected, or <0.01 μg/L

Appendix C Calculation of hazard index

Regression models have been used to describe the relation between acute toxicity and water-octanol coefficient (K_{ow}) for target chemicals to estimate the threshold value of the toxic concentration of each component. It appears to be a linear negative relation between log LC_{50} of the marine organisms and log K_{ow} of the components that give source to toxicity (McCarty et al. (1992 and 1993) and Di Toro et al. (2007)). The equation is expressed as:

$$\log LC_{50} = m \log (K_{ow}) + b \qquad (1)$$

The slope (m), log $K_{ow,}$ and the intercept (b) for different component groups (e.g PAH and phenols) are given in McCarty (1993) and Neff et al. (2000). The LC_{50} (mg/L) is calculated for each component by use of equation (1) and is given in Table C 1.

Hazard quotients for all the target organic chemicals in the sample can be summed to produce a hazard index, which is equivalent to an estimate of the acute toxicity of each ice core.

The HQ for each component (i) was calculated for each ice core sample:

$$HQ_i = C_i/LC50_i \qquad (2)$$

C_i is the concentration of component *i* in the sample and $LC50_i$ is the estimated acute toxicity for component *i* (Table C 1) calculated from equations (1)

HQs were summed for each component group (Table C 2) to produce an estimate of the acute toxicity in the ice; the hazard index (HI):

$$HI = \Sigma HQ \qquad (3)$$

The estimated toxicity of the ice is determined by the sum of the HIs of all component groups. A value of HI > 1 implies toxicity, i.e. the WAF is expected to cause 50% mortality in the test organisms.

Table C 1 Log K_{ow} and estimated toxicity (LC_{50}) of individual components, based on the log LC_{50}/log K_{ow} regressions of Neff , 2002, (PAHs) and McCarty et al., 1993 (phenols).

	Molecular weight	log K_{ow}	LC_{50} (mg/L)
Decalin	138	4.20	0.57
C1-decalins	152	4.60	0.22
Naphthalene	128	3.37	4.87
C1-naphthalenes	142	3.87	1.42
C2-naphthalenes	156	4.37	0.41
C3-naphthalenes	170	4.90	0.11
C4-naphthalenes	184	5.30	0.04
Biphenyl	154	3.90	1.42
Acenaphthylene	152	4.00	1.07
Acenaphthene	154	3.92	1.34
Dibenzofuran	168	4.12	0.86
Fluorene	166	4.18	0.72
C1-fluorenes	180	4.97	0.09
C2-fluorenes	194	5.20	0.06
C3-fluorenes	208	5.70	0.02
Phenanthrene	178	4.46	0.37
Anthracene	178	4.54	0.30
C1-phenanthrenes/antracenes	192	5.14	0.06
C2-phenanthrenes/antracenes	206	5.46	0.03
C3-phenanthrenes/antracenes	220	5.92	0.01
Dibenzothiophene	184	4.38	0.47
C1-dibenzothiophenes	198	4.86	0.14
C2-dibenzothiophenes	212	5.50	0.03
C3-dibenzothiophenes	226	5.73	0.02
Fluoranthene	202	5.22	0.05
Pyrene	202	5.18	0.06
C1-fluoranthenes/pyrenes	216	5.50	0.03
Benz(a)anthracene	228	5.91	0.01
Chrysene	228	5.61	0.02
C1-chrysenes	242	6.14	0.01
Benzo(b)fluoranthene	252	5.80	0.01
Benzo(k)fluoranthene	252	6.00	0.01
Benzo(a)pyrene	252	6.04	0.01
Indeno(1,2,3-c,d)pyrene	276	7.00	0.00
Dibenz(a,h)anthracene	278	6.75	0.00
Benzo(g,h,i)perylene	276	6.43	0.00
Phenol	94	1.50	16.3
C1-phenols	108	1.98	10.2
C2-phenols	122	2.35	7.21
C3-phenols	136	2.70	5.16
C4-phenols	150	3.31	2.63

Table C 2 Predicted toxicity expressed as hazard index (HI). Calculations are based on the concentrations in the brine volume (or pore volume) and the sum of the hazard quotients (concentration in ice/estimated LC_{50}) for each component.

	Tot HI	Naphthalenes	2-3 ring PAH	4-6 ring PAH	C0-C4 phenols
Day 9					
col 8 15-20	0.002	0.0002	0.0011	0.0006	0.0003
col 8 20-25	0.004	0.0003	0.0024	0.0011	0.0001
col 8 25-30	0.004	0.0004	0.0022	0.0013	0.0004
col 8 31-36	0.005	0.0005	0.0026	0.0011	0.0005
col 8 36-41	0.003	0.0003	0.0013	0.0007	0.0012
col 8 41-47	0.003	0.0002	0.0017	0.0007	0.0005
Day 21					
col 4 15-20	0.012	0.0005	0.0094	0.0014	0.0007
col 4 20-25	0.006	0.0008	0.0023	0.0015	0.0013
col 4 25-30	0.004	0.0005	0.0020	0.0012	0.0005
col 4 31-36	0.003	0.0003	0.0014	0.0010	0.0004
col 4 36-41	0.002	0.0002	0.0008	0.0005	0.0003
col 4 41-50	0.003	0.0001	0.0022	0.0004	0.0003
Day 35					
col 1 15-20	0.964	0.0766	0.7976	0.0884	0.0010
col 1 20-25	0.106	0.0059	0.0966	0.0023	0.0009
col 1 25-30	0.004	0.0012	0.0016	0.0006	0.0010
col 1 31-36	0.007	0.0015	0.0033	0.0007	0.0012
col 1 36-41	0.003	0.0007	0.0012	0.0004	0.0004
col 1 41-50	0.005	0.0003	0.0040	0.0003	0.0002
col 5 15-20	0.495	0.0375	0.4040	0.0535	0.0005
col 5 20-25	0.004	0.0007	0.0017	0.0008	0.0007
col 5 25-30	0.003	0.0003	0.0013	0.0010	0.0005
col 5 31-36	0.003	0.0003	0.0010	0.0010	0.0007
col 5 36-41	0.002	0.0002	0.0009	0.0008	0.0004
col 5 41-50	0.001	0.0002	0.0007	0.0004	0.0002
Ref - 35 d					
col 7 15-20	0.007	0.0057	0.0006	0.0004	0.0002
col 7 20-25	0.002	0.0012	0.0007	0.0005	0.0000
col 7 25-30	0.007	0.0040	0.0018	0.0006	0.0002
col 7 31-36	0.009	0.0063	0.0022	0.0005	0.0000
col 7 36-43	0.006	0.0020	0.0030	0.0004	0.0002